Research Activities

– Synchrotron Radiation Experiments –

Electrical Tuning of the Excitonic Insulator
Ground State of Ta₂NiSe₅

Keisuke Fukutani[a], Roland Stania[a], Jiwon Jung[a,b], Eike F. Schwier[c],
Kenya Shimada[c], Chang Il Kwon[a,b], Jun Sung Kim[a,b], Han Woong Yeom[a,b]

[a]*Center for Artificial Low Dimensional Electronic Systems, Institute for Basic Science (IBS),*
77 Cheongam-ro,Nam-gu, Pohang 37673, Republic of Korea
[b]*Department of Physics, Pohang University of Science and Technology (POSTECH),*
77 Cheongam-ro,Nam-gu, Pohang 37673 Republic of Korea
[c]*Hiroshima Synchrotron Radiation Center, Hiroshima University, 2-313 Kagamiyama, Higashi-*
Hiroshima, Hiroshima, Japan

In the recent years, as the experimental identifications of so-called *excitonic insulator* become realistic after more than half a century since their predictions [1], it has garnered considerable attentions as a newly accessible state of matter. Numerous researches have been devoted to understanding the properties of this exotic state of matter over the last few years [2]. On the other hand, how such ground state properties can be modified or manipulated are less well understood. Therefore, revealing the mechanisms to control the excitonic insulator phase not only extends the spectrum of fundamental physics to explore, but is also of paramount importance for realizing the device applications of excitonic insulators.

In this study, we have performed high-resolution angle-resolved photoemission spectroscopy (ARPES) on the excitonic insulator Ta₂NiSe₅ and demonstrate that its excitonic insulator ground state can be electrically controlled by electropositive surface adsorbates. The direct observations of the band structures for various adsorbate coverages (as shown in Figure 1) as well as the theoretical model analysis evidence that the excitonic insulator phase can be modified by the surface dipole layers.
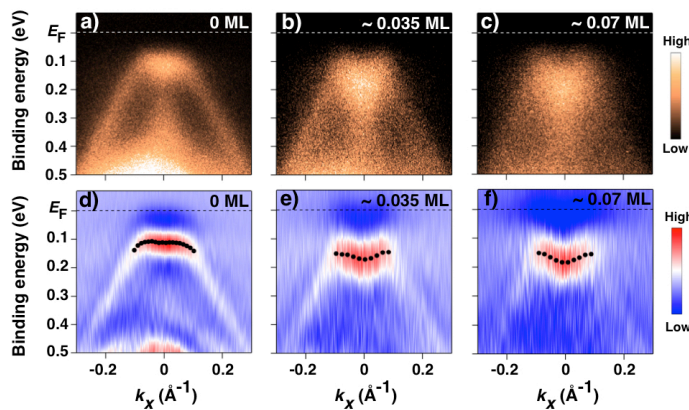

FIGURE 1. The evolution of the valence band maximum in Ta₂NiSe₅ as a function of K coverage, revealed by ARPES intensity maps [(a), (b) and (c)] and their corresponding second derivatives [(d), (e) and (f)]. The filled circles in (d)-(f) indicate the peak positions of the energy distribution curves (EDCs) as extracted from the ARPES spectra. The ARPES measurements were performed at BL-1 at HiSOR.

REFERENCES

1. W. Kohn, Phys. Rev. Lett. **19**, 439 (1967); D. Jerome *et al.*, Phys. Rev. **158**, 462 (1967).
2. Y. Wakisaka *et al.*, Phys. Rev. Lett. **103**, 026402 (2009); Y. F. Lu *et al.*, Nat. Commun. **8**, 14408 (2017); S. Mor *et al.*, Phys. Rev. Lett. **119**, 086401 (2017).

Electronic Structure and H-T Phase Diagram of Eu(Fe$_{1-x}$Rh$_x$)$_2$As$_2$

ShaozhuXiao^a,Darren C. Peets^a, YaFeng^a, Wen-He Jiao^b,Eike F. Schwier^c, Kenya Shimada^c and ShaolongHe^a,

^{a}*Ningbo Institute of Materials Technology and Engineering,Chinese Academy of Sciences, Ningbo, Zhejiang 315201, China*
^{b}*Department of Physics, Zhejiang University of Science and Technology, Hangzhou, Zhejiang 310023, China*
^{c}*Hiroshima Synchrotron Radiation Center, Hiroshima University, Higashi-Hiroshima 739-0046, Japan*

Keywords:ARPES, EuFe$_2$As$_2$, iron-based superconductor.

Superconductivity and magnetic order are normallyantagonistic and often vie for the same unpaired electrons. More generally, the zero-field ground state of a superconductor withsinglet pairing is perfectly diamagnetic, and magnetismwithin the material reduces the energy saved throughpairing as the pair condensate is forced to adapt or compensate. Given the complex relationship between magnetism and high-temperature superconductivity, the interactions of magnetic order with these superconductorsoffers an important opportunity to shed light on the pairing in these systems, which remains among the greatestunsolved problems in condensed matter physics.

Doped EuFe$_2$As$_2$[1-3]offers a unique opportunity tostudy this interaction. It consists of high-temperature-superconducting FeAs layers, but the intermediate layeris a square lattice of magnetic Eu. The FeAs and Eulayers both order magnetically in the undoped parentmaterial [1], but their magnetism is nearly decoupled [3,4]. Superconductivity can be induced by pressure [5] or bychemical substitution [6]. The latter can occur either onthe Eu site, which frustrates the magnetic order whileinjecting charge carriers to the FeAs planes, or withinthe FeAs planes, which introduces disorder to the superconducting system but leaves the magnetic sublatticelargely untouched. Doped EuFe$_2$As$_2$ has a number ofvery unconventional properties, including a reentrant superconducting transition in the resistivity [6] and a reentrant spin-glass phase [7], most likely as a result of thecompetition between superconductivity and magnetism.

The electronic structure of Eu(Fe$_{0.88}$Rh$_{0.12}$)$_2$As$_2$ measured by ARPES with a helium lamp (hν = 21.2 eV) isdisplayed in Fig. 1. Figs. 1(a-d) show the Fermi surface and constant-energy contours at binding energiesE_b = 0, 20, 40, and 60meV taken at a temperatureof 15 K, just below the critical temperature. Similar toEuFe$_2$As$_2$ with other dopants [8,9], there are hole pockets around the point and electron pockets around theM points. The band dispersions centered around the$\bar{\varGamma}$ point [along cut #1 in Fig. 1(a)] and M [along cut#2 in Fig. 1(a)] at different temperatures are shown inFigs. 1(e-h) and Figs. 1(i-l), respectively. Energydistribution curves (EDCs) are shown as a function of temperature at Fermi momenta near $\bar{\varGamma}$and M in Figs. 1(m) and1(n), respectively. Upon increasing temperature throughthe critical temperature Tc (from 15 to 50 K), no significant changes in the band structure can be observedaround the $\bar{\varGamma}$ or M point, we do not observe a gap opening, and no features near the Fermi level EF can be unambiguously identified as coherence peaks. This is mostlikely a consequence of being too close to Tc.

To improve the energy resolution and avoid any inhomogeneity of the cleaved surface, laser-ARPES witha spot size below 5 μm was also used to measure theband structure around the $\bar{\varGamma}$ point (Fig. 2 shows data at13 K). Despite an energy resolution better than 5 meV,there are still no significant changes with temperatureand no visible gap.A superconductor with a high transition temperature would normally have a sizeable gap,but this close to the transition temperature it would bevery small. The lack of observable signatures of a pairinggap may also arise from space charge effects, which wecannot completely rule out in the laser-ARPES data, orEu acting as a magnetic impurity. The pair-breakinginduced by magnetic impurities can lead to "gaplesssuperconductivity" [10, 11], a state which was discussed extensively in connection with BCS superconductors.
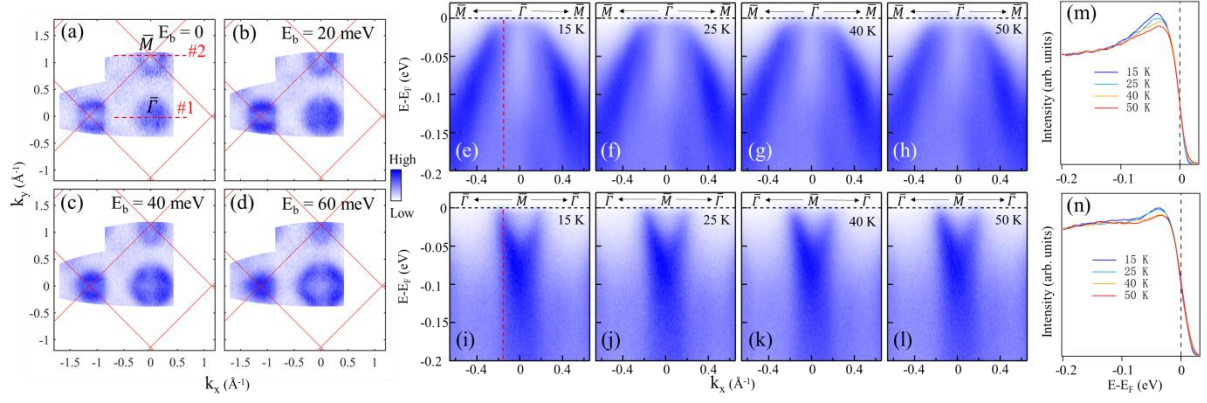
FIGURE 1. Electronic structure of $Eu(Fe_{0.88}Rh_{0.12})_2As_2$ measured by ARPES with a photon energy $h\nu$ = 21.2 eV. (a-d) Constant energy contours at 15K at different binding energies as labeled. (e-l) Energy-momentum images taken at different temperatures along the (e-h) $\bar{M} - \bar{\Gamma} - \bar{M}$ direction as indicated by dashed line #1 in (a), and (i-l) along the $\bar{\Gamma} - \bar{M} - \bar{\Gamma}$ direction as indicated by dashed line #2 in (a). (m) Temperature-dependent EDCs extracted from images (e-h) at the Fermi momentum of the hole pocket, shown by the dashed line in (e). (n) Temperature-dependent EDCs extracted from images (i-l) at the Fermi momentum of the electron pocket, identified by the dashed line in (i).
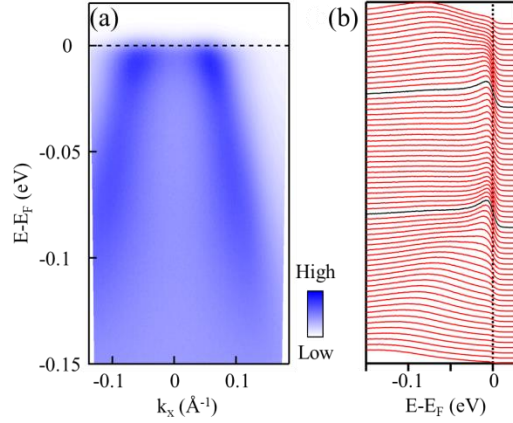

FIGURE 2. (a) Band structure of $Eu(Fe_{0.88}Rh_{0.12})_2As_2$ crossing the $\bar{\Gamma}$ point along the $\bar{M} - \bar{\Gamma} - \bar{M}$ direction measured by μ-laser ARPES ($h\nu$ = 6.3 eV) at 13 K. (b) Energy distribution curves (EDCs) extracted from (a). EDCs at the Fermi momenta are plotted in black.

The band dispersion measured at 13K in the s polarization geometry (electric field perpendicular to the plane of incidence) is shown in Fig. 2(a). This geometry will selectively detect d_{xy} and d_{yz} orbitals, for polarization along y with z being the surface normal. The difference in the Fermi wavevector k_F between Figs. 2(a) and 1(e-h) is mostly likely due to either k_z dispersion or differences in carrier doping at the surface—the material cleaves through the Eu charge reservoir layer. As seen more clearly in the EDCs shown in Fig. 2(b), there is a feature suggestive of a at band near the Fermi level, reminiscent of heavy fermion physics. Such a feature can arise from a at 4f band interacting with the regular electrons at low temperature (and having dipole symmetry that matches d_{xy} and d_{yz}), or it can appear when a band top or bottom is just above the Fermi level. A parabolic fit indicates that the top of the hole pocket at $\bar{\Gamma}$ should lie 30meV above the Fermi level, and this apparent at band is most likely a tail from that band top, cut off by the Fermi function.

Based on specific heat and susceptibility measurements, an H-T phase diagram for $Eu(Fe_{0.88}Rh_{0.12})_2As_2$ is obtained and shown in Fig. 3. The phase diagram combines the results of our measurements on $Eu(Fe_{0.88}Rh_{0.12})_2As_2$ for both orientations. The antiferromagnetic transition has been expanded by a factor of 5. Aside from the inclusion of superconductivity, this phase diagram bears a very close resemblance to that of $(Eu_{0.88}Ca_{0.12})Fe_2As_2$ [12]. Such a high degree of similarity is surprising given that the dopants in the latter case are on the Eu site, disrupting the magnetic order, while here the Rh is in the superconducting FeAs planes, weakening the competing superconductivity.
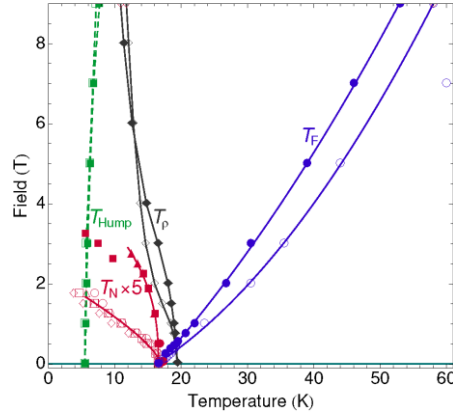
FIGURE 3.H-T phase diagram of Eu(Fe$_{0.88}$Rh$_{0.12}$)$_2$As$_2$ obtained from our specific heat and susceptibility data. Filled symbols are for H // c, and open symbols are for H ⊥ c; lines are guides to the eye. T$_F$ represents field-induced ferromagnetism,T$_{Hump}$ identifies the low-temperature hump in the specific heat, T$_\rho$marks the resistive superconducting transition, and T$_N$ represents the bulk antiferromagnetic transition. T$_N$, which has been expanded by a factor of 5 for clarity, includes points based on the specific heat jump (triangles), susceptibility peak (squares), resistivity (diamonds), and susceptibility jump (circles).

In summary, the antagonistic relationship between the Eu and FeAslayers in EuFe$_2$As$_2$ disrupts both the long-range magneticorder and bulk superconductivity. The consequence forthe magnetism is that the ground state can be tuned bydoping the FeAs layers, likely disrupting the interlayercoupling, and our work indicates that the magnetism'sH-T phase diagram can be traversed with laboratorymagnets. The superconductivity may also be tunable—our data suggest that the FeAs layers may feel astrong field even under zero applied field. The upper critical fields in the iron-based superconductors are normallyvery high and difficult to access, but the EuFe$_2$As$_2$ family may make the high-field region far more accessible. Inparticular, ARPES is a strictly zero-field technique dueto the immediate destruction of momentum informationby any applied magnetic field, so field-dependent ARPESis ordinarily completely impossible. Our results suggestthat in the EuFe$_2$As$_2$ system, ARPES can be performed at a higher effective magnetic field. Tuning the magneticlayers, for instance by Ca or Sr doping, should returnthe system to lower effective field, allowing an effective-magnetic-field-dependent ARPES study and directly accessing the electronic structure under conditions that areordinarily inaccessible to ARPES.

REFERENCES

1. H. Raffius et. al.,J. Phys. Chem. Solids**54**, 135 (1993).
2. Z. Ren et. al., Phys. Rev. B **78**, 052501 (2008).
3. H. S. Jeevan et. al., Phys. Rev. B **78**, 052502 (2008).
4. Y. Xiao et. al., Phys. Rev. B **80**, 174424 (2009).
5. K. Matsubayashi et. al., J. Phys.: Conf. Ser. **215**, 012187 (2010).
6. W.-H. Jiao et. al., Supercond. Sci. Technol. **30**, 025012 (2017).
7. A. Baumgartner et. al., Phys. Rev. B 95, 174522 (2017).
8. S. Thirupathaiah et. al., Phys. Rev. B 84, 014531 (2011).
9. M. Xia et. al., J. Phys.: Condens. Matter 26, 265701 (2014).
10. A. A. Abrikosov and P. Gor'kov, Soviet Physics JETP**12**, 1243 (1961).
11. J. C. Phillips, Phys. Rev. Lett. **10**, 96 (1963).
12. L. M. Tran et. al., Phys. Rev. B 98, 104412 (2018).

Interplay of Exchange and Spin-Orbit Interaction for Interface States in Ni/W(110)

Markus Donath[a], Pascal Jona Grenz[a],
Eike Schwier[b], Koji Miyamoto[b] and Taichi Okuda[b]

[a]*Physikalisches Institut, University of Münster, Wilhelm-Klemm-Straße 10,
48149 Münster, Germany*
[b]*Hiroshima Synchrotron Radiation Center, Hiroshima University*

Keywords: Nickel, tungsten, spin-orbit coupling, exchange interaction, interface states

Due to the high atomic number of tungsten and the ferromagnetic behavior of nickel, ultrathin Ni films on W(110) are well suited for studying the interplay of spin-orbit coupling and exchange interaction. The focus of our spin- and angle-resolved photoemission measurements were (i) the influence of Ni adsorbates on the Dirac-cone-like surface state of W(110) [1], (ii) the spin dependence of electron states at the interface between Ni and W, and (iii) the appearance of ferromagnetic order in the Ni overlayer.

We obtained the following results:

(i)   The Dirac-cone-like surface state vanishes for a coverage above one monolayer [Fig. 1c)]. In the submonolayer region, flat Ni-induced bands appear and overlap with the upper part of the surface state [Fig. 1b)].

(ii)   Interface states near the Fermi level with parabolic-like dispersion and Rashba-type spin splitting are observed for submonolayer [Fig. 2] and monolayer coverages [Fig. 3]

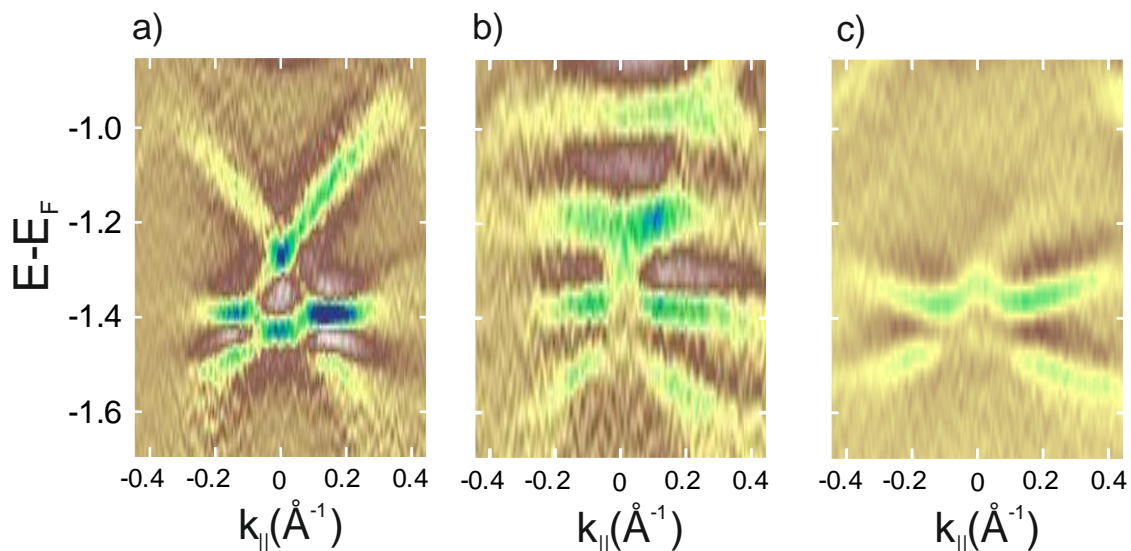(iii)   Ferromagnetic behavior of the Ni film is observed for thicker films, e.g., at about 10 ML.

FIGURE 1. Angle-resolved photoemission measurements (second derivative) of a) clean W(110), b) 0.5ML Ni/W(110), and c) 1ML W(110) along the high symmetry line ΓH.
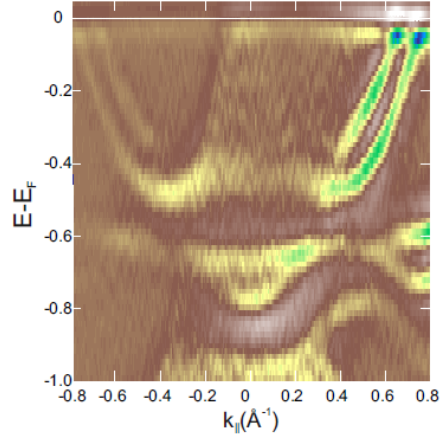
FIGURE 2. Angle-resolved photoemission measurements (second derivative) for 0.5 ML Ni/W(110) along ΓH.
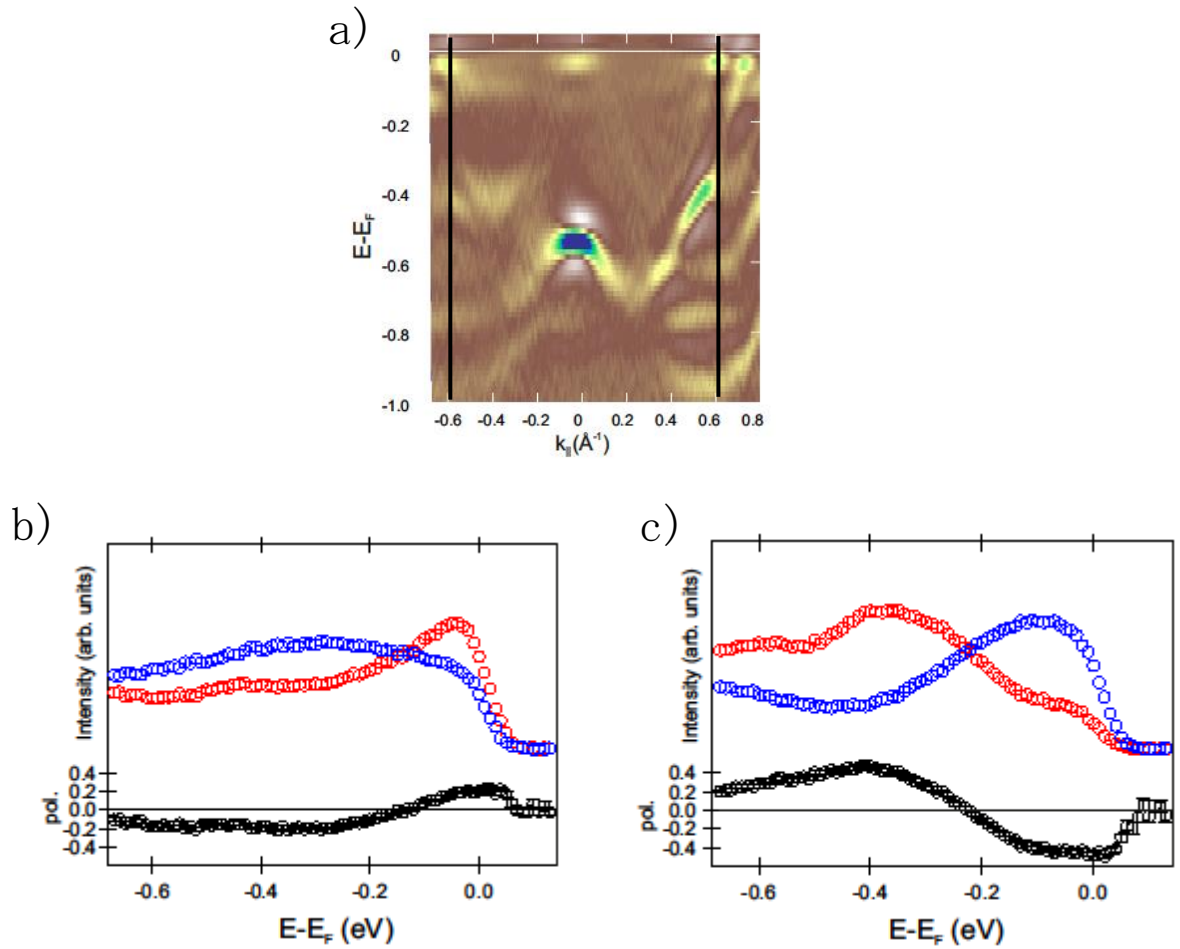

FIGURE 3. a) Angle-resolved photoemission measurements (second derivative) for 1ML Ni/W(110) along ΓH. b+c) Spin-dependent energy distribution curves (EDCs) and spin polarization for $k_{\parallel} \approx \pm 0.6$ Å^{-1} [see black lines in a)]. Blue and red symbols mark spin-up and spin-down components along the Rashba direction.

REFERENCES

1.   K. Miyamoto, A. Kimura, K. Kuroda, T. Okuda, K. Shimada, H. Namatame, M. Taniguchi, and M. Donath, *Phys. Rev. Lett.,* 108, 066808 (2012).

Matrix elements in the resonant photoemission from cerium oxide

Tomáš Duchoň[a], David N. Mueller[a], Shiv Kumar[b], Eike F. Schwier[b], Slavomír Nemšák[c]

[a]*Peter-Grünberg-Institut 6, Forschungszentrum Jülich GmbH, Jülich, Germany*
[b]*Hiroshima Synchrotron Radiation Center, Hiroshima University, Hiroshima, Japan*
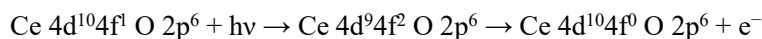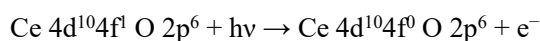[c]*Advanced Light Source, Lawrence Berkeley National Laboratory, Berkeley, USA*

Keywords: cerium oxide, resonant photoemission, matrix elements

Cerium oxide, an industrially relevant material, has a remarkable ability to act either as a supply or a sink of oxygen that allows it to balance oxygen-lean and oxygen-rich phases essential for chemical conversion [1,2]. The ability is realized by a redox cycle that utilizes a facile change of stoichiometry between two stable configurations—CeO_2 (Ce^{4+}) and Ce_2O_3 (Ce^{3+}) [3]. The redox cycle of cerium oxide represents a dramatic alteration of the occupancy of the valence shell. Specifically, the highest occupied subshell is changed within the redox cycle via $4f^0$ and $4f^1$ electronic configurations [4]. Probing the 4f occupation is thus of great importance for unraveling key elements of cerium oxide chemistry.
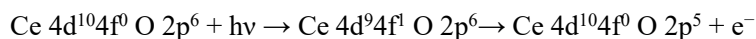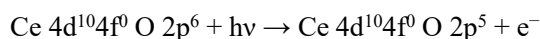
Resonant photoemission is becoming increasingly important as a probe of the 4f shell of cerium oxide. The resonant enhancement at the $4d \rightarrow 4f$ photoabsorption threshold uniquely allows for the detection of very low concentration of Ce^{3+} ions in the system. As such, a universal recipe for quantification of the resonant photoemission in cerium oxide is sought after. Lykhach et al. proposed an elegant solution for the quantification via a proportion coefficient calibrated to core level spectroscopy [5]. The simplicity of the approach encouraged its use; however, the assumptions necessary are poorly understood.

The quantification process relies on comparison of intensities of two resonant features associated with Ce^{4+} and Ce^{3+} ions. We have recently shown, based on results obtained at HiSOR, that the two features are of a disparate origin [6]. For a Ce^{3+} ion, it is an *intra*-atomic process; while for a Ce^{4+} ion, it is an *inter*-atomic process that carries information about cation–anion covalency. The two can be described within a nominal electron configuration as follows:

(Ce^{3+} ion)

Ce $4d^{10}4f^1$ O $2p^6$ + hν $\rightarrow$ Ce $4d^{10}4f^0$ O $2p^6$ + e^-

Ce $4d^{10}4f^1$ O $2p^6$ + hν $\rightarrow$ Ce $4d^9 4f^2$ O $2p^6$ $\rightarrow$ Ce $4d^{10}4f^0$ O $2p^6$ + e^-

(Ce^{4+} ion)

Ce $4d^{10}4f^0$ O $2p^6$ + hν $\rightarrow$ Ce $4d^{10}4f^0$ O $2p^5$ + e^-

Ce $4d^{10}4f^0$ O $2p^6$ + hν $\rightarrow$ Ce $4d^9 4f^1$ O $2p^6$ $\rightarrow$ Ce $4d^{10}4f^0$ O $2p^5$ + e^-

The above illustrates that fact the symmetry of the O 2p and Ce 4d and 4f states enters the quantification process. Herein, we gauge the symmetry contribution using a Nb-doped cerium oxide (111) epitaxial film grown on gold support. The cation doping introduces a controlled amount of Ce^{3+} ions in the system that are stable against cleaning procedure consisting of annealing in oxygen. We measure the ratio of the intensity of the Ce^{3+} and Ce^{4+} resonant features that forms the basis of the quantification process with respect to the

symmetry of the experiment. The results are plotted in Figure 1. Two important points are immediately apparent from the figure. First, while the Ce^{3+} resonant feature related to highly localized 4f electrons does not show any measurable dispersion [6], the dispersion of the O 2p states governing the Ce^{4+} resonant feature significantly modifies the resulting ratio, up to a factor of 3 when moving away from the Γ point. Second, the polarization of the exciting light introduces a sizeable factor, with *s* polarized light favoring the Ce^{4+} resonant feature.
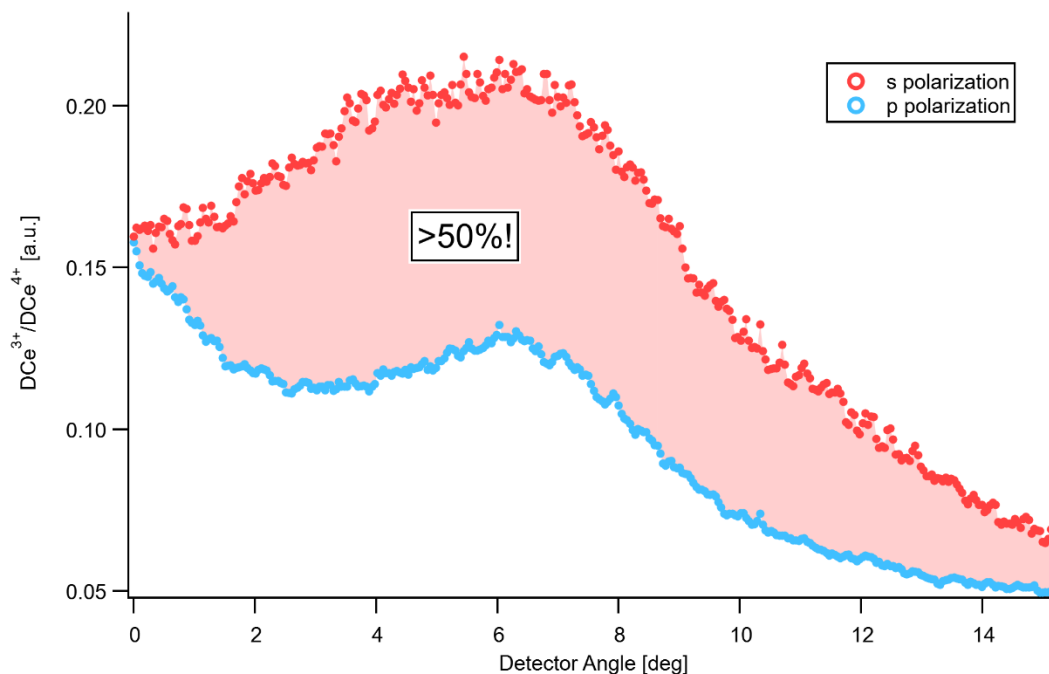

FIGURE 1. The ratio of the intensity of the Ce^{3+} and Ce^{4+} resonant features measured along Γ → M high-symmetry direction of Nb-doped cerium oxide (111) surface with *s* and *p* polarized light (hν = 124.5 eV).

The results clearly illustrate that the quantification of resonant photoemission in cerium oxide as proposed in [5] is useful for general comparison only when the samples examined are disordered at the probing lengthscale. Any other evaluation has to precisely account for the geometry of the experiment. It should be noted that the geometry in question includes Ce–O bond length, a quantity that is known to differ, among other influences, with a stoichiometry of cerium oxide. Understanding the effects pointed out in our study provides an opportunity to reveal phenomena that would be otherwise hidden, or falsely interpreted, in the signal variations originating from matrix elements.

REFERENCES

1. Montini, T.; Melchionna, M.; Monai, M.; Fornasiero, P. *Chem. Rev.* **2016**, 116, 5987–6041.
2. Mullins, D. R. *Surf. Sci. Rep.* **2015**, 70, 42–85.
3. Skorodumova, N. V.; Simak, S. I.; Lundqvist, B. I.; Abrikosov, I. A.; Johansson, B. *Phys. Rev. Lett.* **2002**, 89, 166601.
4. Chen, B.; Ma, Y.; Ding, L.; Xu, L.; Wu, Z.; Yuan, Q.; Huang, W. *J. Phys. Chem. C* **2013**, 2, 5800–5810.
5. Lykhach, Y.; Kozlov, S. M.; Skála, T.; Tovt, A.; Stetsovych, V.; Tsud, N.; Dvořák, F.; Johánek, V.; Neitzel, A.; Mysliveček, J.; Fabris, S.; Matolín, V.; Neyman, K. M.; Libuda, J. *Nature Materials* **2016**, 15, 284–288.
6. Duchoň, T.; Aulická, M.; Schwier, E. F.; Iwasawa, H.; Zhao, C.; Xu, Y.; Veltruská, K.; Shimada, K.; Matolín, V. *Phys. Rev. B* **2017**, 95, 165124.

Superstructure-Induced Splitting of Dirac Cones in Silicene

Baojie Feng,[1,2,*] Hui Zhou,[1,2] Ya Feng,[3,4] Hang Liu,[1,2] Shaolong He,[3] Iwao Matsuda,[5] Lan Chen,[1,2] Eike F. Schwier,[4] Kenya Shimada,[4] Sheng Meng,[1,†] and Kehui Wu[1,2,‡]

[1]*Institute of Physics, Chinese Academy of Sciences, Beijing 100190, China*
[2]*School of Physical Sciences, University of Chinese Academy of Sciences, Beijing 100049, China*
[3]*Ningbo Institute of Materials Technology and Engineering, Chinese Academy of Sciences, Ningbo 315201, China*
[4]*Hiroshima Synchrotron Radiation Center, Hiroshima University, 2-313 Kagamiyama, Higashi-Hiroshima 739-0046, Japan*
[5]*Institute for Solid State Physics, The University of Tokyo, Kashiwa, Chiba 277-8581, Japan*

Keywords: Silicene, Dirac cone, ARPES.

Atomic scale engineering of two-dimensional materials could create devices with rich physical and chemical properties. External periodic potentials can enable the manipulation of the electronic band structures of materials. A prototypical system is 3×3-silicene/Ag(111), which has substrate-induced periodic modulations. Recent angle-resolved photoemission spectroscopy measurements revealed six Dirac cone pairs at the Brillouin zone boundary of Ag(111), but their origin remains unclear [1]. We used linear dichroism angle-resolved photoemission spectroscopy, the tight-binding model, and first-principles calculations to reveal that these Dirac cones mainly derive from the original cones at the K (K') points of free-standing silicene. The Dirac cones of free-standing silicene are split by external periodic potentials that originate from the substrate-overlayer interaction.

Both the sample preparation and ARPES measurements were performed at the linear undulator beam line BL-1. Monolayer silicene was prepared by evaporating silicon from a silicon wafer onto a Ag(111) substrate. The linear polarization of the incident light could be switched between s and p by rotating the whole ARPES system; this ensured pure s and p polarization without cross contamination as is the case with undulator-based polarization switching [2].
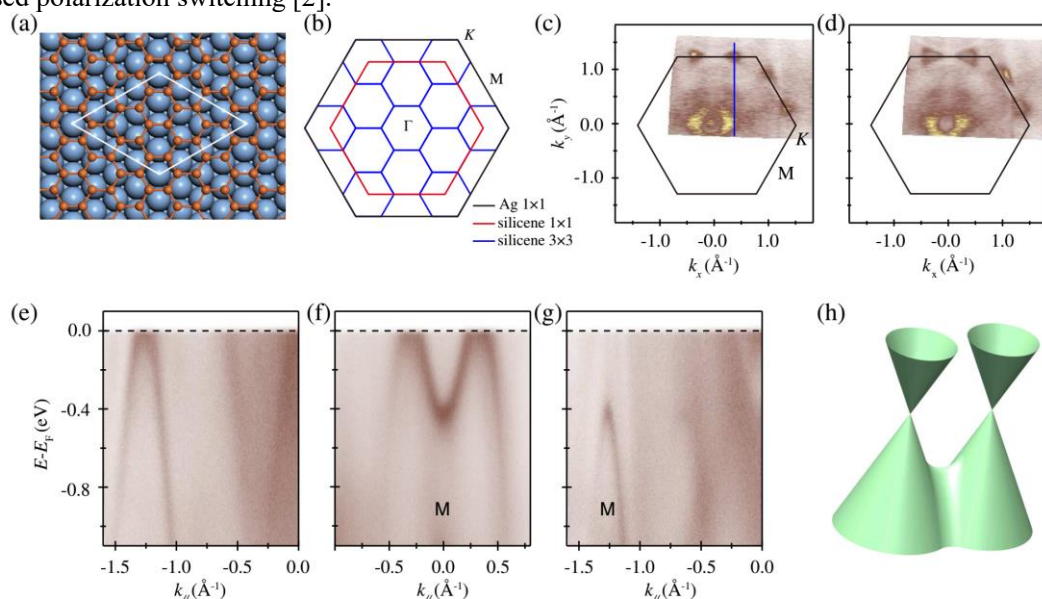
FIGURE 1. (a) Atomic structure of 3 × 3 silicene on Ag(111). Orange and blue balls represent Si and Ag atoms, respectively. The white rhombus indicates a unit cell of the 3 × 3 superstructure. (b) BZs of silicene (red lines), Ag(111) (black lines), and the superstructure (blue lines). (c) Photoemission intensity at the Fermi level as measured with 50 eV p-polarized photons. The blue line indicates the momentum cut along which the ARPES intensity plots in (e) were taken. (d) The same plot as in (c) but at a binding energy of 0.2 eV.(e)–(g) ARPES intensity plot along the blue line in (c), along the $\overline{\text{K}}$-$\overline{\text{M}}$-$\overline{\text{K}}$ direction, and along the $\overline{\Gamma}$-$\overline{\text{M}}$ direction, respectively.(h) Schematic drawing of a pair of Dirac cones.

Figure 1(a) shows the structure model of 3 × 3 silicene on Ag(111). The white rhombus indicates a unit cell of the superstructure which includes a 3 × 3 superlattice of silicene and a 4 × 4 superlattice of Ag(111). From the Fermi surface in Figure 1(c), we found that there exist a pair of Fermi pockets symmetric to the $\overline{\text{M}}$ point of Ag(111). The size of the pockets increases at higher binding energies, as shown in Figure 1(d). Figure 1(e) shows the band structure along the blue line in Figure 1(c), which shows a linear dispersion. The band structure along the $\overline{\text{K}}$-$\overline{\text{M}}$-$\overline{\text{K}}$ direction also shows a linear dispersion [Figure 1(f)]. These results indicate the existence of a pair of Dirac cones at each BZ boundary of Ag(111), which is consistent with previous ARPES results [1]. Along the perpendicular direction, i.e., the $\overline{\Gamma}$-$\overline{\text{M}}$ direction, we found a reversed parabolic dispersion with the band top located at the $\overline{\text{M}}$ point. These results indicate the existence of a saddle point between the pair of Dirac cones [as illustrated in Figure 1(h)] and agree with previous ARPES results [1,3]. The existence of a saddle point indicates that the pair of Dirac cones have a common origin and is reminiscent of the Weyl cone pair that are split from a Dirac cone after certain symmetry breaking. These results suggest the possibility that the pair of Dirac cones are split from one original cone at the $\overline{\text{M}}$ point of Ag(111).

To confirm this, we first discuss the possible existence of such an original Dirac cone (before splitting) at the $\overline{\text{M}}$ point of Ag(111). From the schematic drawing of the BZs in Figure 1(b), we can see that the K point of the silicene 1 × 1 lattice is equivalent to the $\overline{\text{M}}$ point of Ag(111), because both of them are located at the Γ point of the superstructure (blue hexagons). In analogy to graphene, freestanding silicene naturally hosts a Dirac cone at each K (K')point; this Dirac cone will be folded to the $\overline{\text{M}}$ point of Ag(111) in the presence of the superstructure. Another important fact is that the Dirac cones of a honeycomb lattice mainly derive from the p_z orbitals of the outermost shell. We will show next that this can be experimentally confirmed by our ARPES measurements.
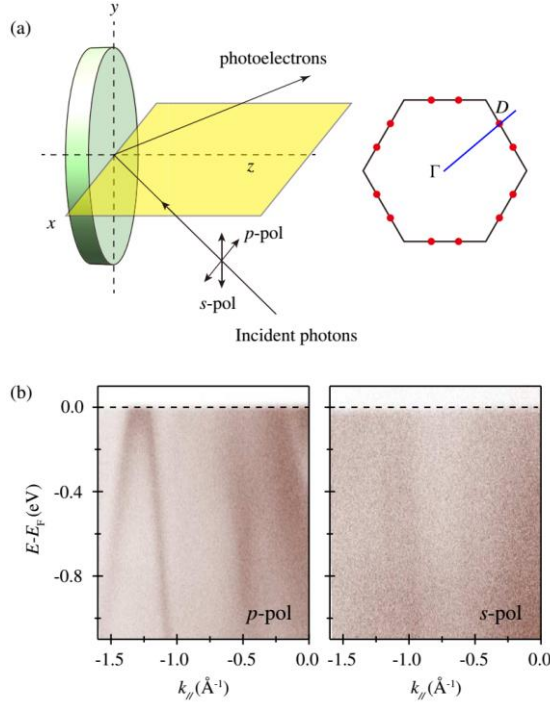

FIGURE 2. (a) Left panel: schematic illustration of the experimental geometries of the ARPES measurements. The incident light lies in the detection plane (colored yellow). The s and p polarization is defined as perpendicular and parallel to the detection plane, respectively. Right panel: schematic drawing of the BZ of Ag(111) and the positions of the Dirac cones. The blue line indicates the momentum cut that includes the Γ point and Dirac point. (b) ARPES intensity plots along the blue line with p and s polarized light, respectively. The incident photon energy is 50 eV.

To disentangle the orbital composition of the Dirac cones, we performed linear dichroism ARPES. In our ARPES measurement setup, the xz plane is the incident plane as well as the detection plane, as shown in Figure 2(a). When the detection plane coincides with the mirror plane of the sample, there will be a selection rule in the photoemission process according to the electric dipole approximation: linearly polarized light tends to excite electronic states that have well-defined parities with respect to the mirror plane: the p-polarized light excites the even-parity states while the s-polarized light excites the odd-parity states [4]. In silicene, the low-energy electronic states are dominated by the p electrons of Si, including the p_x, p_y, and p_z orbitals. In particular, the p_z orbitals always have an even parity when we rotate the sample around the z axis, and thus can only be excited by p-polarized light. The photoemission intensity along the $\overline{\Gamma}$-$\overline{D}$ direction measured with p and s polarized light is shown in Figure 2 (b). One can see that the linearly dispersing Dirac bands are only visible with p polarized light, while they almost disappear with s polarized light; this result indicates that the Dirac cones mainly originate from even parity p_z orbitals. These results further corroborate our speculation that the Dirac cones originate from the original ones of the freestanding silicene.

To capture the physical mechanism of the splitting, it is convenient to use a simple tight-binding model in which the effects of the substrates are treated as perturbations. We start with a flat silicene structure, and only the p_z orbitals of Si are taken into account. When silicene is placed on Ag(111), a 3 × 3 superstructure will form, and, more importantly, the sublattice symmetry will be broken [5]. In our tight-binding model, we used an external perturbation to simulate the effects of the substrate. From this point of view, the superstructure has two prominent effects. First, the band structures will be folded into the BZs of the 3 × 3 supercell because of the Umklapp scattering process, resulting in the appearance of a Dirac cone at the $\overline{M}$ point of Ag(111), as discussed above. Second, it will expose a long-range periodic potential in silicene, which has not yet been taken into account.
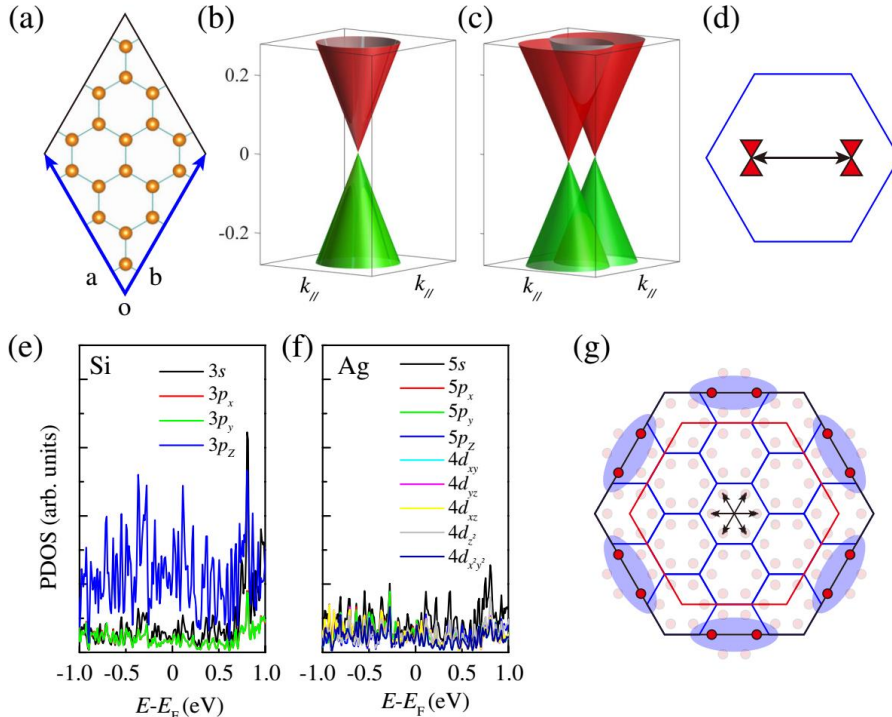

FIGURE 3. (a) Schematic illustration of the periodic potential in our tight-binding model. (b) and (c) Calculated band structures using the tight-binding model before (b) and after (c) applying the periodic potential. (d) Schematic drawing of the splitting direction of the Dirac cones. (e) and (f) Calculated partial density of states of Si and Ag atoms, respectively, using DFT. (g) Schematic drawing of the Dirac cone pairs in the BZs of silicene and Ag(111). The red dots represent the positions of the Dirac cones. The blue shaded ellipses highlight the Dirac cones that have been experimentally observed. The black double arrows indicate the splitting of the Dirac cones.

Applying the periodic potential will break the sublattice symmetry and lead to a dramatic change in the Dirac cone. With proper parameters, the Dirac cone will split along the Γ-K direction of the 3 × 3 supercell [Figure 3(d)], in agreement with our experimental results. Therefore, our tight-binding model could qualitatively explain the origin of Dirac cone pairs that are symmetric to the $\overline{M}$ point of Ag(111). It should be noted that the periodic potential in our tight-binding model does not break the inversion symmetry, which

protects the gapless nature of the Dirac cones [6]. Moreover, our calculated partial density of states near the Fermi level are dominated by the p_z orbitals of Si, as shown in Figure 3(e) and 3(f). These results agree well with our experimental results and support our tight-binding model that only considers the p_z orbitals of Si. On the other hand, although the contributions from the Ag orbitals are smaller than those from Si p_z orbitals, there are still considerable contributions from some orbitals of Ag, such as the s, p_z, and d_z^2 orbitals. These orbitals have out-of-plane components and are prone to hybridize with Si p_z orbitals. This band hybridization, although weak, imposes a periodic potential in the silicene lattice and results in the splitting of the Dirac cone.

In summary, we studied the electronic structures of (3×3)-silicene on Ag(111) using high-resolution ARPES, tight-binding analysis, and DFT calculations. We confirmed the existence of six pairs of Dirac cones at the BZ boundary of Ag(111), but these Dirac cones were only detectable with p polarized light, indicating that the Dirac bands are mainly derived from the p_z orbitals of silicon. Our tight-binding analysis and DFT calculations revealed that these Dirac cones originate from the original Dirac cones of freestanding silicene. Our results settle the long-debated question on the existence of Dirac cones in the silicene/Ag(111) system, and, more importantly, provide a powerful route to tailor the physical properties of Dirac fermions in a honeycomb lattice.

1. Y. Feng et al, *Proc. Natl. Acad. Sci. USA 113, 14656 (2016)*.
2. H. Iwasawa et al, *J. Synchrotron Radiat. 24, 836 (2017)*
3. D. Tsoutsou et al, *Appl. Phys. Lett. 103, 231604 (2013)*
4. A. Damascelli et al, *Rev. Mod. Phys.75, 473 (2003)*
5. C.-L. Lin et al, *Phys. Rev. Lett. 110, 076801 (2013)*.
6. See Supplemental Materials at http://link.aps.org/supplemental/10.1103/PhysRevLett.122.196801 for additional experimental and theoretical analysis.

ARPES Measurements on Thin Films of Topological Crystalline Insulator Pb$_x$Sn$_{1-x}$Te

Yuta Tomohiro[a], Hiroshi Ito[a], Takeru Shimano[a], Ryota Akiyama[b] , Eike F. Schwier[c], Akio Kimura[d], Kenya Shimada[c], Shuji Hasegawa[b], and Shinji Kuroda[a]

[a]*Institute of Materials Science, University of Tsukuba, 1-1-1 Tennoudai, Tsukuba 305-8573, Japan*
[b]*Department of Physics, The University of Tokyo, 7-3-1 Hongo, Bunkyo, Tokyo 113-8654, Japan*
[c]*Hiroshima Synchrotron Radiation Center, Hiroshima University, 1-3-2 Kagamiyama, Higashi-Hiroshima 739-8511, Japan*
[d]*Department of Physics, Hiroshima University, 1-3-2 Kagamiyama, Higashi-Hiroshima 739-8511, Japan*

Keywords: Topological crystalline insulators, Dirac cone, Gap opening, Mirror reflection symmetry

SnTe has been attracting attention as a typical material of topological crystalline insulator (TCI)[1,2], in which the topological surface state (TSS) is protected by the mirror reflection symmetry[1], instead of the time-reversal symmetry (TRS) in the conventional Z_2 topological insulator (TI). Pb$_x$Sn$_{1-x}$Te, a mixed crystal between SnTe and PbTe, exhibits the transition from topological to trivial phase at Pb content $x \sim 0.7$[3-5]. In order to investigate how the TSS in Pb$_x$Sn$_{1-x}$Te changes with the Pb content x, we have performed the angle-resolved photoemission spectroscopy (ARPES) measurement on Pb$_x$Sn$_{1-x}$Te thin films.

We prepared a series of Pb$_x$Sn$_{1-x}$Te (111) thin films with Pb content $x = 0$ (SnTe), 0.17, 0.23, which were grown by molecular beam epitaxy (MBE) on a conductive CdTe template[6]. In the films with $x = 0.17$, 0.23, Sb was doped as a donor impurity with a concentration about 1% in order to compensate the Sn vacancies formed in the crystal. We performed the ARPES measurement at BL-1 of HiSOR. We used a home-made portable vacuum chamber in order to bring the grown films without exposure to air. After having transferred the grown films into the preparation chamber of BL-1, we annealed them at around 200°C to clean the surface. Then we observed the unreconstructed diffraction pattern by low-energy electron diffraction (LEED).

Figure 1 shows the ARPES image of the SnTe (111) film along the $\bar{\Gamma}$-$\bar{M}$ direction. The measurement was done at $T = 20$ K with an incident photon energy of 30 eV. As shown in the figure, one can see band dispersions reaching the Fermi level ($E_F = 0$) both at the $\bar{M}$ and $\bar{\Gamma}$ points. Since the SnTe crystal is heavily p-degenerate due to the formation of Sn vacancies, the Fermi level is below the top of the bulk valenceband. Then we observe only the lower part of the Dirac cone below the Fermi level.

Figures 2 and 3 the ARPES images of the Pb$_x$Sn$_{1-x}$Te films with $x = 0.17$ and 0.23, respectively, taken in the same measurement condition as in Fig. 1. As shown in the figures, one can see a similar band dispersion reaching the Fermi level at the $\bar{M}$ point. On the other hand, it does not reach the Fermi level at the $\bar{\Gamma}$ point. This suggests that a gap opens in the Dirac cone at the $\bar{\Gamma}$ point while that at the $\bar{M}$ point remains gap-closed.

Similar transition was reported in another TCI material (Pb,Sn)Se[7]; In the (111) surface of (Pb,Sn)Se with a Pb composition in the range of the TCI phase, it was observed that a gap is opened in the Dirac cone at the $\bar{\Gamma}$ point upon Bi-doping, while those at the $\bar{M}$ points remain gap-closed. This gap opening was attributed to the phase transition from the TCI phase to the Z_2 topological phase due to the breaking of the mirror reflection symmetry of the crystal upon Bi-doping. In the present case, we observed the gap-opening only at the $\bar{\Gamma}$ in the Pb$_x$Sn$_{1-x}$Te films with Sb doping. This gap-opening may be related to a similar phase transition caused by the lattice distortion due to Sb-doping. Further studies analyzing details of the lattice distortion would be needed in order to understand the origin of the observed gap-opening.
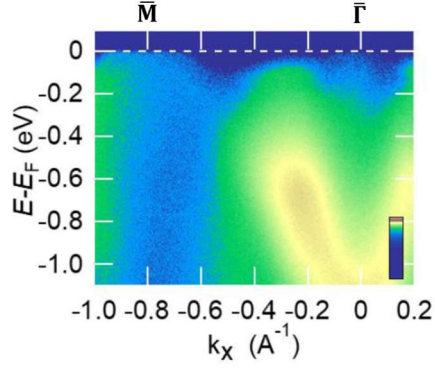
FIGURE 1. ARPES image of a SnTe (111) film along the $\bar{\Gamma}$-$\bar{M}$ direction. The measurement was done at $T = 20$ K with an incident photon energy of 30 eV.
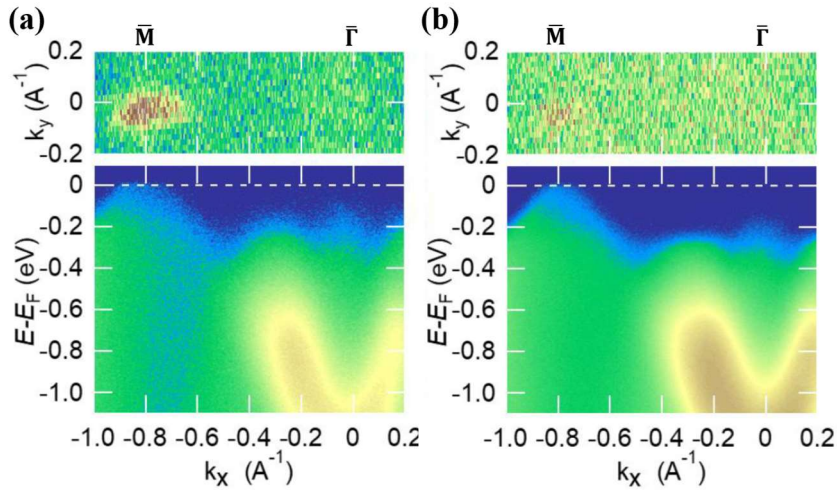

FIGURE 2. ARPES images of $Pb_xSn_{1-x}Te$ (111) films with Pb content (a) $x = 0.17$ and (b) $x = 0.23$, both co-doped with Sb with a concentration of 1%. The measurement was done with the same condition as in Fig. 1. The horizontal axis is taken along the $\bar{\Gamma}$-$\bar{M}$ direction. The equi-energy mapping images at the Fermi level are shown in the top panel.

REFERENCES

1. T. H. Hsieh, H. Lin, J. Liu, W. Duan, A. Bansil, and L. Fu, Nat. Commun. **3**, 982 (2012).
2. Y. Tanaka, Z. Ren, T. Sato, K. Nakayama, S. Souma, T. Takahashi, K. Segawa, and Y. Ando, Nat. Phys. **8**, 800 (2012).
3. S. –Y. Xu *et al.*, Nat. Commun. **3**, 1192 (2012).
4. Y. Tanaka, T. Sato, K. Nakayama, S. Souma, T. Takahashi, Z. Ren, M. Novak, K. Segawa, and Y. Ando, Phys. Rev. B **87**, 155105 (2013).
5. C. Yan et al., Phys. Rev. Lett. **112**, 186801 (2014).
6. R. Ishikawa, T. Yamaguchi, Y. Ohtaki, R. Akiyama, S. Kuroda, J. Cryst. Growth **453**, 124 (2016).
7. P. S. Mandal *et al.*, Nat. Commun. **8**, 68 (2017).

ARPES Study of The Evolution of Electronic Structures of Yb-Doped SmB$_6$

ShaozhuXiao[a], YaFeng[a], TaoWu[b], Eike F. Schwier[c], Kenya Shimada[c] and ShaolongHe[a],

[a]*Ningbo Institute of Materials Technology and Engineering,Chinese Academy of Sciences, Ningbo, Zhejiang 315201, China*
[b]*University of Science and Technology of China, Hefei, Anhui230026, China*
[c]*Hiroshima Synchrotron Radiation Center, Hiroshima University, Higashi-Hiroshima 739-0046, Japan*

SmB$_6$, the first mixed valence material and first Kondo insulator identified in the 1960s, is a bad metal at high temperature, and behaves with a metal to insulator transition as temperature decreased [1]. The metal to insulator transition of SmB$_6$ is due to the hybridization of the localized f electrons with conduction d electrons which opens a narrow band gap on the order of ~10 meV at low temperatures and the Fermi level lies in the gap. This effect lead SmB$_6$ to a resistivity raising with temperature decreasing and the resistivity behaves saturation at about 3 K instead of diverging as in an insulator, which was initially thought to originated from in-gap states such as bulk impurity states [2, 3]. However, recent transport experiments performed on SmB$_6$ suggest that the residual conductivity is originated from the surface-dominated transport state and SmB$_6$ is identified to possess a conductive surface state with perfect insulating bulk state [4-6]. Moreover, the presence of topological protected surface states in the gap of SmB$_6$ have been directly observed by angle resolved photoemission spectroscopy (ARPES) and quantum oscillation experiments [7, 8]. Therefore, SmB6 is identified as an ideal Kondo topological insulator candidate [9, 10].

The valence number of Sm ion is mixed between 2^+ and 3^+ [11] and is an important issue for the theory of the proposed topological character of SmB$_6$. For Yb-doped Sm$_{1-x}$Yb$_x$B$_6$, the valence of Sm Linearly changes with increasing x, from 2.6^+ to 3^+ as x increased from 0 to 1 [12].Transport measurements shows that Sm$_{1-x}$Yb$_x$B$_6$experience an insulator to metal transition with x increased up to about x=0.3 at temperature of 2 K. The theory and the relationship between the metal-to-insulator transition and Sm valence variation are still remained to be uncovered.

Sm$_{1-x}$Yb$_x$B$_6$ is too stiff to be cleaved to obtain a smooth surface large enough. In this work, we usedLaser μ-ARPES, which has small beam spot with size of several μm and high spatial resolution, to overcome this problem to study the electronic structures of Sm$_{1-x}$Yb$_x$B$_6$. Up to now, only the sample with x = 0.3 was successfully cleaved and measured, and the results are shown in Fig. 1. In Circular and P polarization geometry, the hybridization between the flat *f* bands and the conduction*d* bands can be seen (guide lines for eyes in Fig. 1b), which are further confirmed by the MDCs along the flat *f* bands at binding energies of 18 meV and 172 meV (see Figs. 1d and 1e).
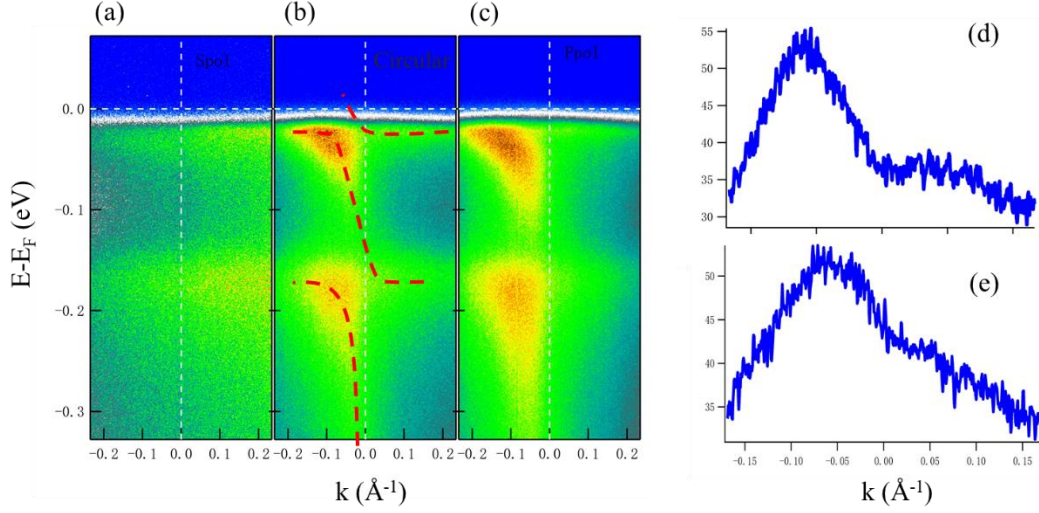
FIGURE 1. Electronic structure of $Sm_{0.7}Yb_{0.3}B_6$ measured by μ-Laser ARPES (hν = 6.3 eV) at 19 K in the (a) S polarization geometry, (b) Circular polarization geometry and (c) P polarization geometry, respectively. (d-e) Momentum distribution curves (MDCs) extracted from image (b) along the flat f bands at binding energies of (d) 18 meV and (e) 172 meV.

REFERENCES

1. A. Menth, E. Buehler, and T.H. Geballe, Phys.Rev. Lett. 22, 295–297 (1969).
2. Allen J W, Batlogg B and Wachter P, Phys. Rev. B 20, 4807 (1979).
3. Sluchanko N E et al., Phys. Rev. B 61, 9906 (2000).
4. Kim D J et al., Sci. Rep. 3 3150 (2013).
5. Wolgast S et al., Phys. Rev. B 88, 180405 (2013).
6. D. J. Kim, J. Xia and Z. Fisk, Nature Materials. 13, 466 (2014).
7. H. Miyazaki et al., Phys. Rev. B 86, 075105 (2012).
8. G. Li et al., Science 346, 1208–1212 (2014).
9. N. Xu, H. Ding and M. Shi, J. Phys.: Condens. Matter. 28, 363001 (2016).
10. F. Lu, J. Z. Zhao, H.Weng, Z. Fang, and X. Dai, Phys. Rev. Lett. 110, 096401 (2013).
11. E. E. Vainshtein, S. M. Blokhin, and Y. B. Paderno, Sov. Phys. Solid State 6, 2318 (1965).
12. J. M. Tarascon et al., J. physique 41, 1135-1140 (1980).

The ARPES Studies on Nodal-line Semimetal LaSbTe

Yang Wang[1], Wenjuan Zhao[1], Guodong Liu[1,*], E. Schwier[2], K. Shimada[2], and Xingjiang Zhou[1,*]

[1]National Laboratory for Superconductivity, Beijing National Laboratory for Condensed Matter Physics, Institute of Physics, Chinese Academy of Sciences, Beijing 100190, China
[2]Hiroshima Synchrotron Radiation Center, Hiroshima University, 2-313 Kagamiyama, Higashi-Hiroshima, Hiroshima 739-0046, Japan

Keywords: nodal-line semimetal, diamond fermi surface , ARPES.

The original title for this proposal is "ARPES studies on the electronic structure of 2D layered van der Waals (vdW) ferromagnetic semiconductor CrI3". However, we found that the atomic-layer-thick 2D CrI3 is extremely sensitive to air. After being prepared, it got damaged in a short time in our lab. It is impossible for us to safely transport the samples to HiSOR. Therefore, we used the beam time to investigate the interesting nodal-line semimetal LaSbTe. In the following, we describe the research progress on this material.

Materials with exotic topological properties have evoked great interests in the field of condensed matter physics since the discovery of topological materials. Searching for new topological materials in experiments is one of the direction of efforts all the time. In the past few years, the first-principle calculations had predicted that LaSbTe is a new nodal-line semimetal when SOC is neglected[1]. However, there are no direct experiment evidences demonstrating it`s topological properties. From the point of this view, we studied the electronic structure of LaSbTe for the first time via angle-resolved photoelectronic emission spectroscopy experiments. We have measured the fermi surface and the band structures along high symmetry directions with different photon energy. We found that it has a diamond-shaped topological fermi surface and Dirac band in Γ-M and X-M direction that are consistent with our band theory calculation. Our results provide clear evidence that LaSbTe is a nodal-line semimetal.

In Fig.1(a), it shows the crystal structure of LaSbTe which has the tetragonal lattice formed by Sb atom. Fig.1(b) shows the fermi surface and constant energy contour of LaSbTe by ARPES measurement with 55eV photon energy. We found that it has a diamond-shaped topological fermi surface arising from Sb atom square similar to the case of ZrSiS [2][3].
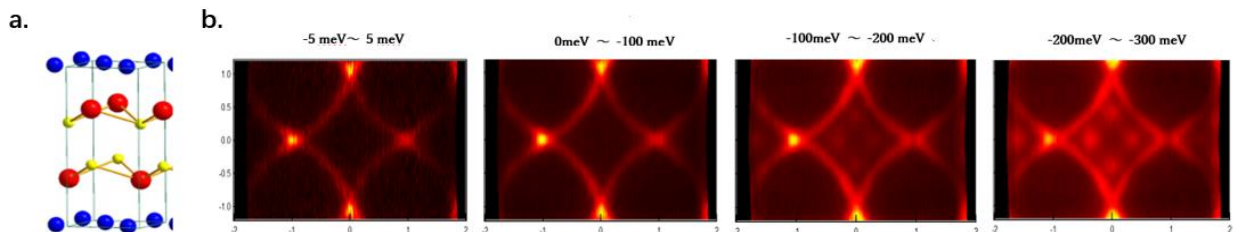

Figure 1. Fermi surface and constant energy contour of LaSbTe. (a) The crystal structure of LaSbTe. The red and yellow balls stand for La and Te atoms respectively and the blue ball stands for Sb atom which forms a square lattice. (b)Fermi surface and constant energy contour of LaSbTe by ARPES measurements with 55eV photon energy, demonstrating that it possesses a topological diamond-shaped fermi surface.

Fig.2(a) shows the band structure of LaSbTe by using first-principle calculation. According to the band calculation, LaSbTe is a Dirac nodal-line semimetal when SOC is neglected. Fig.2(b) shows the core level photoemission spetrum of LaSbTe. In fig.2(c), the electronic band structures of LaSbTe which are measured by different photon energy along all high symmetry directions are shown. The Dirac band are observed in Γ-M and X-M direction which is consistent with our band calculation. Our results indicate that LaSbTe is a Dirac nodal-line semimetal.
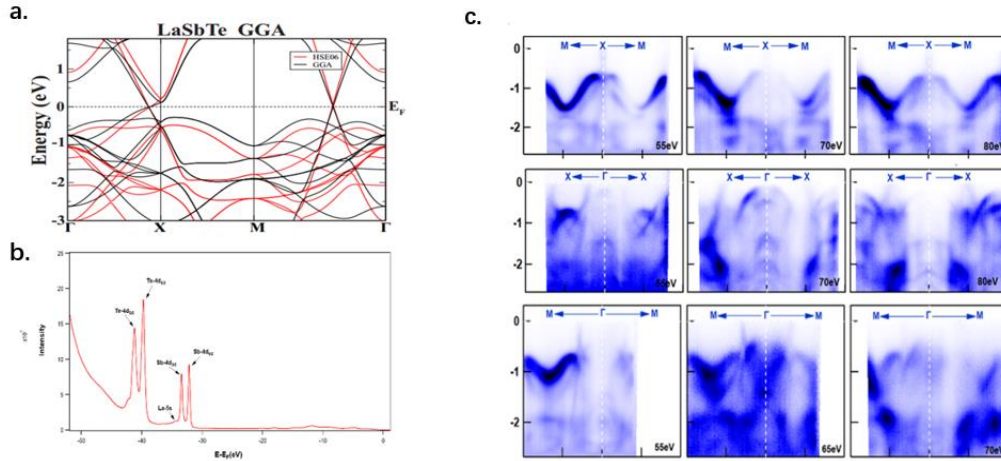

Figure2. The band structure of LaSbTe. (a) The band structure of LaSbTe obtained by using first-principle calculation [1]. (b) The core level spectrum of LaSbTe acquired by ARPES expements with 55eV photon energy. (c) The electronic band structure of LaSbTe along several high symmety directions with different photon energy. We found that there is a topological Dirac band around X point along X-M direction which is contributed by bulk states. In Γ-M direction, another Dirac band is observed in our measurements which is consistent with first-principle calculation [1].

REFERENCES

1. X. Dai et al., *PHYSICAL REVIEW B 92, 205310 (2015)*.
2. Christian R. Ast et al, ncomms11696.
3. Guang-Hao Hong et al, CPB Vol.27,No.1(2018) 017105.

Excitonic correlation effect in multi-band superconductors

T. Mizokawa[a], Y. Matsuzawa[a], T. Morita[a], N. L.Saini[b], T. Asano[c], T. Nakajima[c],
R. Higashinaka[c], T. D. Matsuda[c], Y. Aoki[c], E. F. Schwier[d], and K. Shimada[d]

[a] *Department of Applied Physics, Waseda University, Shinjuku-ku, Tokyo 169-8555, Japan*

[b] *Department of Physics, University of Roma "La Sapienza", Piazzale Aldo Moro 2,*
00185 Roma, Italy

[c] *Department of Physics, Tokyo Metropolitan University, Hachioji 192-0397, Japan*

[d] *HiSOR, Hiroshima University, Higashihiroshima, Hiroshima 739-0046, Japan*

Since the discovery of a BiS_2-based superconductor by Mizuguchi *et al*. [1], a family of BiS_2-based superconductors including $RE(O,F)BiS_2$ (RE=rare-earth element) have been investigated extensively by means of various experimental techniques [2-7]. In $REOBiS_2$ with REO blocking layer, the F substitution for O introduces electrons to the BiS_2 layer. The theoretical calculations indicate that the Fermi surfaces constructed from the Bi $6p_x$ and $6p_y$ orbitals cover the entire Brillouin zone when x is as large as 0.5[2]. The orbital component of the Fermi surfaces has been identified by means of polarization dependent angle-resolved photoemission spectroscopy (ARPES) in $Ce(O,F)BiS_2$ which is consistent with the theoretical predictions [8]. However, the observed Fermi surfaces for $CeO_{0.5}F_{0.5}BiS_2$ are rather small and located around X point of the Brillouin zone. Sugimoto *et al*. argued that Bi $6p_z$ orbitals can accommodate some electrons that do not contribute to the Fermi surfaces. If the Bi $6p_z$ electrons and Bi 6s-S 3p holes have a kind of excitonic correlation, the localized electron-hole pair can couple with asymmetric distortion of BiS_5 pyramids. In order to understand the effect of electron-hole correlation in the BiS_2-based superconductors, we have performed ARPES on $Pr(O,F)BiS_2$ (x=0.0, 0.3, and 0.5) at BL-1, HiSOR.

The electron pocket observed around X point is shown for x=0.5 in Fig. 1. The shape of the electron pockets and the dispersion of the electron bands are symmetric around X point. This behavior is canonical for $RE(O,F)BiS_2$ with RE=La, Ce, and Nd and is consistent with the band-structure calculation for x=0.2 [9-11]. On the other hand, as shown in Fig. 2, the shape of the electron pocket is considerably distorted for x=0.3 indicating that the orbital component is different from the prediction of the band-structure calculation. The difference between $Ce(O,F)BiS_2$ and $Pr(O,F)BiS_2$ would be derived from the mixed valence of the rare-earth elements. In case of $Ce(O,F)BiS_2$, Ce^{4+} component decreases with the F doping, indicating that considerable amount of Bi $6p_z$ electrons should exist in x=0.0. In going from x=0.0 to 0.5, the electrons in the Bi $6p_z$ orbitals are transferred to the Bi $6p_x$ and Bi $6p_y$ orbitals and the electron pockets at X point are formed. In case of $Pr(O,F)BiS_2$, Pr^{4+} component does not change appreciably with the F doping [9]. The present work has revealed that even $PrOBiS_2$ has the electron pockets at X point suggesting that the Bi $6p_z$ orbitals do not accommodate electrons and only the Bi $6p_x$ and $6p_y$ orbitals form the electron pockets due to the self-doping by Pr^{4+}. With the F doping, the doped electrons partly contribute to increase the volume of the electron pocket and are partly trapped in the Bi $6p_z$ orbitals. As shown in the right panel of Fig. 2, x=0.3 exhibits the anisotropic band dispersion down to -0.2 eV below the Fermi level. Therefore, one can exclude possibility of partial elimination of the Fermi surfaces or pseudogap opening. Since the entire electron band becomes anisotropic, one possible explanation is a kind of Jahn-Teller effect in which degeneracy between the Bi $6p_x$ and $6p_y$ orbitals is lifted due to local lattice distortion from tetragonal to orthorhombic. The distortion can be induced by excitonic correlation between Bi $6p_x$/$6p_y$ electron and Bi 6s-S 3p hole. In order to understand dynamics of such correlation, time-resolved ARPES on $Pr(O,F)BiS_2$ should be done in future.
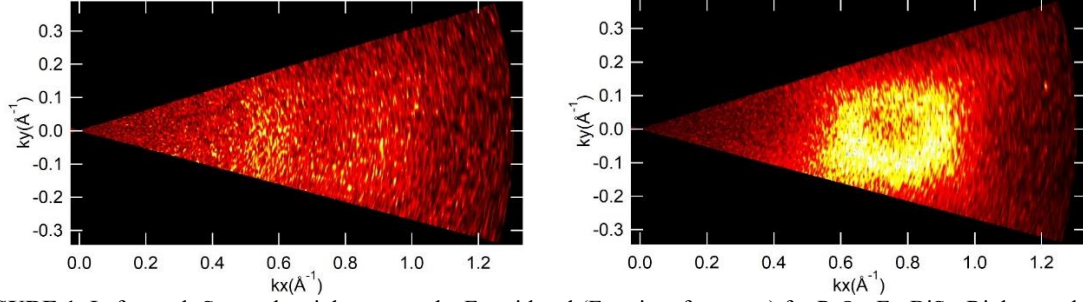
FIGURE 1. Left panel: Spectral weight map at the Fermi level (Fermi surface map) for $PrO_{0.5}F_{0.5}BiS_2$. Right panel: Spectral weight map at -0.2 eV for $PrO_{0.5}F_{0.5}BiS_2$. hν=30eV and T=20 K.
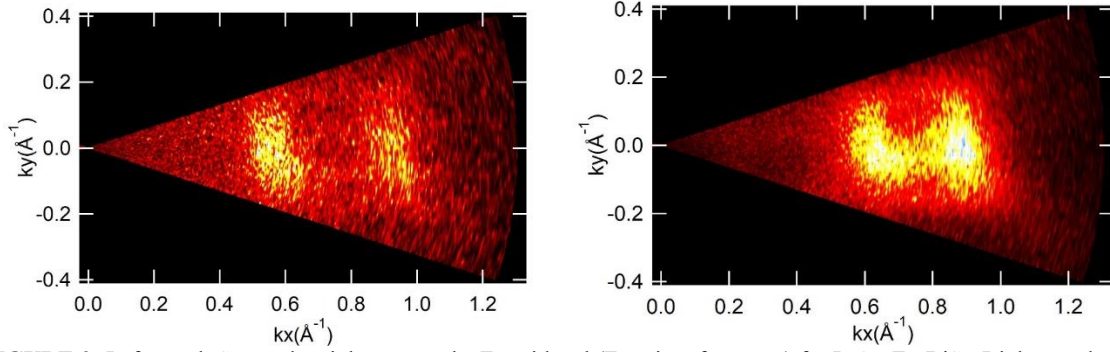

FIGURE 2. Left panel: Spectral weight map at the Fermi level (Fermi surface map) for $PrO_{0.7}F_{0.3}BiS_2$. Right panel: Spectral weight map at -0.2 eV for $PrO_{0.7}F_{0.3}BiS_2$. hν=30eV and T=20 K.

REFERENCES

1. Y. Mizuguchi, H. Fujihisa, Y. Gotoh, K. Suzuki, H. Usui, K. Kuroki, S. Demura, Y. Takano, H. Izawa, and O. Miura, *Phys. Rev. B* **86**, 220510(R) (2012).
2. H. Usui, K. Suzuki, and K. Kuroki, *Phys. Rev. B* **86**, 220501(R) (2012).
3. S. Demura, Y. Mizuguchi, K. Deguchi, H. Okazaki, H. Hara, T. Watanabe, S. J. Denholme, M. Fujioka, T. Ozaki, H. Fujihisa, Y. Gotoh, O. Miura, T. Yamaguchi, H. Takeya, and Y. Takano, *J. Phys. Soc. Jpn.* **82**, 033708 (2013).
4. T. Sugimoto, B. Joseph, E. Paris, A. Iadecola, T. Mizokawa, S. Demura, Y. Mizuguchi, Y. Takano, and N. L. Saini, *Phys. Rev. B* **89**, 201117(R) (2014).
5. S. Demura, K. Deguchi, Y. Mizuguchi, K. Sato, R. Honjyo, A. Yamashita, T. Yamaki, H. Hara, T. Watanabe, J. Denholme, M. Fujioka, H. Okazaki, T. Ozaki, O. Miura, T. Yamaguchi, H. Takeya, and Y. Takano, *J. Phys. Soc. Jpn.* **84**, 024709 (2015).
6. T. Machida, Y. Fujisawa, M. Nagao, S. Demura, K. Deguchi, Y. Mizuguchi, Y. Takano, and H. Sakata, *J. Phys. Soc. Jpn.* **83**, 113701 (2014).
7. Masanori Nagao, Akira Miura, Satoshi Demura, Keita Deguchi, Satoshi Watauchi, Takahiro Takei, Yoshihiko Takano, Nobuhiro Kumada, Isao Tanaka, *Solid State Commun.* **178**, 33 (2014).
8. T. Sugimoto, D. Ootsuki, C. Morice, E. Artacho, S. S. Saxena, E. F. Schwier, M. Zheng, Y. Kojima, H. Iwasawa, K. Shimada, M. Arita, H. Namatame, M. Taniguchi, M. Takahashi, N. L. Saini, T. Asano, R. Higashinaka, T. D. Matsuda, Y. Aoki, T. Mizokawa, *Phys. Rev. B* **92**, 041113 (2015).
9. Z. R. Ye, H. F. Yang, D. W. Shen, J. Jiang, X. H. Niu, D. L. Feng, Y. P. Du, X. G. Wan, J. Z. Liu, X. Y. Zhu, H. H. Wen, and M. H. Jiang, *Phys. Rev. B* **90**, 045116 (2014).
10. L. K. Zeng, X. B. Wang, J. Ma, P. Richard, S. M. Nie, H. M. Weng, N. L. Wang, Z. Wang, T. Qian, and H. Ding, Ph*ys. Rev. B* **90,** 054512 (2014).
11. N. L. Saini, D. Ootsuki, E. Paris, B. Joseph, A. Barinov, M. Tanaka, Y. Takano, T. Mizokawa, *Phys. Rev. B* **90**, 214517 (2014).
12. S. Dash, T. Morita, K. Kurokawa, Y. Matsuzawa, N. L. Saini, N. Yamamoto, Joe Kajitani, R. Higashinaka, T. D. Matsuda, Y. Aoki, and T. Mizokawa, *Phys. Rev. B* **98**, 144501 (2018)

The Electronic Structure Investigation
on Pd Doped SrIrO$_3$ Thin Film

Takashi Komesu[a], Prescott E. Evans [a], Andrew J. Yost [a]
Eike F. Schwier[b], Kenya Shimada[b],
Le Zhang[a], Xia Hong[a] and P. A. Dowben[a]

[a]*Department of Physics and Astronomy, Nebraska Center for Materials and Nanoscience,*
Theodore Jorgensen Hall, 855 N 16th, University of Nebraska, 880299, Lincoln, NE 68588-0299, U.S.A.
[b]*Hiroshima Synchrotron Radiation Center, Hiroshima University, Higashi-Hiroshima 739-0046, Japan*

Keywords: High Resolution Angle Resolved Photoemission Spectroscopy, Electronic Structure, spin-orbital interaction.

The goal of this research is to examine the surface electronic structure in a correlated semi-metallic oxide thin film, orthorhombic SrIrO$_3$ (SIO), which possess strong spin-orbit coupling (SOC). This effort is key to any effort to exploit the interfacial charge and control quantum confinement to tune the relative energy scales of electron correlation. The band structure, mapped at HiSOR, BL-1, using High Resolution Angle Resolved Photoemission Spectroscopy (HR-ARPES), taken at 150 eV photon energy, show the itinerant character for SrIrO$_3$ [1], as seen in Figure 1. Indeed, there is clear evidence for an occupied density of states near the measured Fermi level, away from the Brillouin center, at 0.7 Å^{-1}, as well as
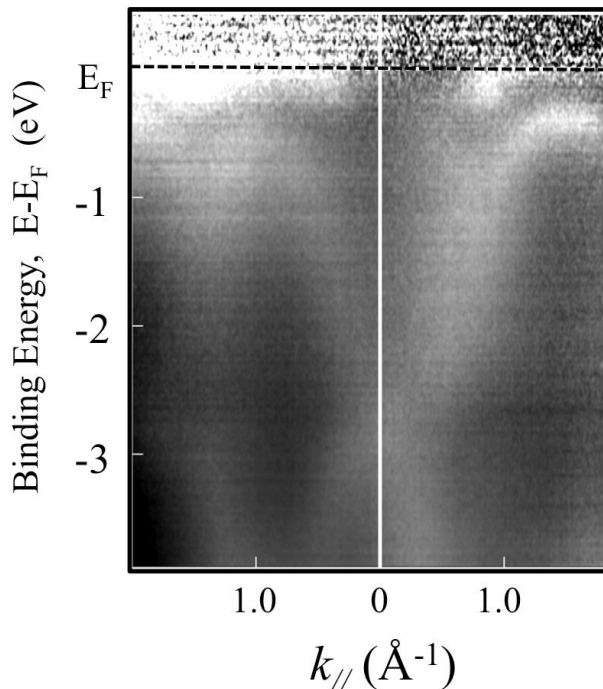

Figure 1. The electronic structure of 5 nm think orthorhombic SrIrO$_3$ single crystal thin films acquired at HiSOR BL1 beam line, taken with 150 eV photon energy, at room temperature.

significant dispersion of the occupied bands, symmetric about the Brillouin zone edge, as is expected [1]. This experimental band structure is completely consistent with the semimetallic character of orthorhombic SrIrO$_3$ [1], but this measured band structure is very different from monoclinic SrIrO$_3$ [2]. It is key to understand that we have now experimentally identified some of the bands predicted by theory, but missing from prior experimental studies [1].

The SrIrO$_3$ samples were prepared by off-axis RF magnetron sputtering, growing the SrIrO$_3$ samples on strontium titanate (SrTiO$_3$). The lattice match of the overlayer and substrate, as seen in Figure 2, is good. Nb doped strontium titanate (SrTiO$_3$) substrates were used for electronic structure investigation. This work, in combination with angle resolved X-ray photoemission, makes clear that the

orthorhombic SrIrO$_3$(001) (SIO) surface is Sr-O terminated and that the surface electronic structure is very different from the bulk.

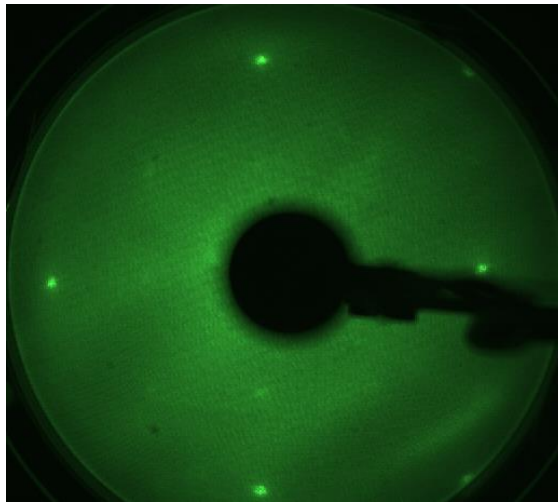Figure 2. X-ray diffraction showing the close lattice match of orthorhombic SrIrO$_3$ (0001), here denoted as SIO, with the strontium titanate (SrTiO$_3$) substrate, denoted as STO.

Figure 3. Low energy electron diffraction of orthorhombic SrIrO$_3$(001) thin films grown on Nb doped strontium titanate (SrTiO$_3$) substrates. The electron energy is 38 eV.

As noted above, Figure 1 shows experimental band structure mapping of orthorhombic SrIrO$_3$(001), as taken at HiSOR, at room temperature. The surface Brillouin zone, from the band structure, is consistent with the (001) surface, as determined by low energy diffraction (LEED) shown in Figure 3, but not perturbed by the 2x2 surface reconstruction hinted at in the low energy electron diffraction (there is little evidence of band folding), suggesting that only some of the surface is subject to a surface reconstruction at room temperature.

References

1) Y. F. Nie, P. D. C. King, C. H. Kim, M. Uchida, H. I. Wei, B. D. Faeth, J. P. Ruf, J. P. C. Ruff, L. Xie, X. Pan, C. J. Fennie, D. G. Schlom, and K. M. Shen, Phys. Rev. Lett. 114 (2015) 016401
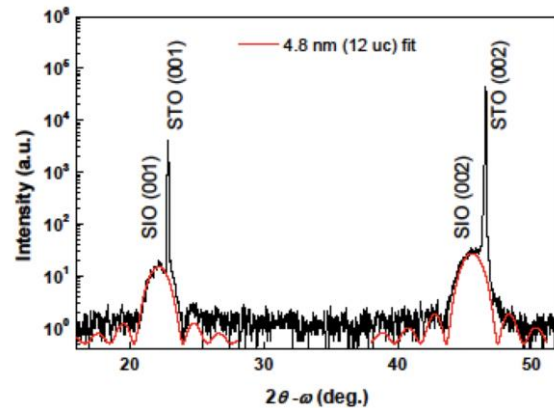2) T. Takayama, A. N. Yaresko and H. Takagi, J. Phys.: Condens. Matter 31 (2019) 074001

Current activities of research and education on BL-5 (FY2018)

T. Yokoya, T. Wakita, Y. Muraoka and K. Terashima

Research Institute for Interdisciplinary Science, Okayama University
Research Laboratory for Surface Science, Okayama University, Okayama 700-8530, Japan

Keywords: photoemission spectroscopy, photoelectron emission microscopy

We present an overview of our resent research and educational activities on beamline 5 (BL5) in the fiscal year 2018. Our beamline has two experimental stations in a tandem way. The first station is equipped with an angle-resolved photoemission spectrometer (ARPES), a low energy electron diffraction (LEED) apparatus and an X-ray source. The hemispherical analyzer of ARPES spectrometer (HA54, VSW) has a mean radius of 50 mm and is mounted on a twin axis goniometer in ultra-high vacuum chamber. Using this goniometer, one can perform ARPES and photoelectron diffraction (PED) measurements. It is also possible to perform resonant photoemission spectroscopy (RPES) measurements by using photon energy tunability of synchrotron radiation with X-ray absorption spectroscopy (XAS) measurement. With the X-ray source (XR2E2, FISONS), we can perform an X-ray photoelectron spectroscopy (XPS) measurement for the chemical state analysis and the PED. At the second station, we have installed a photoelectron emission microscope (PEEM, 'PEEM III', Elmitec). PEEM provides a magnified image of lateral intensity distribution of photo-emitted electrons from a sample surface. The spatial resolutions are several ten nanometers with Hg lamp and a few micrometers with synchrotron radiation. The sample is transferred between the ARPES and the PEEM chamber *in-situ*, and one can perform measurements at both stations for the same sample.

In the recent researches on BL-5, we have studied the electronic structure of potassium doped aromatic molecule (K_x picene) [1], iron-based superconductor ($FeSe_xTe_{1-x}$) [2], transition metal di-oxide films such as VO_2 thin films which exhibits a first-order metal-to-insulator transition at 340 K [3], CrO_2 thin films which are known as a half-metallic material [4], and TaO_2 film which is stabilized with a new technique developed in our group [5]. We have also studied the electronic structures of a high quality boron doped diamond film which shows a signature of the highest superconducting transition temperature of 25 K [6] and a high quality single crystal of $YbFe_2O_4$ which is one of multiferroic materials [7], by utilizing RPES at B-*K* and Fe-$M_{2,3}$ edges, respectively. In this fiscal year, we are studying the charge states of Lu atoms in $Lu_2@C_{82}$ and $Lu_2C_2@C_{82}$ by the photon-energy dependence of the valence band photoemission spectra, as presented in this symposium.

We have used the BL-5 for education activity as well, for example, practical education for undergraduate students of Okayama University. The students have an opportunity to study the synchrotron radiation mechanism and to experience XPS measurement which is very useful for the surface science research. We accepted more than 100 students from 2006 to 2012. From 2014, we have started to join the practical lecture for experiments using the beamline end stations in HiSOR for both graduate school students of Hiroshima and Okayama Universities. In this February, we have started a new project for education under a Japan-Asia youth exchange program in science supported by Japan Science and Technology Agency (JST), "Sakura Exchange Program in Science". We have accepted six students from Changchun University of Science and Technology in China this year.

REFERENCES

1. H. Okazaki *et al.*, *Phys. Rev* **82**, pp. 195114 (5 pp.) (2010).
2. Y. Yoshida *et al.*, *J. Phys. Soc. Jpn* **78**, pp. 034708 (4 pp.) (2009).
3. K. Saeki *et al.*, *Phys. Rev* **80**, pp. 125406 (5 pp.) (2009).
4. Y. Muraoka *et al.*, *MRS Proceedings* **1406** (2012).
5. Y. Muraoka *et al.*, *Thin Solid Films* **599**, pp. 125-132 (2016).
6. H. Okazaki *et al.*, *Appl. Phys. Lett* **106**, pp. 052601 (5 pp.) (2015).
7. K. Fujiwara *et al.*, *Trans. Mater. Res. Soc. Jpn.* **41**, pp. 139-142 (2016).

Development of On-site Cleaning Method of Carbon Contamination with Atomic Hydrogen

Masahito Niibe,[a] Takashi Tokushima[a,b,c], Tomohiko Kono[d], Yusuke Hashimoto[c], Yuka Horikawa[d], and Hiroaki Yoshida[e]

[a]*Laboratory of Advanced Science and Technology for Industry, University of Hyogo, Kamigori, Hyogo, Japan*
[b]*Sanka High Technology Co. Ltd., Tatsuno, Hyogo, Japan*
[c]*MAX IV Lab. Lund Univ., Lund, Sweden*
[d]*Graduate School of Sciences and Technology for Innovation, Yamaguchi University, Yamaguchi, Japan*
[d]*Department of Physical Science, Graduate School of Science, Hiroshima University, Higashi-Hiroshima, Japan*

Carbon contamination of optical elements in synchrotron radiation beamlines is a serious problem [1-4]. In particular, for a mirror coated with easily-oxidizable-metal such as Ni, Cr, etc., carbon cleaning technique by $VU-O_3$ ashing is not applicable since Ozone cause surface oxidation resulting in reflectance lowering. Therefore, the cleaning technique for this kind of mirrors is not established. Recently, we reported off-site cleaning treatment using the atomic hydrogens is very effective in removing contamination of mirrors [5]. In response to this, we received requests from many people to develop atomic hydrogen cleaning equipment that can be used "on-site". Therefore, we began to develop a small on-site cleaning device that can be mounted in a mirror vacuum chamber. Here we report on the first cleaning experiment conducted at the HiSOR beamline BL-6 of Hiroshima University.

Fig. 1 shows the tip portion of the atomic hydrogen generating apparatus. This device consists of tungsten (W) filament, current introducing electrode, hydrogen gas introduction piping, hydrogen gas source and pressure regulator, and DC power supply. These parts can be easily installed in the vacuum chamber of the beam line by fixing/positioning them to the short pipe with ICF-70 flange. By using a container with a low-pressure hydrogen storage alloy as the gas source, hydrogen gas can be easily supplied into the mirror chamber at the synchrotron radiation experimental hall where it is difficult to introduce a high-pressure dangerous gas cylinder. Hydrogen gas is brought introduced in the vacuum chamber to contact with W filaments heated to about 1700 °C for generation of atomic hydrogens by catalytic reaction. As a preliminary experiment to confirm the generation of atomic hydrogens, the device was operated in a vacuum chamber in front of a tungsten oxide powder sample. We have successfully observed the color changes of the powder sample from green to black which is an evidence of the oxide reduction.

FIGURE 1. Tip portion of atomic hydrogen generating apparatus.

The first mirror cleaning experiment using atomic hydrogen was carried out on the cleaning of the contaminated collector mirror of the monochromator in BL-6 of the HiSOR facility. As the installation position of the W filament in two directions, laterally and above side from the mirror, 4 to 5 times of cleaning were attempted, with input power 24 W to 40 W, gas pressure 10 Pa to 50 Pa, and processing time 1 hr. However, carbon contamination could not be removed visually.

Fig. 2 shows the spectra exited from the monochromator before and after the atomic hydrogen treatment. It seems that a slight increase appears in the output of the spectrometer. However, errors due to beam position fluctuations and others like are large, so it is difficult to make an assertive conclusion. Insufficient improvement of the mirror reflectivity seems to be caused by insufficient input power and insufficient generation of atomic hydrogens.
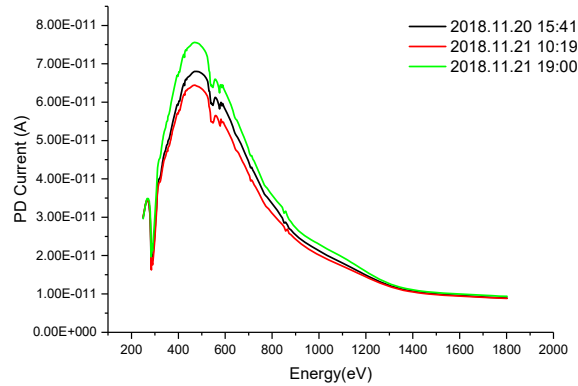

FIGURE 2. Spectra emitted from the monochromator before and after the atomic hydrogen treatment.

In the future, we plan to improve the shape of the filament or heater so that we can introduce larger electric power and generate more atomic hydrogen.

REFERENCES

1. K. Boller, R.-P.Haelbich, H. Hogrefe, W. Jark and C. Kunz, Nuclear Instrum. Method. **208**, 273-279 (1983).
2. T. Koide, S. Sato, T. Shidara, M. Niwano, M. Yanagihara, A. Yamada, A. Fujimori, A. Mikuni, H. Kato and T. Miyahara, Nuclear Instrum. Method. Phys. Research A**246**, 215–218 (1986).
3. R. A. Rosenberg, Nuclear Instrum. Method. Phys. Research A**291**, 101–106 (1990).
4. R. Kohli and K.L. Mittal Ed., *Developments in Surface Contamination and Cleaning* (Elsevier, Amsterdam, 2015).
5. M. Niibe, T. Harada, A. Heya, T. Watanabe, and N. Matsuo, *AIP Conf. Proc.*, **2054**, 060010 (2019).

Ex-situ/In-situ Soft X-ray Absorption Investigation Towards Corrosion of Cu and Passivation Behavior of Ti

Ying Jin[a], Qingrui Wang[a], FeiFei Huang[a], Yi-Tao Cui[b], Hiroaki Yoshida[c] and Takashi Tokushima[d]

[a]*National Center for Materials Service Safety, University of Science and Technology Beijing, No.30, Xueyuan Road, Haidian District, Beijing P.R. CHINA*
[b]*SANKA High Technology Co. Ltd. 90-1,Kurimachi, Shingu-machi, Tatsuno, Hyogo,679-5155,Japan*
[c]*Department of Physical Science, Hiroshima University, 1-3-1 Kagamiyama, Higashi-Hiroshima, 739-8526, Japan*
[d] *MAX IV Laboratory Lund University, Box 117, 221 00 Lund, Sweden*

Keywords: TC4, passive film, XAS, XPS, EIS, Mott-schottky

Passivation is the contributor for metals-based civilization since the active metals (Fe, Cr, Al, and Ti, etc.) show excellent kinetic stabilities in oxidizing service environments [1]. Owing to their high strength-to-weight ratios, superior fatigue strengths, modulus of elasticity and especially high corrosion resistance [2]. These metals and their alloys have been extensively used in kinds of fields. So copper (Cu), titanium (Ti) and their alloys are the most important materials having a wide range of application in many industries such as electronic equipment, architectural engineering materials, marine equipment, and aeronautical material etc. However, they may suffer damaging effects in corrosive environment.

This passive film provides Ti with the resistance to corrosion as long as the integrity of the film is maintained. However, the nature, composition, and thickness of this protective film depends on the environmental conditions [3]. In order to investigate the effects of potentials and time on formation and failure mechanisms of passivation comprehensively, as shown in figure 1, we have chosen commercial samples of TC4 (Ti-6Al-4V) to do potentiostatic control at -0.6, 0, 0.5, 1.0, 1.5, 2.3 V (vs Ag/AgCl reference electrode) for 12 hrs, and at 1.0V for 2, 4, 8, 12, 24 hrs respectively in 0.5 M sulfuric to form the passive film.
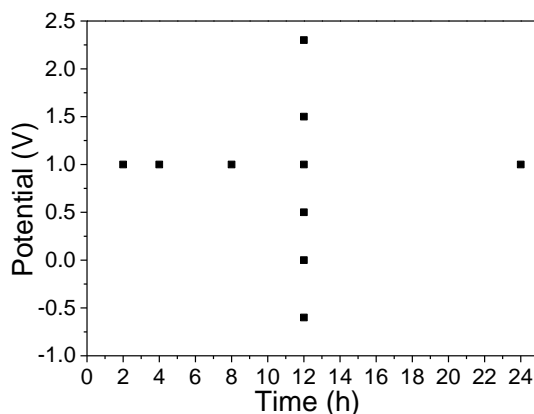

FIGURE 1. The conditions for potentiotatic control

To further understand the passivation, surface characterization techniques are often used. X-ray Absorption Specstroscopy (XAS) is employed to reveal complex compositions and chemical states within the film (as the figure 2 shows), also can support the data of X-ray Photoelectron Spectroscopy (XPS). Auger Electron Spectroscopy (AES) is employed to reveal composition and thickness of passive Film. Beside, Electrochemical impedance spectroscopy (EIS) is employed using a frequency range of 100 kHz to 10 mHz , at 0 V (vs open circuit potential) and with a 10 mV amplitude of the alternating current (AC) signal to reveal

corrosion resistance of the passive film. And Mott-schottky measurements is employed using a potential fange from the film-formed potential to -1 V (vs Ag/AgCl reference electrode) at 1000Hz and with a 10 mV amplitude of the AC signal to reveal semiconductive property of the passive film.
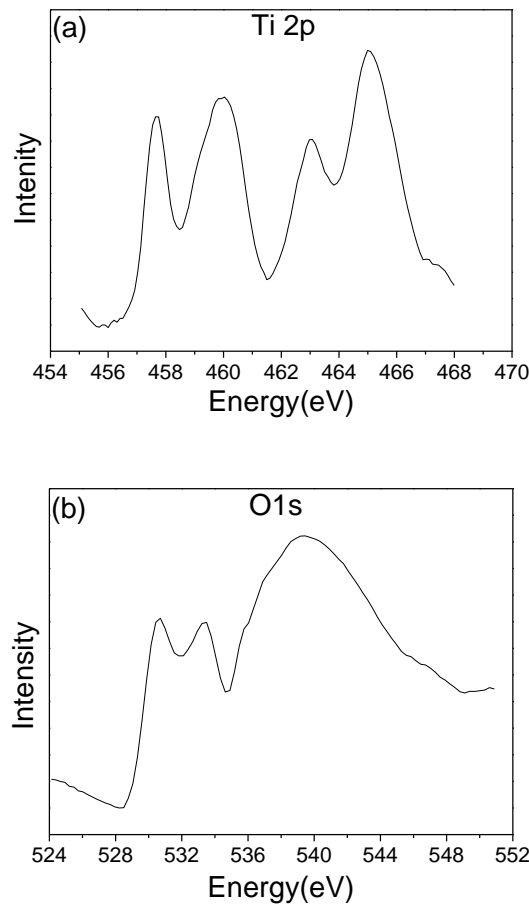

FIGURE 2. The XAS (Ti 2p and O 1s) of TC4 in 0.5 M sulfuric acid

The main findings are summarized as follows:

(a) The thickness of the passive film is proportional to the potential of titanium in potentiostatic control.

(b) The predominant oxide formed on titanium is TiO_2, and with the increase of depth, the film is not completely oxidized because of the rapid increase of suboxides TiO and Ti_2O_3.

(c) The corrosion resistance of the passive film in passive region is proportional to the potential in potentiostatic control. Suggesting that the worst corrosion resistance of passive film is formed in cathodic region, and the medium corrosion resistance of passive film is generated in dissolve region, and the best protective passive film is formed in passive region.

(d) All the slopes of M-S plots are positive, implying the n-type semi-conductive character of the passive film on TC4 [4]. And the semiconductive property of the passive film is also related to the potential of potentiostatic control.

REFERENCES

1. Macdonald D D. The Passive State in Our Reactive Metals-Based Civilization [J]. Arabian Journal for Science & Engineering, 2012, 37(5):1143-1185.
2. Pang J, Blackwood D J. Corrosion of titanium alloys in high temperature near anaerobic seawater [J]. Corrosion Science, 2016, 105:17-24.
3. Perini N, Corradini P G, Nascimento V P, et al. Characterization of AISI 1005 corrosion films grown under cyclic voltammetry of low sulfide ion concentrations[J]. Corrosion Science, 2013, 74(Complete):214-222.
4. Li D, Wang J, Chen D, et al. Influence of passive potential on the electronic property of the passive film formed on Ti in 0.1M HCl solution during ultrasonic cavitation[J]. Ultrasonics Sonochemistry, 2016.

Photoelectron spectroscopy of YbCu$_x$ systems

Hitoshi Yamaoka[a], Hitoshi Sato[b], Naohito Tsujii[c], and Kenya Shimada[b],

[a]*RIKEN SPring-8 Center, 1-1-1 Kouto, Sayo, Hyogo 679-5148, Japan*
[b]*Hiroshima Synchrotron Radiation Center, Hiroshima University, Higashi-Hiroshima, Hiroshima 739-0046, Japan*
[c]*International Center for Materials Nanoarchitectonics (MANA), National Institute for Materials Science, 1-2-1 Sengen, Tsukuba, Ibaraki 305-0047, Japan*

Keywords: photoelectron spectroscopy, YbCu$_x$, temperature dependence

In rare-earth compounds some of elements such as Yb, Eu, Sm, and Ce often show the valence instability between the two charge states. The $4f$ electrons of these elements have localized nature, while the electronic state of the $4f$ electrons in the compounds is the result of the hybridization of the $4f$ electrons with conduction (c) electrons (c-f hybridization) which is characterized by the Kondo temperature. The valence of the rare-earth elements of these compounds is a measure of the c-f hybridization and the Kondo temperature. Temperature or pressure is a prominent tool to control the c-f hybridization or the Kondo temperature.

Here, we study the electronic structures of the Yb-Cu binary alloy systems, the compositions of YbCu, YbCu$_2$, YbCu$_{4.5}$, YbCu$_5$, and YbCu$_{6.5}$, systematically. We measured the valence band spectra as shown in Figs. 1(a)-1(c). The intensity is normalized by the area. The resonant increase of the intensity of the Yb^{3+} component was observed at the $4d$-$4f$ resonant energy of 182 eV. The data shown here were measured at the off-resonant energy of 176 eV. The broad and large peak around 2-5 eV is the component of Cu $4d$. The intensity of the Yb^{3+} component in YbCu and YbCu$_2$ is very small, suggesting nearly divelent Yb state of these compounds and supporting the results of the measurements of the PFY-XAS at SPring-8. The valence band spectra of YbCu$_2$ reproduced the spectra measured previously [1].

Another remarkable issue is the difference of the Cu $3d$ component. The electronic structure of the Cu $3d$ component of YbCu, YbCu$_{4.5}$, YbCu$_5$, and YbCu$_{6.5}$ are similar, but different from YbCu$_2$. The width of the Cu-$3d$ component increased with increasing the Cu content. The Cu $3d$ component consists of mainly two peaks and the separation of the two peaks of YbCu$_2$ is much larger than others.

Temperature dependence of the valence band spectra were measured for YbCu, YbCu$_2$, YbCu$_{4.5}$, and YbCu$_5$ as shown in Figs. 1(d)-1(m). No temperature dependence was observed in YbCu and YbCu$_2$ and the results of PES agree with those of XES. While the valence band spectra of YbCu$_{4.5}$ and YbCu$_5$ show weak temperature dependence. In YbCu$_{4.5}$ the intensity of the $4f$ peak increased with decreasing the temperature. This indicated the increase of the Yb devalent state and agrees with the previous measurements of the PFY-XAS spectra [2].

On the other hand, the Yb^{3+} component showed a unique temperature dependence which has never been observed in the other Yb compounds. The peaks of Yb^{3+} components are assigned as shown in Fig. 1(j) from the analogy to the spectra of Yb$_2$Pd$_2$Sn [3]. Shifts to the lower-biding energy were observed in the peaks of ^{3}P and ^{1}D, while other peaks keep the same energy positions and the intensity of the peaks in ^{1}I, ^{3}H, ^{3}F, and ^{3}H increased and that in ^{1}D decreased with decreasing the temperature. At present we do not understand the mechanism of the phenomena. But this temperature-induced behavior may correlate to the existence of three types of Yb sites and complex crystal structure in YbCu$_{4.5}$.

In YbCu$_5$ we observe a slight increase of the intensity of the Yb^{2+} component as shown in Fig. 1(l). But it is difficult to see the temperature-induced change in the intensity of the Yb^{3+} component as shown in Fig. 1(m). The Yb valence changed approximately from 2.97 at 300 K to 2.94 at 18 K [4]. It may be too small to observe as the change in the intensity of the Yb^{3+} component of the valence band spectra clearly.
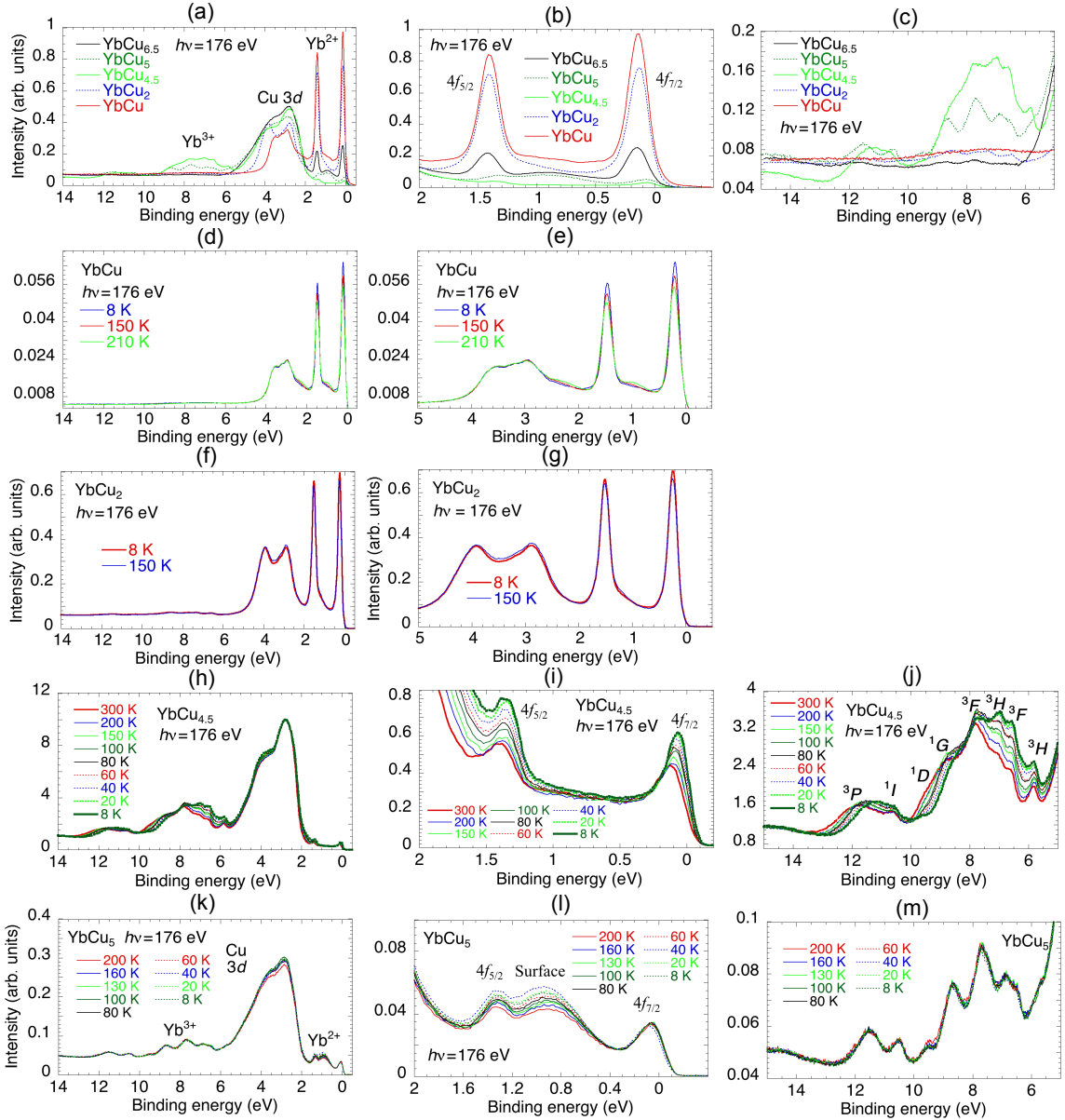
FIGURE 1. (a) Comparison of the valence band spectra of YbCu, YbCu$_2$, and YbCu$_{4.5}$ at 8 K and that of YbCu$_{6.5}$ at 200 K ($h\nu$=176 eV). (b) Expanded view of the spectra near the Fermi level in (a). (c) Expanded view of the spectra around Yb^{3+} component in (a). (d) Valence band spectra of YbCu at 8, 150, and 210 K and at $h\nu$=176 eV. (e) Expanded view of the spectra near the Fermi level in (d). (f) Valence band spectra of YbCu$_2$ at 8 and 150 K and at $h\nu$=176 eV. (g) Expanded view of the spectra near the Fermi level in (f). (h) Valence band spectra of YbCu$_{4.5}$ as a function of temperature at $h\nu$ =176 eV. (i) Expanded view of the spectra near the Fermi level in (h). (j) Expanded view of the spectra around Yb^{3+} component in (h). (k) Valence band spectra of YbCu$_5$ as a function of temperature at $h\nu$=176 eV. (l) Expanded view of the spectra near the Fermi level in (k). (m) Expanded view of the spectra around Yb^{3+} component in (k).

REFERENCES

1. A. Fujimori, T. Shimizu, and H. Yasuoka, Photoemission study of valence fluctuation in YbCu$_2$, Phys. Rev. B **35**, 8945 (1987).

2. H. Yamaoka, N. Tsujii, Y. Yamamoto, Y. Michiue, J.-F. Lin, N. Hiraoka, H. Ishii, K.-D. Tsuei, and J. Mizuki, Reentrant valence transition in YbCu$_{4.5}$ under pressure, Phys. Rev. B **97**, 085106 (2018).

3. H. Yamaoka, P.Thunstrom, N. Tsujii, I. Jarrige, K. Shimada, M. Arita, H. Iwasawa, H. Hayashi, J. Jiang, H. Namatame, M. Taniguchi, N. Hiraoka, H. Ishii, K.-D. Tsuei, M. Giovannini, and E. Bauer, The electronic structure and the valence state of Yb$_2$Pd$_2$Sn and YbPd$_2$Sn studied by photoelectron and resonant x-ray emission spectroscopies, Phys. Rev. B **86**, 085137 (2012).

4. H. Yamaoka, I. Jarrige, N. Tsujii, N. Hiraoka, H. Ishii, and K-D. Tsuei, Temperature dependence of the Yb valence in YbCu$_5$ and YbCu$_{5-x}$Al$_x$ Kondo compounds studied by x-ray spectroscopy, Phys. Rev. B **80**, 035120 (2009).

Observation of Singly Occupied Molecular Orbital in 2-iodo Nitronyl Nitroxide Radical

Hiroaki Anzai[a], Yusuke Ono[a], Ryosuke Takakura[a], Hitoshi Sato[b],
Toshiyuki Matsui[a], Satoru Noguchi[c], and Yuko Hosokoshi[c]

[a] Graduate School of Engineering, Osaka Prefecture University, Sakai 599-8531, Japan
[b] Hiroshima Synchrotron Radiation Center, Hiroshima University, Higashi-Hiroshima 739-0046, Japan
[c] Graduate School of Science, Osaka Prefecture University, Sakai 599-8531, Japan

Keywords: organic radical crystal, electronic structure, photoemission spectroscopy.

Organic radicals that bear an unpaired electron have been focus of research on molecular magnetic materials because of their potential for applications in spintronics devices [1]. The 2-iodo nitronyl nitroxide (INN) is a typical stable radical with spin-density localization on NO groups and forms a chain structure with contact between the NO group and the I atom along the a-axis [2]. It is therefore considered that the intermolecular arrangement of the NO groups is responsible for the ferromagnetic interaction at low temperature.

The intermolecular interaction of INN can be interpreted by the model of charge transfer (CT) between orbitals of two radicals where the electronic configurations of the singly occupied molecular orbital (SOMO) and the next highest molecular orbital (NHOMO) are taken into account [3]. The ferromagnetic electron coupling is favored when spin-triplet state is stabilized after the charge transfer, as shown in Fig. 1(a). The intermolecular overlap and the energy difference of the molecular orbitals are closely related to the exchange interactions [4]. Hence, it is important to identify the SOMO and NHOMO in the valence bands. Previous studies of photoemission spectroscopy on the nitronyl nitroxide radicals have reported the multiple electronic features near Fermi level (E_F) [5,6].

Here, we report the valence-band structure of INN using photoemission spectroscopy with synchrotron radiation. Single crystals of INN with honeycomb lattice were grown by slow evaporation of concentrated solutions. The chemical structure is shown in Fig. 1(b). The experiments were performed at BL-7 of Hiroshima Synchrotron Radiation Center. The data were collected at $T = 300$ K with $h\nu = 60$ eV. Total energy resolution was set to 33 meV. The samples were kept under a high vacuum of 4.7×10^{-9} Torr during the measurements. No beam-induced degradation of the samples was observed.
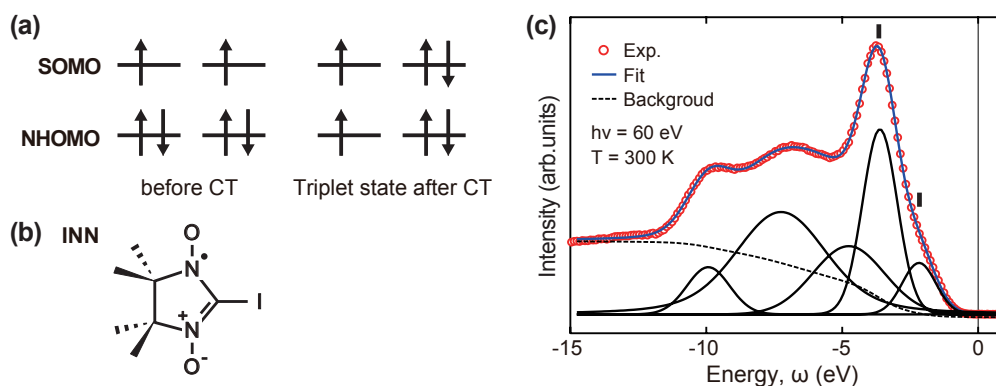

Figure 1. (a) The charge transfer (CT) process within a radical dimer [3]. (b) Chemical structure of INN. (c) Valence-band spectra (circles) of INN taken with $h\nu = 60$ eV at 300 K. The thick blue and black curves represent the result of fitting analysis and the extracted peak components, respectively. The dashed line is a background. Vertical bars indicate peak positions of the SOMO and NHOMO.

Figure 1(c) shows the valence-band spectra of INN. The well-defined sharp and intense peak is observed at $|\omega| \sim 3.6$ eV. Several peaks are also visible at $|\omega| \sim 7.0$ and 10.0 eV. The multiple peak features are in agreement with the previous photoemission studies on the nitroxide radicals [5,6]. We note that there exists a shoulder structure on the low-energy side of the 3.6 eV peak. This first band just below E_F can be attributed to the SOMO, and thus the second peak at 3.6 eV is the NHOMO.

The line shape of the spectra is rigorously determined from a fitting analysis with Voigt functions, as shown by thick blue curves in Fig. 1(c). The energy of SOMO is estimated as $|\omega| \sim 2.1$ eV. The energy difference between the SOMO and NHOMO is 1.5 eV, which is approximately 1.0 eV smaller than the value reported in the organic radical with the intermolecular antiferromagnetic interactions [6]. Indeed, the formation of a chain structure stacked NO group and I atom with short separations leads to an enhanced orbital overlap in the SOMO and NHOMO [2,4]. We considered that the observed SOMO and NHOMO states play an important role in the ferromagnetic interaction with neighboring spins. Further experiments in wide energy and temperature ranges are required to provide the detailed evolution of the ferromagnetic interaction in INN.

In conclusion, we investigated the valence band structure in INN using synchrotron radiation photoemission spectroscopy. The SOMO is observed at $|\omega| \sim 2.1$ eV, for the first time. The energy separation of the SOMO and NHOMO is estimated to be ~1.5 eV, which is ~1.0 eV smaller than the value on the antiferromagnetic compound. These findings indicate that the close intermolecular SOMO-NHOMO contact enhances the intermolecular ferromagnetic interactions of organic radicals.

REFERENCES

1. S. Sanvito, Chem. Soc. Rev. **40**, 3336 (2011).
2. Y. Hosokoshi *et al*., Mol. Cryst. Liq. Cryst. **271**, 115 (1995).
3. K. Awaga *et al*., Mol. Cryst. Liq. Cryst. **232**, 27 (1993).
4. I. Novak *et al*., Chem. Phys. Lett. **413**, 351 (2005).
5. I. Morishima *et al*., Chem. Phys. Lett. **16**, 336 (1972).
6. H. Anzai *et al*., Physica B **536**, 664 (2018).

Photoelectron spectroscopy of Yb$_4T$Ge$_8$ (T = Cr, Mn, Fe, Ni)

Hitoshi Yamaoka[a], Hitoshi Sato[b], Masahito Hikiji[c], Shunsuke Yamanaka[c],
Chishiro Michioka[c], Naohito Tsujii[d], Kenya Shimada[b],
and Kazuyoshi Yoshimura[c]

[a]*RIKEN SPring-8 Center, 1-1-1 Kouto, Sayo, Hyogo 679-5148, Japan*
[b]*Hiroshima Synchrotron Radiation Center, Hiroshima University, Higashi-Hiroshima, Hiroshima 739-0046, Japan*
[c]*Department of Chemistry, Graduate School of Science, Kyoto University, Kyoto 606-8502, Japan,*
[d]*International Center for Materials Nanoarchitectonics (MANA), National Institute for Materials Science, 1-2-1 Sengen, Tsukuba, Ibaraki 305-0047, Japan*

Keywords: photoelectron spectroscopy, Yb$_4T$Ge$_8$, temperature dependence, zero thermal expansion

Materials with zero thermal expansion (ZTE) or negative thermal expansion (NTE) are very rare, and have attracted much interest for their physical mechanism as well as potential technological applications. Yb$_4T$Ge$_8$ (T = Cr, Mn, Fe, Ni, Co) has been found to show ZTE upon cooling. Interestingly, it has been suggested that the ZTE is not originated from the temperature-induced change in the Yb valance [1]. The crystal structure of Yb$_4T$Ge$_8$ is CeNiSi$_2$-type with the space group of *Cmcm*. Yb and Ge zigzag chains are on the Ge square net forming the alternating layers stacked along the long b axis. It was claimed that ZTE was caused by the 3-dimensional geometrical mechanism of the temperature-induced structural modulation arising from the charge transfer from T atoms to the Ge net, destabilizing the square-net structure of Ge [1]. In Yb$_4$FeGe$_8$, Yb$_4$CrGe$_8$, and Yb$_4$CoGe$_8$, the x-ray absorption spectra have been measured at three or four temperature points, indicating the valence fluctuation of Yb. However, detailed study of the temperature dependence of the Yb valence has not been clarified yet. The study of the correlation between the electronic and crystal structures of these ZTE compounds under pressure may provide clues to understand the ZTE mechanism of the valence fluctuation systems. We have measured the temperature and pressure dependence of the Yb valence at SPring-8. Here, complementary to the measurements at SPring-8, we study the temperature dependence of the valence band and core-level spectra of Yb$_4T$Ge$_8$ (T = Cr, Mn, Fe, Ni).

We performed photoelectron spectroscopy to observe the electronic structure below the Fermi level. Figure 1(a) shows incident energy dependence of the valence-band spectra of Yb$_4$MnGe$_8$ at room temperature around Yb $4d$-$4f$ resonance. Resonant enhancement of the intensity of the Yb^{3+} component was observed at 182 eV as in other Yb compounds. In Fig. 1(b) we show an example of wide band spectra of Yb$_4$FeGe$_8$ at on- and off-resonant energies. The temperature dependence of the spectra shown below were measured at off-resonant energy of 176 eV. Figure 1(c) shows a comparison of the valence band spectra of Yb$_4T$Ge$_8$ (T = Cr, Mn, Fe, Ni) at 8 K. The intensity of the Yb^{2+} component is very weak compared to that of the Yb^{3+} component in these four compounds, indicating nearly Yb^{3+} mean valence state. The intensity of the Yb^{2+} component of Yb$_4$FeGe$_8$ is larger than those of the other three compounds and the Yb valence fluctuation of Yb$_4$FeGe$_8$ is relatively stronger than the others. In Yb$_4$CrGe$_8$ there is a broad peak around 4 eV. Figures 1(c) shows a comparison of the Ge $3d$ core-level spectra of Yb$_4T$Ge$_8$ (T = Cr, Mn, Fe, Ni) at 8 K. The peak of Ge $3d$ consists of $3d_{3/2}$ and $3d_{5/2}$. Intensity ratio of $3d_{3/2}$ to $3d_{5/2}$ components depends on T and the intensity of $3d_{5/2}$ of the T = Fe sample is stronger than the others. The intensity of $3d_{3/2}$ at 8 K is stronger than that at 300 K as shown in Figs. 1(d) and 1(e). This may be caused by the increase of the intensity of the tail component above the binding energy of 30 eV at low temperatures. The intensity of the Yb^{2+} component increased at low temperatures as shown in Figs. 1(f), 1(i), 1(f), and 1(o). The spectra of the Yb^{3+} component shift to the lower binding energy at low temperatures. This temperature-induced behavior has not been observed so far in the Yb compounds.
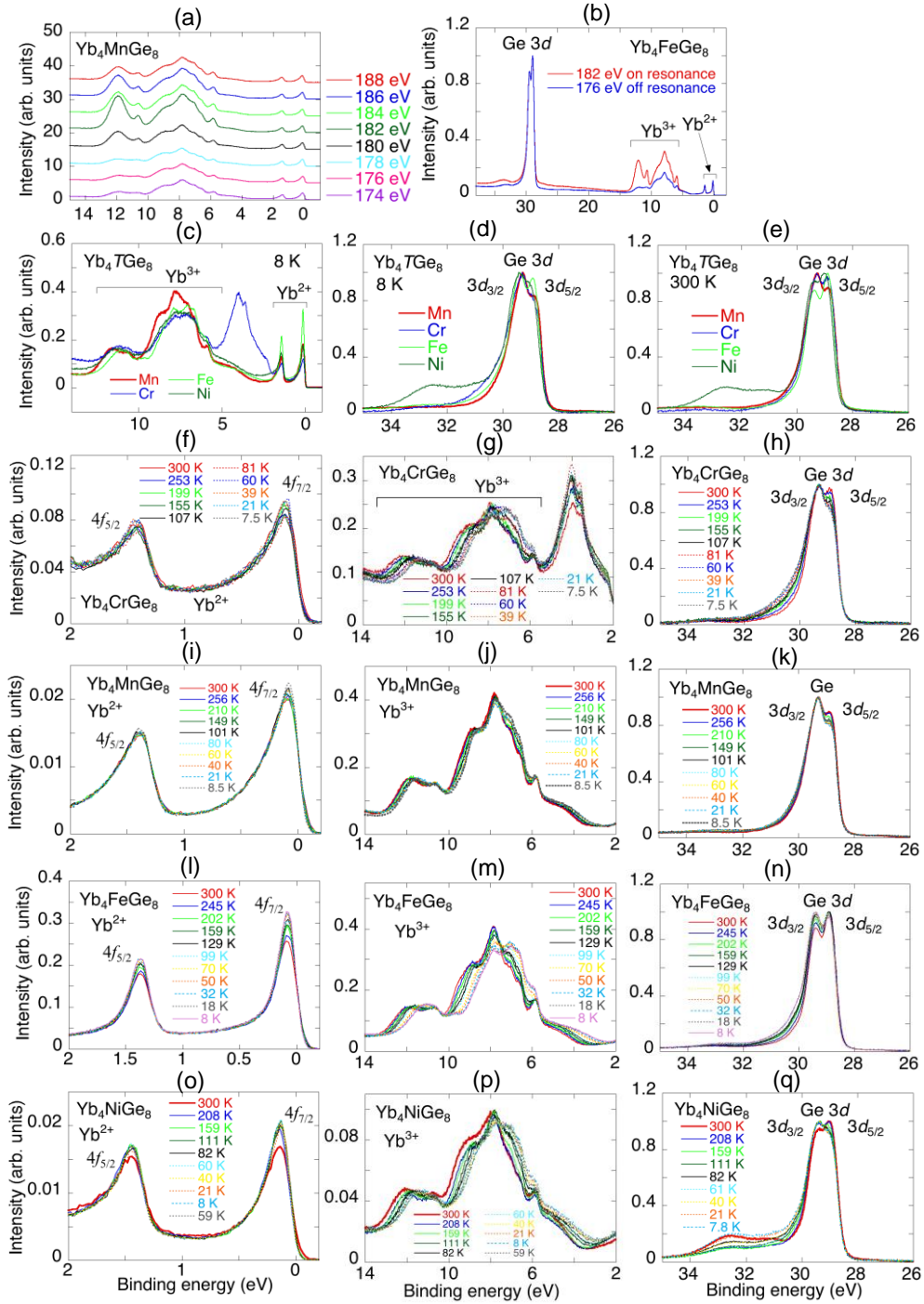
FIGURE 1. (a) Incident energy dependence of the valence band spectra of Yb$_4$MnGe$_8$ around Yb 4d-4f resonant energy at 300 K. (b) Wide band spectra of Yb$_4$FeGe$_8$ at on and off resonances at 300 K. (c) Comparison of the valence band spectra of Yb$_4$$TGe_8$ (T = Cr, Mn, Fe, Ni) at 8 K. (d), (e) Comparison of the Ge 3d core-level spectra of Yb$_4$$TGe_8$ (T= Cr, Mn, Fe, Ni) at 8 and 300 K.(f), (i), (l), (o) Temperature dependence of the valence band spectra of Yb^{2+} components of Yb$_4$$TGe_8$ near the Fermi level. (g), (j), (m), (p) Temperature dependence of the valence band spectra of Yb^{3+} components of Yb$_4$$TGe_8$. (h), (k), (n), (q) Temperature dependence of the Ge 3d core-level spectra of Yb$_4$$TGe_8$.

REFERENCES

1. S. C. Peter, M. Chondroudi, C. D. Malliakas, M. Balasubramanian, and M. G. Kanatzidis, *J. Am. Chem. Soc.* **133**, 13840 (2011).

Electronic structure of Mn₃Sn investigated by angle-resolved photoemission

Shilong Wu[a†], Masashi Arita[b], Kazuki Sumida[a‡],
Koji Miyamoto[b] Hitoshi Sato[b], and Taichi Okuda[b]

[a]Graduate School of Science, Hiroshima University, 3-1-5 Kagamiyama, Higashi-Hiroshima 739-8586, Japan
[b]Hiroshima Synchrotron Radiation Center, Hiroshima University, 2-313 Kagamiyama, Higashi-Hiroshima 739-0046, Japan

Keywords: Mn₃Sn, Weyl semimetal

Weyl semimetals are novel topological materials that host Weyl fermions. This novel quantum matter has been realized in certain inversion-symmetry breaking materials with large spin-orbit interaction such as TaAs[1] and NbAs[2] systems. In these weakly correlated systems, some proof of Weyl semimetals such as Weyl node or Fermi arc connecting Weyl points has been observed by ARPES measurement. Recently, it has been expected that a non-collinear antiferromagnet Mn₃Sn, which is a strongly correlated system, can be a Weyl semimetal caused by the time-reversal-symmetry breaking and demonstrated the evidence by magnetotransport measurement and ARPES observation[3]. However, not only because of the highly correlated system but also uncleavable crystal structure obtaining the well-ordered surface is highly difficult and the reported electronic structures observed by ARPES measurement are not clear enough to compare the data with first principles calculation precisely.

For getting the atomically flat clean surface of the uncleaved metal surfaces, the repeated ion-sputtering and annealing procedure is widely utilized so far. Recently, it has been demonstrated that the procedure also works to obtain a clean surface of some alloys such as YbB₁₂ and SmB₆ single crystals[4,5].

Here in this report, in order to obtain clearer evidence of the nature of Weyle semimetal in Mn₃Sn, we have tried to obtain the clean Mn₃Sn(0001) surface by the sputtering and annealing procedure and observe the electronic band structure by ARPES and spin-ARPES.

The Mn₃Sn single crystal sample was grown by the bridgemann method. The orientation of the sample was checked by the observation of the Laue pattern and mechanically polished with diamond paper. The polished sample was sputtered with Ar^+ ion at 550 V and post-annealed at 950 K in the ultra-high-vacuum chamber. Figure 1(a) shows the low energy electron diffraction (LEED) pattern taken at E_k=37.2 eV. The clear LEED spots and the absence of the C 1s or O 1s peak in the Auger spectrum (not shown here) indicate that the sample surface was successfully cleaned by the procedure.

Figures 2 show the results of Fermi surface mapping as well as the band mapping along K-Γ-K and K-M-K lines (red lines in the FS map) taken at hν=103 eV where the k_z value corresponds to the bulk Γ point. Hexagonal FS and observed band structures are in good agreement with the previous results reported recently[3]. Although we have measured the well ordered clean surface, the observed band structure is similar to the previous report and renormalized very much indicating that the material is a highly correlated system. Similarly to the previous study, the Fermi arc has not been observed and no clear evidence of spin polarization has been observed in our spin-ARPES measurement that was done near the kx, ky positions where the existence of Fermi arc is expected (not shown here). Since our measurement was done around 50 K, the absence of spin-polarized states might come from the possible phase transition to the cluster glass

phase with a ferromagnetic moment that appears below 50K[6]. Further investigation at a higher temperature and with a magnetized sample is expected in the near future.
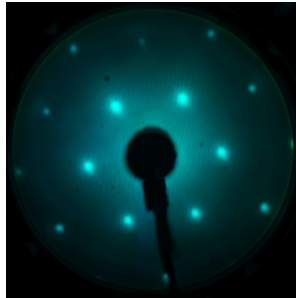

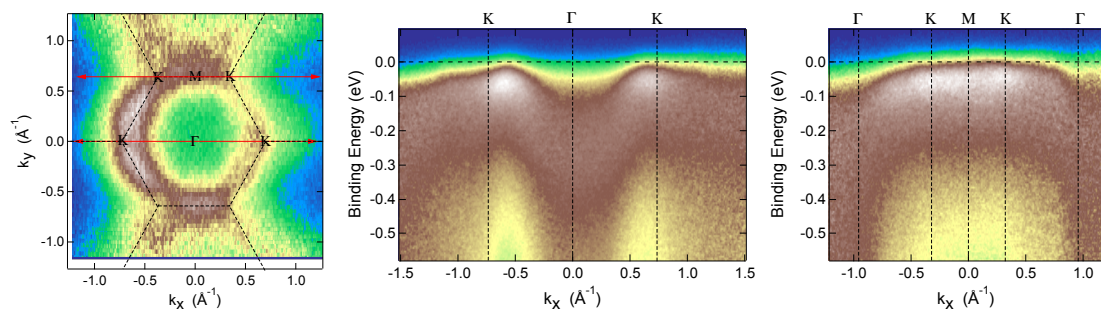**FIGURE 1.** LEED pattern of Mn$_3$Sn taken at E_k=37 eV after Ar+ sputtering and annealing.

FIGURE 2. ARPES results of Mn$_3$Sn surface taken at hv=103 eV.

REFERENCES

1. S.-Y. Xu et al., "Discovery of a Weyl fermion semimetal and topological Fermi arcs", Science 349, 613–617 (2015).

2. S.-Y. Xu et al., "Discovery of a Weyl fermion state with Fermi arcs in niobium arsenide", Nat. Phys. 11, 748-754(2015).

3. K. Kuroda et al., "Evidence for Magnetic Weyl Fermions in a Correlated Metal", Nat. Mat. 16, 1090-1096 (2017).

4. K. Hagiwara et al., "Surface Kondo Effect and Non-Trivial Metallic State of the Kondo Insulator YbB$_{12}$". Nat. Commun. 7, 12690 (2016).

5. Y. Ohtsubo, et al., "Non-trivial surface states of samarium hexaboride at the (111) surface", Nat. Commun. 10 2298-2304 (2019).

6. S. Nakatsuji, N. Kiyohara, and T. Higo, "Large anomalous Hall effect in a non-collinear antiferromagnet at room temperature", Nature 527, 212–215 (2015).

† present address: Koeln Universitat
‡ present address: Tokyo Institute of Technology

Elucidation of the electronic band of germanene superperiodic structure

Osamu Kubo[a], Seijiro Kinoshita[a], Hitoshi Sato[b] and Taichi Okuda[b]

[a]Graduate School of Engineering, Osaka University,
2-1 Yamadaoka, Suita, Osaka 565-0871, Japan
[b]HiSOR, Hiroshima University,
2-313 Kagamiyama, Higashi Hiroshima, Hiroshima 739-0046, Japan

Keywords: germanene, ARPES

Monolayer sheets of group IV materials such as Si and Ge were also predicted to have Dirac cone analogous to graphene. They are composed of buckled honeycomb structure which is predicted to introduce very curious physical properties, such as quantum-spin Hall effect and tunable band gap by external electric field [1,2]. These properties are more likely to be able to observe in germanene as compared with silicene owing to its relatively large spin-orbit coupling [2]. Currently, formation of germanene has been reported mainly on metal substrates such as Au(111), Pt(111), Al(111), and so forth. [3-5]. However, it is still controversial whether the reported germanenes have Dirac cone. Recently, we have shown that a honeycomb-like structure (germanene) of a Ge monolayer film with an $\sqrt{7}\times\sqrt{7}$ period is formed on the Al(111) surface [6]. In this structure, however, the interaction with the substrate is strong and Dirac cone as a germanene did not appear. On the other hand, the interaction with the Al(111) substrate is reported to be weak in the germanene with 3×3 periodicity reported in previous researches [4]. Thus, we have studied electronic band structure of 3×3 germanene using angle resolved photoelectron spectroscopy (ARPES).
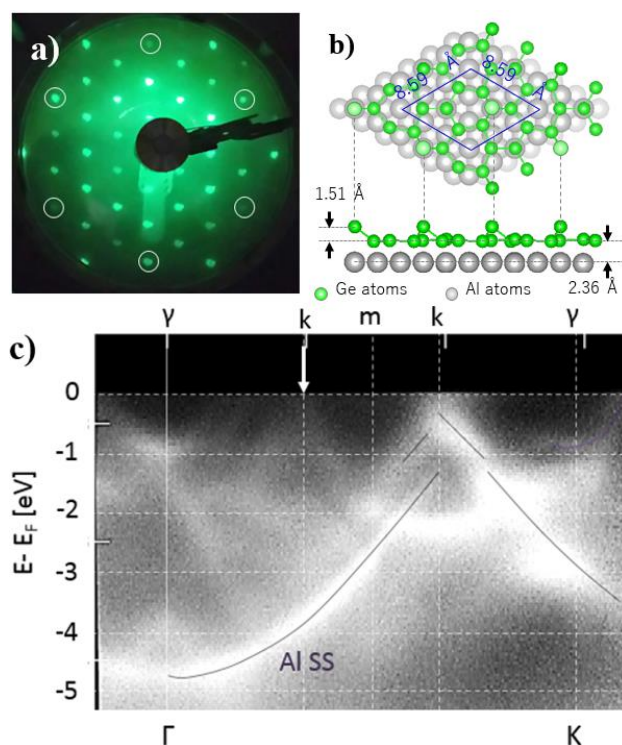

FIGURE 1. LEED image obtained from germanene on Al(111). White circles indicate 1×1 spots. (b) Schematic of Structural model of Al(111)3×3-Ge surface. (c) ARPES intensity obtained from germanene on Al(111) along Γ -K direction.

Figure 1(a) shows a LEED image for an Al(111)3×3-Ge surface, which was formed in an ultrahigh vacuum chamber by Ge deposition onto an atomically clean Al(111) surface at a substrate temperature about 100 °C with an evaporation rate of 0.03 ± 0.01 ML/min for 30 min. A proposed 3×3-Ge structural model [7] is shown in Fig. 1(b), in which the precise atomic coordinates are determined by our low energy ion scattering spectroscopy [8].

Figure 1 (c) shows the results of ARPES measurement for 3×3-Ge surface with incident light energy of 53 eV obtained along the Γ-K direction of Al (111). This direction is assigned to a Brillouin zone of Al(111)3×3 phase as the direction of γ-k-m-k-γ (described in small letters above Fig. 1(c)). In addition to the surface band of Al(111) (black line in the figure), various band dispersions not observed before Ge deposition were observed on the surface. It has been assumed that Ge honeycomb structure forms 2×2 superstructure in the Al(111) 3×3-Ge, and Dirac cone is expected to be expressed at its k point. In fact, a linear band dispersion is seen around the k point indicated by an arrow in Fig. 1(c). When the incident light energy was changed, however, the linear dispersion around k point disappeared along with the surface state of Al(111), which suggests that this band dispersion is derived from Al layer but not from surface Ge layer.

REFERENCES

1. C.-C. Liu, *et al.*, Phys. Rev. Lett. 107, 076802 (2011).
2. M. Ezawa, New J. Phys. 14, 033003 (2012).
3. M. E. Dávila, *et al.*, New J. Phys. 16, 095002 (2014).
4. M. Derivaz, *et al.*, Nano Lett. 15, 2510 (2015).
5. L. Li, *et al.*, Adv. Mater. 26, 8420 (2014).
6. S. Endo, *et al.*, Appl. Phys. Express 11, 015502 (2018).
7. Y. Fukaya, *et al.*, 2D Mater. 3, 035019 (2016).
8. O. Kubo, *et al.*, unpublished.

Photoemission spectroscopy study for half-metal Heusler compounds

K. Goto[a, b], Y. Sakuraba[b], H. Sato[c] and K. Hono[a, b]

[a]Graduate school of Pure and Applied Science, University of Tsukuba, 1-1-1 Tennodai Tsukuba 305-0047, Japan
[b]National Institute for Materials Science, 1-2-1 Sengen, Tsukuba 305-0047, Japan
[c]Hiroshima Synchrotron Radiation Center, Hiroshima University, 2-313 Kagamiyama, Higashi-hiroshima 739-0046, Japan

Keywords: Half-metal Heusler compounds, ARPES, Photon energy scan

Co-based Heusler compounds such as Co_2MnSi and $Co_2FeGa_{0.5}Ge_{0.5}$ (CFGG) are predicted to have high spin-polarization of the conduction electron at the Fermi level. These materials have been attracting much attention for spintronics devices of tunneling magnetoresistance (TMR) and current perpendicular to plane giant magnetoresistive (CPP-GMR) devices [1-4]. However, observed large reduction of MR ratio with temperature [1, 4] limits a potential of applications using half-metallic Heusler compounds. To understand a cause of this problem, the spin-polarized electronic structure of bulk, surface and interface and its temperature dependence should be observed by spin and angle-resolved photoemission spectroscopy (SARPES) which is the most powerful method for direct measurement of the electronic structure (energy, moment and spin) in the solids. However, CFGG has 3-dimensional Brillouin Zone (BZ) and it is not clear that which photon energy is suitable for observation of the specific band structure. First, a photon energy scan using synchrotron radiation for CFGG should be performed to understand which photon energy is optimal for specific k_z point in the BZ.

In this study, the CFGG thin film sample which has $L2_1$ structure was prepared by the magnetron sputtering method equipped at National Institute for Materials Science (NIMS) and it was delivered to Hiroshima Synchrotron Radiation Center (HiSOR) with keeping high vacuum (~3.0×10^{-10} mbar) level by the suitcase chamber. The surface quality was confirmed by low-energy electron diffraction (LEED). The ARPES measurement was carried out at BL-7 of the HiSOR. The sample was kept at about 8.0 K during the experiment. A photon energy scan was performed, ranging photon energy $h\nu$ from 27-107 eV and the Fermi surface was observed.

Figure 1 shows the Fermi surface of CFGG along k_z direction obtained by a photon energy scan. In the free-electron final-state approximation, the conversion for the perpendicular momentum k_z given by $k_z = \sqrt{2m[(h\nu - \phi - E_B)\cos^2\theta + V_0]}/\hbar$, where θ is the emission angle of the electron, ϕ is the work function and V_0 is the inner potential. In the conversion of experimental data to Fermi surface, $V_0 = 9$ eV was used tentatively. However, the distinctive structure around high symmetry points for comparison with the calculation to determine the proper value of the inner potential cannot be obtained in experimental Fermi surface. The cause of this problem is considered that the sample surface was not clean because of oxygen

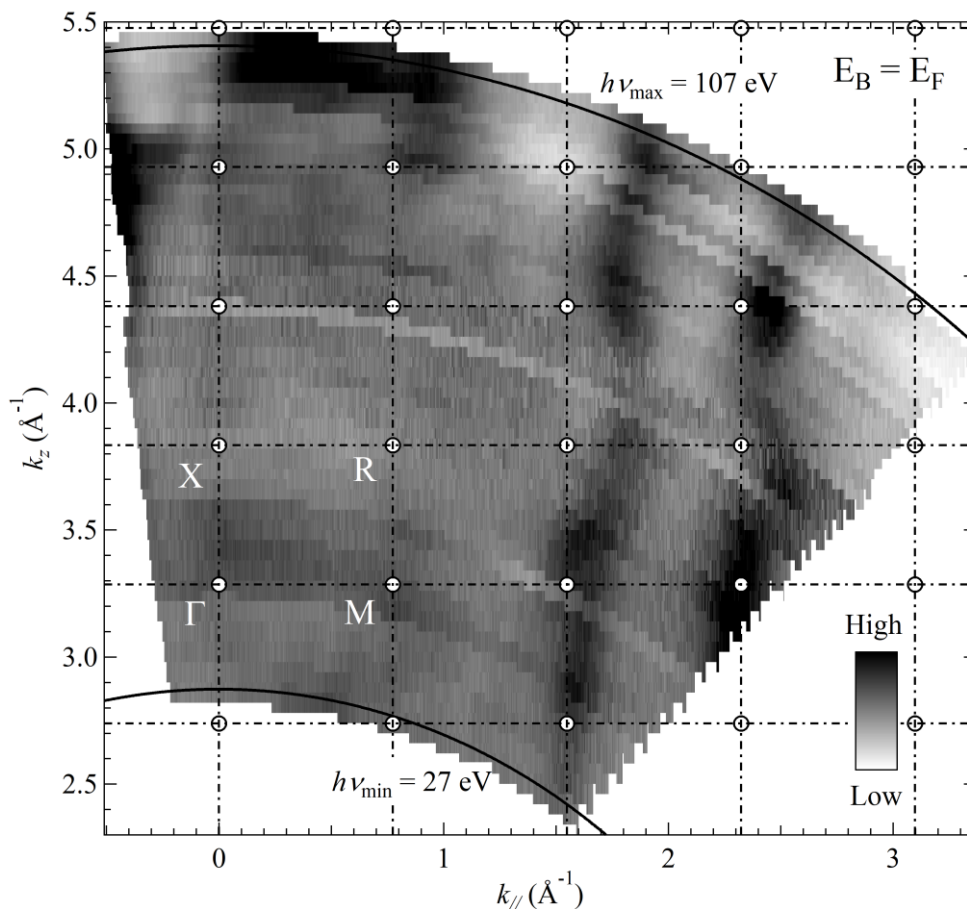and carbon. The surface cleaning should be performed by short annealing before ARPES measurement.

FIGURE 1. Measured Fermi surface of CFGG along k_z direction. A photon energy scan was performed, ranging from 27 – 107 eV. Converting the photon energy into k_z with the inner potential V_0 of 9 eV.

In summary, the photon energy scan was performed for half-metal Heusler compound CFGG thin film and Fermi surface along k_z direction was obtained to determine the proper value of the inner potential V_0. However, the symmetric structure around high symmetry points cannot be observed because of the impurity on the sample surface. The short annealing should be performed for Heusler thin film samples to clean the surface before ARPES measurement.

REFERENCES

1. Y. Sakuraba *et al*., Appl.Phys. Lett. **88**, 192508 (2006)
2. T. Ishikawa *et al*., J. Appl. Phys. **103**, 07A919 (2008)
3. S. Li *et al*., Appl. Phys. Lett. **103**, 042405 (2013)
4. J. W. Jung *et al*., Appl. Phys. Lett. **108**, 102408 (2016)

Photoelectron Spectroscopy of Thin-film Beta Tungsten

H.T. Lee[a], H. Yamaoka[b], A. Nagakubo[a] and H. Sato[c]

[a]*Graduate School of Engineering, Osaka University, Suita 565-0871, Japan*
[b]*RIKEN SPring-8 Center, Hyogo 679-5148, Japan*
[c]*Hiroshima Synchrotron Radiation Center, Hiroshima University, Higashi-Hiroshima 739-0046, Japan*

Keywords: Electronic structure, Photoelectron spectroscopy, Spintronic devices, Tungsten

Thin film β-tungsten (β-W) is attracting extensive attention due to its giant spin Hall effect and promising application in spintronics as memory devices. Large spin currents have been used to set the magnetization of adjacent magnetic layers using the spin torque effect [1]. The transfer efficiency of the charge-to-spin current is defined by the spin-Hall angle which is ~0.3 for β-W [2] in comparison to <0.07 for α-W at 300 K. Utilization of the large spin-Hall angle of β-W appears promising for applications in spin torque devices. However, the reason for the large magnitude of the spin Hall angle in β-W is presently not known. Clarifying whether the giant spin Hall effect arises from extrinsic or intrinsic properties is the first step towards engineering β-W based spin torque devices. Extrinsic effects arise from spin-dependent scattering with impurities or band structure peculiarities. Many studies have examined the magnitude of the spin Hall angle as a function of W structure, but to date, hardly any experimental measurements of the electronic states of β-W have been reported. It is especially important to characterize the band structure near the Fermi level as the large spin Hall angles reported are experiments performed at very low currents.

In this work, the experimental goal was to characterize the electron density of states of deposited β-W films by measuring high-resolution valence band spectra near the Fermi level and compare to reference α-W. Thin (~50 nm) α-W and β-W films on silicon substrates were produced using physical vapor deposition technique. The mechanical and structural properties were characterized using a combination of X-ray diffraction and picosecond ultrasonic measurements [3]. The elastic constants of pure α-W and β-W were 5–10% lower than the reported bulk values for α-W. The calculated elastic constants using density functional theory agreed within 10% of the experimental values.

In 2017, photoelectron spectroscopy (PES) measurements of thin α-W and β-W films were performed. Figure 1 (a) shows the results for α-W as a function of in-vacuo Ar sputtering time. The tungsten oxide layer formed due to air transport was removed following ~25 minutes of Ar sputtering (1 keV) as determined from the W 4f core level spectra. Figure 1(b) compares the photoelectron spectrum between α-W and β-W samples. Fine difference in the structure between -2 and -4 eV was observed. Specifically, α-W clearly showed a double peak structure, which was less prominent in β-W. However, such comparisons in peak shape and magnitudes were complicated by the fact that there was an additional broad peak observed between -4 and -6 eV in experiments. This signal continuously decreased with increasing sputtering time as illustrated in both Figures 1(a) and (b) - suggesting partial contribution from surface oxygen contamination.

In 2018, PES measurements on 99.999% pure bulk-W sample was performed to clarify whether the oxygen signals arose due to intrinsic oxygen impurities in deposited thin films or from surface contamination during sputtering in the preparation chamber. Figure 2 (a) shows the results for bulk α-W as a function of in-vacuo Ar sputtering time. Comparing the spectrum between 5- and 25-minutes sputtering, it is clear that the contamination decreased then increased. This suggests that the Ar sputtering process is a source of contamination, either indirectly by recoil implantation of surface impurities or direct implantation from the Ar ion source itself. While the contamination is reduced following longer sputtering time, it is nevertheless never reduced to zero. Figure 2 (b) compares the photoelectron spectrum between bulk and thin film α-W samples. Qualitatively, the width and energy of the contamination peak in the region between -4 and -6 eV are in good agreement, although the

absolute magnitudes differ due to differences in sputtering time. The fact that there is qualitatively very little difference in the spectrum between a 99.999% pure bulk-W and a much less pure thin film supports the notion that the impurities are being introduced by the Ar sputtering process itself. While this is a disappointing result, it should be remembered that β-W thin films are almost exclusively produced using physical vapor deposition methods with unknown control of oxygen impurities. Since large spin Hall angles reported in other thin film materials generally arise due to spin-orbit interaction of impurities [4], or resonant/surface skew scattering effects with impurity sites [5], our results indicate that the role of oxygen impurities on β-W surfaces should be clarified in the reported large spin Hall angles of β-W layered systems.
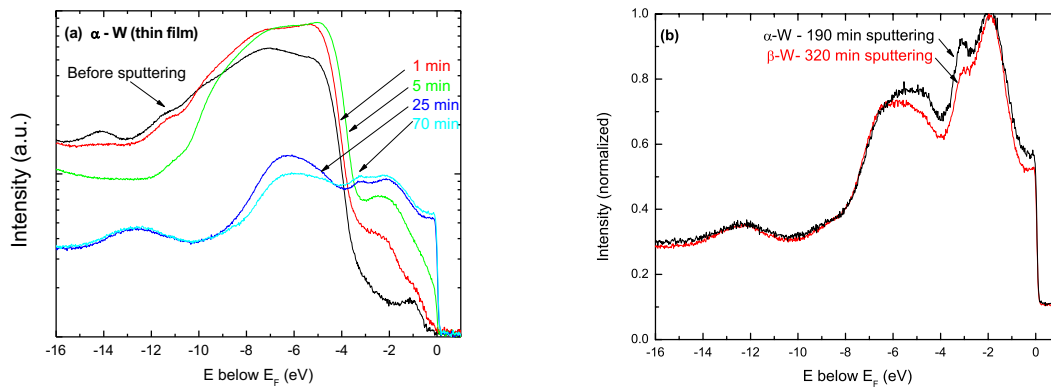
FIGURE 1. Photoemission spectra for (a) thin film α-W sample as function of Ar sputtering time, and (b) comparison of α-W and β-W samples showing the difference in peak structure between -2 and -4 eV.
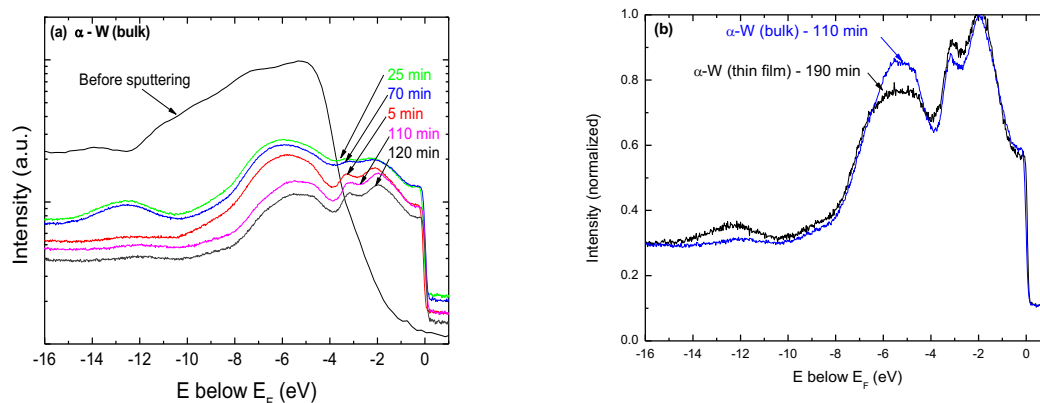

FIGURE 2. Photoemission spectra for (a) 99.999% pure bulk α-W sample as function of Ar sputtering time, and (b) comparison of bulk and thin film α-W samples showing qualitatively similar peak structure between -4 and -6 eV.

REFERENCES

1. L. Liu et al., Science **336**, 555 (2012).
2. C-F. Pai et al., Appl. Phys. Lett. **101**, 122404 (2012).
3. A. Nagakubo et al., "Elastic constant of alpha and beta tungsten films studied by picosecond ultrasonics" USE2017
4. N. Nagaosa et al., Rev. Mod. Phys. **82**, 1539 (2010).
5. G-Y Guo et al., Phys. Rev. Lett., **102**, 036401 (2009).

Angle resolved photoemission study of $Sm_{1-x}Yb_xB_6$

M. Arita[1], H. Sato[1], K. Shimada[1], H. Namatame[1], M. Taniguchi[1], H. Tanida[2], Y. Osanai[3], K. Hayashi[3], F. Iga[4]

[1]*Hiroshima Synchrotron Radiation Center,* [2]*Graduate School of Advanced Sciences of Matter,*

Hiroshima University, Kagamiyama, Higashi-Hiroshima 739-0046, Japan

[3]*Graduate School of Science and Engineering,* [4]*College of Science, Ibaraki University, Mito, Ibaraki, 310-8512, Japan*

SmB_6 is well known as Kondo insulator, the energy gap of which opens below ~100 K. Recently, it has attracted great interest as candidate material of topological Kondo insulator [1]. The spin-polarized surface band structure near E_F has been observed by spin resolved ARPES for SmB_6 (001) [2] .

Although YbB_6 is one of candidate for topological Kondo insulators, c-f hybridized gap has not been found [3]. It is controversial whether there is the topological surface state or not.

To clarify the impurity effects for the energy gap and the surface states in SmB_6 and YbB_6 near E_F, we have measured the electronic band structures of $Sm_{1-x}Yb_xB_6$ (x=0, 0.1 and 0.8) by means of ARPES.

Figure 1 shows the ARPES image for x = 0.1 around $\bar{\Gamma}$ with $h\nu$ = 26 eV at 8 K. The localized bands stem from Sm^{2+} 4f bands at E ~ - 20 and − 160 meV. The bands crossing the 4f bands are derived from rare-earth 5d bands, which are hybridized with the 4f bands strongly. Between E_F and - 20 meV, the bands exist and cross E_F at $k \sim \pm 0.35$ Å^{-1}, similar to that in SmB_6 [2]. There is no change in the band structure with the substitution from Sm to Yb in x ≤ 0.1. Thus, they are attributed to the topological surface states as in SmB_6, and robust for the impunity of Yb ion.

Figure 2 shows the ARPES image for x = 0.8 along $\bar{\Gamma} - \bar{X}$ line with $h\nu$ = 26 eV at 8 K. Though the whole band structure is similar to that for YbB_6, the weak non-dispersive bands derived from Sm^{2+} 4f are observed at E ~ - 20 and - 160 meV same as in SmB_6. The 5d derived bands cross E_F at $k_F \sim \pm 0.25$ and 3.8 Å^{-1}, respectively. However the bands are not hybridized with Sm 4f bands clearly. Moreover, the surface band and energy gap are not observed for SmB_6 and $Sm_{0.9}Yb_{0.1}B_6$ near E_F. Thus, c-f hybridization gap and the surface topological bands are not found for $Sm_{0.9}Yb_{0.1}B_6$.

Fig.1 ARPES image of $Sm_{0.9}Yb_{0.1}B_6$.
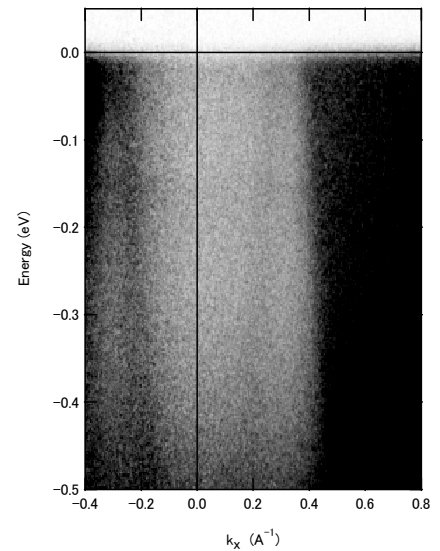
Fig.2 ARPES image of $Sm_{0.2}Yb_{0.8}B_6$.

1)   T. Takimoto et al., J. Phys. Soc. Jpn. 80 123710 (2011).

2)   N. Xu et al., Nat Commun 5 (2014).
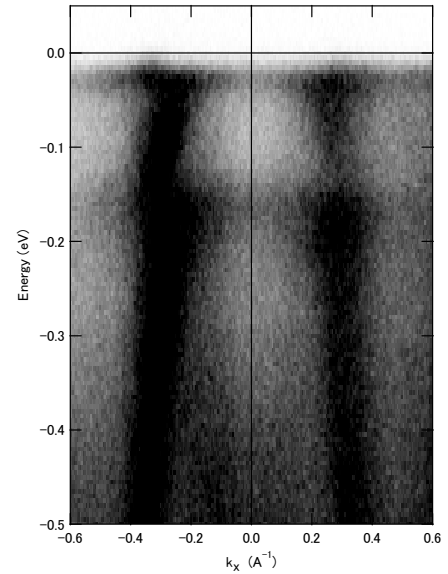
3)   J. Jiang et al., Nat. Commun, 4, 3010(2013)

Linear polarization dependence of angle resolved photoemission study on SmB$_6$

M. Arita[1], H. Sato[1], K. Shimada[1], H. Namatame[1], M. Taniguchi[1], H. Tanida[2], Y. Osanai[3], K. Hayashi[3], F. Iga[4]

[1]*Hiroshima Synchrotron Radiation Center, [2]Graduate School of Advanced Sciences of Matter,*

Hiroshima University, Kagamiyama, Higashi-Hiroshima 739-0046, Japan

[3]*Graduate School of Science and Engineering, [4]College of Science, Ibaraki University, Mito, Ibaraki, 310-8512, Japan*

Rare-earth hexaboride forms CaB$_6$-type cubic crystal structure. The unusual physical properties appear originated from localized 4f bands. SmB$_6$ is well known as Kondo insulator, the energy gap of which opens below ~100 K. Recently, it has attracted great interest as a candidate material of topological Kondo insulator [1]. The spin-polarized surface band structure near the Fermi level (E$_F$) around $\overline{\mathrm{X}}$ has been observed by spin resolved ARPES for SmB$_6$ (001) [2]. On the other hand, the existence of the topological surface state around $\overline{\Gamma}$ is controversial, because the band structures observed by ARPES are obscure.

In order to clarify the topological surface states in SmB$_6$ around $\overline{\Gamma}$, we have measured the electronic band structures of SmB$_6$ by means of ARPES with the linear polarized lights parallel and perpendicular to the mirror plane, that is, P and S polarized lights.

Figures 1 (a) and (b) show the Fermi surfaces (FS's) for $h\nu$ = 26 eV at 8 K with P and S polarized lights, respectively. The elliptical FS's centered at $\overline{\mathrm{X}}$ point are derived from the topological surface state in the bulk c-f hybridization gap. Around $\overline{\Gamma}$, two circular FS's are observed with S polarized light in first BZ and with P polarized light in second BZ. Figure 2 shows the ARPES E-k image for S polarized light along $\overline{\Gamma}$ - $\overline{\mathrm{X}}$ in first BZ at 8 K. The localized bands at E ~ - 20 meV stem from Sm 4f bands. Between E$_F$ and 4f band, there are two metallic bands which cross E$_F$ at k ~±0.1 and ~ ±0.3 Å^{-1}. Though the metallic state remains below 300 K in inner band, the structure crossing E$_F$ in outer band disappears above 60 K. The temperature corresponds approximately to the temperature of the bulk c-f gap opening. It is considered that the inner band stems from the bottom of the bulk conduction state and the outer band is derived from the topological surface state, which forms the circular FS centered at $\overline{\Gamma}$ below 60 K.
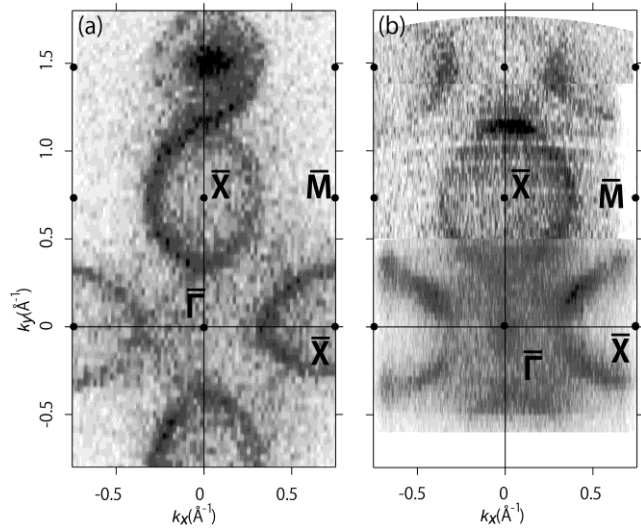

Fig.1 Fermi surfaces of SmB$_6$ measured with (a) P and (b) S polarized lights.
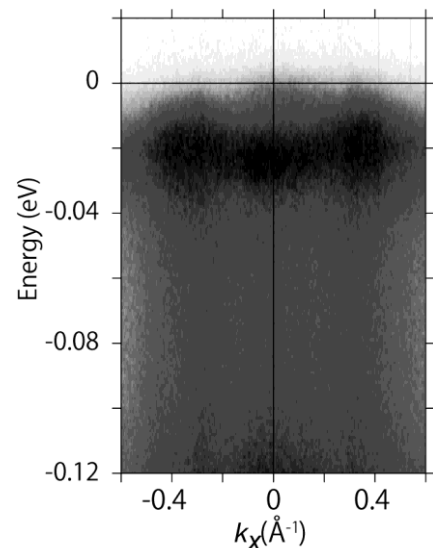
Fig.2_ARPES image of SmB$_6$ along $\overline{\Gamma}$ - $\overline{\mathrm{X}}$ with S polarized light.

1)   T. Takimoto et al., J. Phys. Soc. Jpn. 80, 123710 (2011).

2)   N. Xu et al., Nat. Commun. 5, 4566 (2014).

Probing bulk k_z dispersion of a correlated semimetal CeSb by low $h\nu$ ARPES

Kenta Kuroda[a], Shuntaro Akebi[a], Ryo Noguchi[a], So Kunisada[a], Masashi Arita[b],
Hideaki Kitazawa[c], Shik Shin[a], Hiroyuki Suzuki[a], Takeshi Kondo[a]

[a]*The Institute for Solid State Physics (ISSP), The University of Tokyo, Kashiwa, Chiba 277-8581, Japan*
[c]*Hiroshima Synchrotron Radiation Center, Hiroshima University, Higashi-Hiroshima, 739-0046, Japan*
[c]*National Institute for Materials Science (NIMS), 1-2-1 Sengen, Tsukuba 305-0047, Japan*

Keywords: Strong correlation, *c-f* mixing, magnetic transition

CeSb is a correlated semimetal with a rocksalt lattice, where its Ce^{3+} ions provoke Kondo transport [1] and at low temperature coordinate fourteen magnetostructures in the phase diagram [2, 3]. Even at zero-field, the seven phases with various long-period magnetostructures appear one after another below the Néel temperature (T_N) ~17 K. The magnetic ground state appears below ~8.5 K, as antiferromagnetic (AF) phase with the double-layer stacking of the Ising-like ferromagnetic (001) planes. Various antiferro-paramagnetic (AFP) phases initially establish below the T_N, where the double-layer modulation is periodically locked by the paramagnetic (P) layers. This variety in the magnetic modulation is understood as "devil's staircase" behavior [4] that can be phenomenologically explained by presence of competing different magnetic interactions.

Microscopically, the key mechanism for the above anomalies is for long time considered to be a strong hybridization between the localized Ce 4*f* moment and the itinerant carriers (*c-f* mixing). However, despite 40 years of intense researches, the low energy electronic structure corresponding to the devil's staircase has been so far elusive. Therefore, direct observations of the quasiparticle structure by angle-resolved photoemission spectroscopy (ARPES) across the T_N is strongly required, because it has been widely applied for the strongly correlated systems and substantiated the impact of the *c-f* mixing on their quasiparticle structures. Previous ARPES measurements on CeSb with surface-sensitive photon energy ($h\nu$) have mapped the electronic structures in ordered phase, and suggested the imapact of the *c-f* mixing. However, a critical issue was recently made for its surface sensitivity of ARPES measurements to investigate "intrinsic" bulk structures of CeSb [5]: either k_z broadening effect [6] in the surface-sensitive ARPES or possible surface resonant states can hinder the bulk responses.

In this study, we have performed relatively bulk-sensitive ARPES measurement by low-energy photons from synchrotron at HiSOR BL9A to access the intrinsic bulk structures of CeSb. Figure 1(a) summarizes the ARPES images at 30 K above T_N acquired with various $h\nu$ ranging from 6.4 to 7.4 eV. For $h\nu$=6.4 eV, we observe, in the paramagnetic phase, the two-hole bands originating from the Sb 5*p* state [5]. With increasing $h\nu$, our data clearly shows that the top of the hole bands shift downward in energy. This behavior becomes more clearly visible in Fig. 1(b) where the energy distribution curves (EDCs) at $k_\parallel$=0 are presented. All of these data provide a signature for the k_z dispersion, demonstrating that the bulk-sensitive ARPES with low $h\nu$, in sharp contrast to the surface-sensitive ARPES, enables us to detect the intrinsic bulk states. More experiments with low $h\nu$ ARPES particularly at low temperature below T_N and with high energy resolution is necessary to experimentally investigate the microscopic mechanism of the devil's staircase.
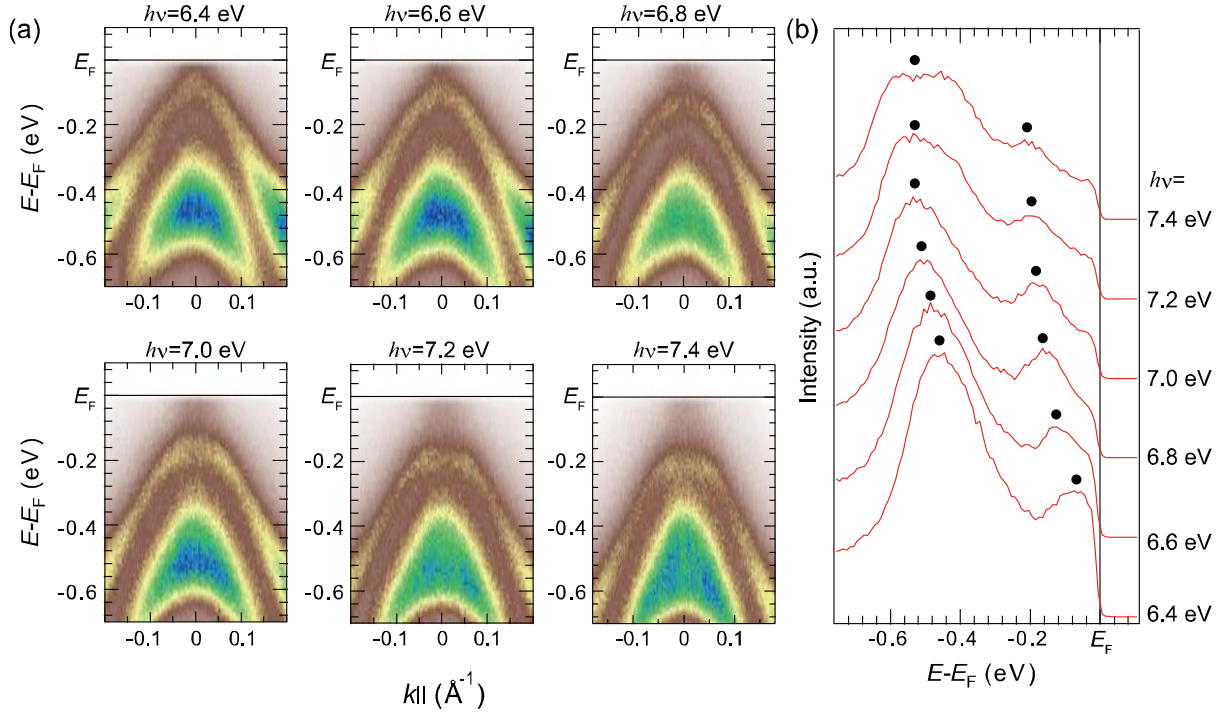
FIGURE 1. (a) ARPES images of electronic structures at paramagnetic state by using various photon energies from 6.4 eV to 7.4 eV. (b) Their energy distribution curves (EDCs) at $k_{\parallel}=0$. The clear k_z dispersions of the hole bands are traced by the circles.

REFERENCES

1. T. Kasuya, Y. Haga, Y. Kwon, and T. Suzuki, Physics in low carrier strong correlation systems. Physica B: Con-densed Matter **186**, 9 (1993).
2. J. Rossat-Mignod *et al*., Phase diagram and magnetic structures of CeSb. Phys. Rev. B **16**, 440 (1977).
3. P. Fischer, G. Meier, B. Lebech, B. D. Rainford, and O. Vogt, Magnetic phase transitions of CeSb. I. zero applied magnetic field. Journal of Physics C: Solid State Physics **11**, 345 (1978).
4. J. von Boehm, and P. Bak, Devil's stairs and the commensurate-commensurate transitions in CeSb. Phys. Rev. Lett. **42**, 122 (1979).
5. K. Kuroda *et al*., "Experimental Determination of the Topological Phase Diagram in Cerium Monopnictides", Phys. Rev. Lett. **120**, 086402 (2018).
6. V. Strocov, J. Electron Spectrsc. Phenom. **130**, 65 (2003).

Semiconductor To Metal Transition And Spin-orbit Coupling In Boron Doped Graphene Nanoribbons

Alexander Grüneis, Boris Senkovskiy

Physics Institute II, Zülpicher Strasse 77, Köln, Germany

Keywords: ARPES, graphene nanoribbons, on-surface polymerization

In our works at BL9A and BL9B we have investigated the electronic band structure of in-situ grown N=7 and N=14 armchair graphene nanoribbons (AGNRs). Samples were made by the following procedure. We have cleaned a Au788 crystal by repeated sputtering and annealing and evaporated the organic precursor material onto the clean Au788 surface. Following the annealing of the sample with precursor molecules, we observed the fusing to an N=7 AGNRs with the well-known band structure [1].

Interestingly, we found that further annealing of the sample resulted in a new band structure that agrees well with N=14 AGNRs. This finding is not totally unexpected since the are reports of the lateral fusion of two N=7 GNRs to a N=14 GNR. However, to date there is no ARPES information. The ARPES that we measured is shown in the Figure 1. These data have been measured at BL9A. It shows that the N=14 valence band is reaching the Fermi level and that these GNRs are expect to conduct electricity much better as the wide gap N=7 GNRs. It is thus clear that the metallicity of the GNR sample can be increased by the conversion of N=7 to N=17 AGNRs.

In the time following the beamtime at HiSOR we have performed many more epxeriments (UHV Raman, Li doping and UHV transport) that proof unambigously the arge area formation of N=14 AGNRs and a manuscript is currently in preparation [2].
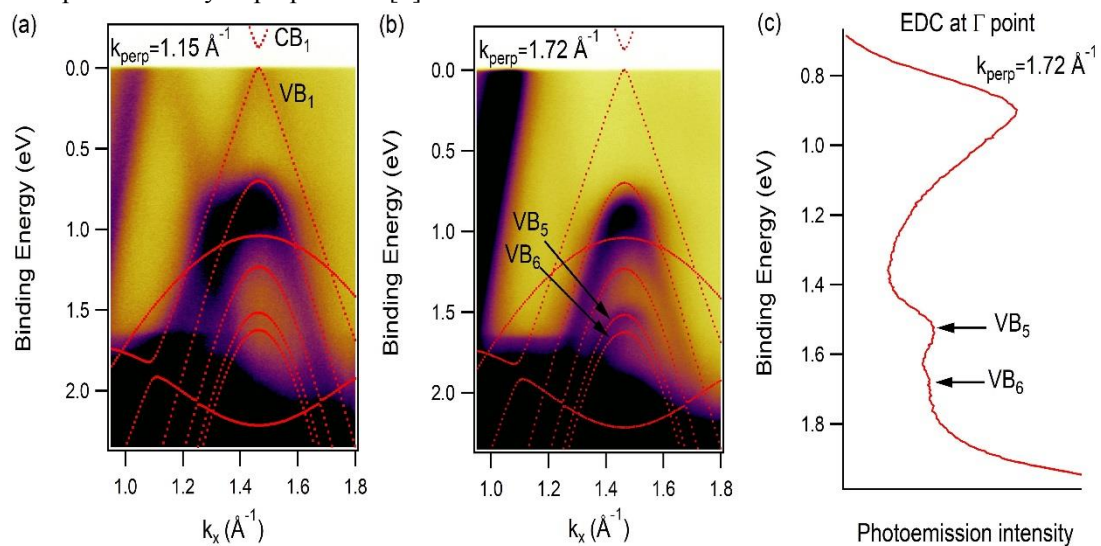

FIGURE 1. (a) and (b) ARPES spectra taken at BL9A (T= 9 K , E = 25 eV) of in-situ synthesized N=14 armchair graphene nanoribbons overlaid to a calculation. (a) and (b) are taken at different perpendicular wavevector that can selectively enhance the intensity of the linear band (labelled by VB1). (c) depicts a energy distribution curve (EDC) at the Gamma point. The nanoribbon related bands VB5 and VB6 are indicated.

REFERENCES
1. Boris V Senkovskiy *et al* 2018 *2D Mater.* **5** 035007.
2. Boris V Senkovskiy *et al* in preparation.

High-resolution ARPES Study of $Ca_3Ru_2O_7$

D. Ootsuki [a], A. Hishikawa [a], Y. Takasuka [a], D. Shibata [a], Y. Shinya [a],
N. Kikugawa [b], M. Arita [c], H. Tamatame [c], M. Taniguchi [c], and T. Yoshida [a]

[a] *Graduate School of Human and Environmental Studies, Kyoto University, Sakyo-ku, Kyoto 606-8501, Japan,*
[b] *National Institute for Materials Science, Tsukuba, Ibaraki 305-0003, Japan,*
[c] *Hiroshima Synchrotron Radiation Center, Hiroshima University, Higashi-Hiroshima, 739-0046, Japan.*

Perovskite-type ruthenium oxides has rich physics such as spin-triplet superconductivity, orbital ordering, antiferro/ferromagnetism, and metal to insulator transition with structural phase transition. Among them, $Ca_3Ru_2O_7$ is a quasi-2-dimensional semimetal showing an antiferromagnetic transition at $T_N = 56$ K and a structural phase transition at $T_s = 48$ K [1-3]. Previous ARPES study revealed the presence of the tiny Fermi surfaces at M and M' points and the momentum-dependent gap at the low temperature phase [4]. However, the Fermi surface at the high temperature phase is not determined by the ARPES measurement.

In this work, we have performed high-resolution angle-resolved photoemission spectroscopy (ARPES) measurements in order to reveal the origin of the antiferromagnetic transition and the structural transition of $Ca_3Ru_2O_7$. The ARPES spectra are were taken at BL-9A of Hiroshima synchrotron radiation center (HiSOR). The total energy resolution was ~10 meV for the incident photon energy $h\nu = 21$ eV. The sample surface of Ca_3RuO_7 was obtained by cleavage in ultrahigh vacuum of ~1.4×10^{-9} Pa . The Fermi level was calibrated by using the Fermi edge of the gold reference samples.

Figure 1 shows the temperature dependence of the Fermi surface for $Ca_3Ru_2O_7$. At the low temperature phase, the large square contour with rounded corners connecting the M points and the more intense square composed of four broad triangular feature are observed, which is in good agreement of the previous ARPES study by Baumberger *et al* [4]. On the other hand, the large square contour disappears as well as the intense inner square contour in the high temperature phase. The band dispersions along the Γ-X line are displayed in Fig. 2. The broad hole-like band around Γ-point is observed at the high temperature phase (Fig. 2 (b)). In going from the high temperature phase to the low temperature phase, the "M"-shaped band dispersion appears around Γ-point (Fig. 2 (a)), corresponding to the intense inner square contour as shown in Fig. 1 (a). These observations suggest the band folding due to the structural and/or antiferromagnetic transitions.
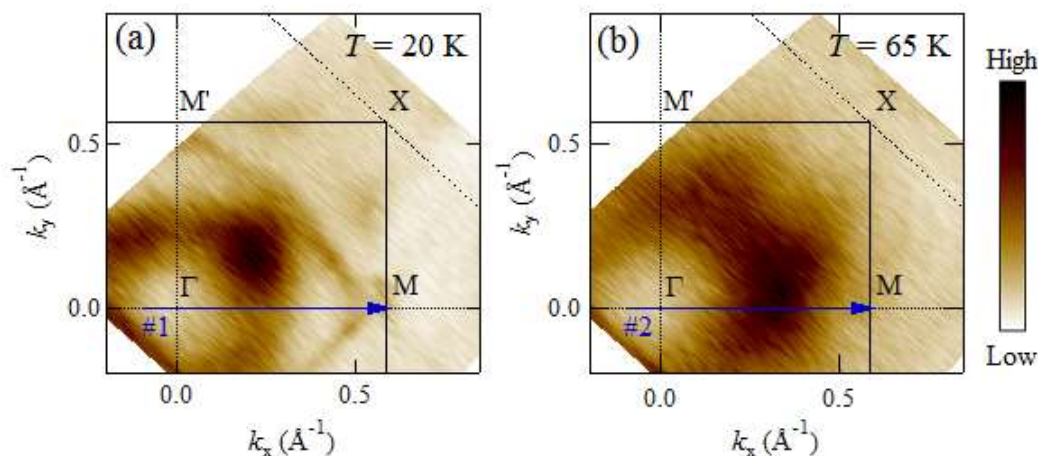

FIGURE 1. Fermi surface maps of $Ca_3Ru_2O_7$ measured at (a) $T = 20$ K and (b) $T = 65$ K, respectively. The data were acquired using $h\nu = 21$ eV with circular polarization. The ARPES spectra were integrated within ± 10 meV.
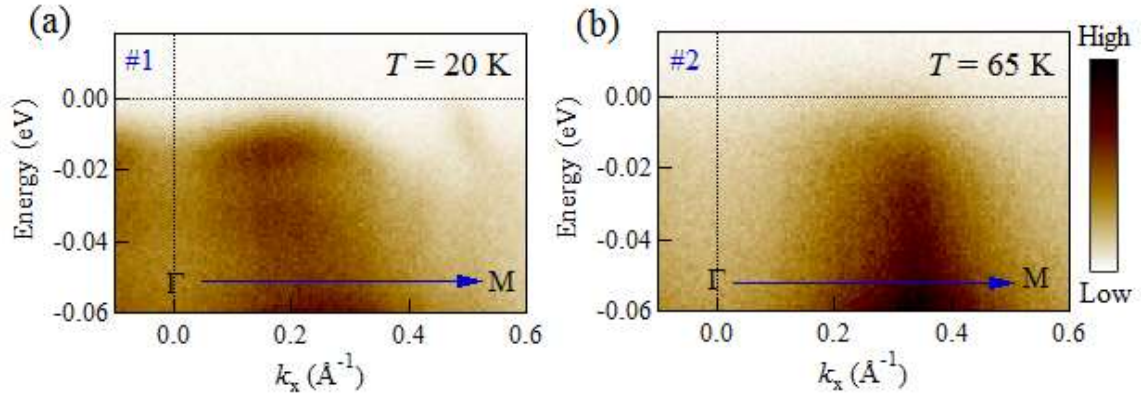
FIGURE 2. Band dispersions of $Ca_3Ru_2O_7$ taken at (a) $T = 20$ K and (b) $T = 65$ K taken at $h\nu = 21$ eV with circular polarization. The data are corresponding to the cut #1 and #2 in Figs. 1 (a) and (b), respectively.

REFERENCES

1. G. Gao *et al.* Phys. Rev. Lett. **78**, 1751 (1997).
2. Y. Yoshida *et al.* Phys. Rev. B **69**, 220411 (R) (2004).
3. N. Kikugawa *et al.* J. Phys. Soc. Jpn. **79**, 0244704 (2007).
4. F. Baumberger *et al.* Phys. Rev. Lett. **96**, 107601 (2006).

ARPES Study on the New candidate Weyl semimetal in XSi (X=Co,Rh)

Cong Li[1] , Jianwei Huang[1], Desehng Wu[1], Wei Wu[1], Guodong Liu[1], Jianlin Luo[1], K. Shimada[2] and Xingjiang Zhou[1]

[1]National Laboratory for Superconductivity, Beijing National Laboratory for Condensed Matter Physics, Institute of Physics, Chinese Academy of Sciences, Beijing 100190, China
[2]Hiroshima Synchrotron Radiation Center, Hiroshima University, 2-313 Kagamiyama, Higashi-Hiroshima, Hiroshima 739-0046, Japan

Keywords: Weyl semimetal, $RhSi_4$, ARPES

The Weyl semimetal is now a very hot topic in condensed matter physics field. So far, Dirac Fermions and Weyl Fermions have been discovered experimentally. A brand-new kind of double Weyl Fermions with Chirality have been predicted in 2017 by Shoucheng Zhang's group in Stanford[1], Zahid Hasan's group in Princeton[2], and one group in Institute of Physics, Beijing[3]. But so far, no experimental confirmation has been made yet mainly because of the lack of high quality samples. In order to study the electronic structure of the new candidate Weyl semimetal, we need use different photon energy to study this material.

Figure 1 shows the Crystal structure and electronic properties of CoSi family. CoSi is belong cubic crystal system with No.198 space group, the crystal structure as shown in Fig. 1a. The corresponding BZ is shown in Fig. 2b. The projected BZ of the (001) surface is marked in red lines. The band structure of Co(Rh)Si along the high symmetry line without spin orbital coupling as shown in Fig. 1c. It exists spin-1 excitations at Gamma point and double Weyl Fermions (WF) at R point. The 3D Fermi surface of Co(Rh)Si at calculated Fermi level is show in Fig. 1c. Because of nontrivial topology possessed by hole and electron pockets in the bulk, the Fermi arc surface states can be observed on the side surface. The electronic spectra for the (001) surface is shown in Fig. 1d. We can see that topological surface states (marked by SS) emerge from projections of spin-1 excitation and a double Weyl fermion at Γ and R points, which are stable in a large energy window. The Fermi surface of Co(Rh)Si at Fermi level are shown in Fig. 1e. Fig. 1f shows the Laue spot of RhSi sample. The clear Laue spot indicated the high quality single crystal of RhSi.

Figure 2 shows the band structure of RhSi. In order to confirm the material is on the light path, we measured the large energy range photoemission spectra (EDC) with 150 eV photon energy. Two peak can be clearly observed on the inset of Fig. 2a, one is corresponding to the 99.8 eV and another corresponding to the 99.2 eV, which match the core level of $2p_{1/2}$ and $2p_{3/2}$ orbital, respectively. So we confirm the RhSi sample is on the light path. Fig. 2b shows the Fermi surface of RhSi sample. And the band structure of RhSi measured with 150 eV photon energy and 50 eV photon energy are show in the Fig. 2c-2e. The band structure and Fermi surface are looks not clearly. So more experiment should be do for further analysis.
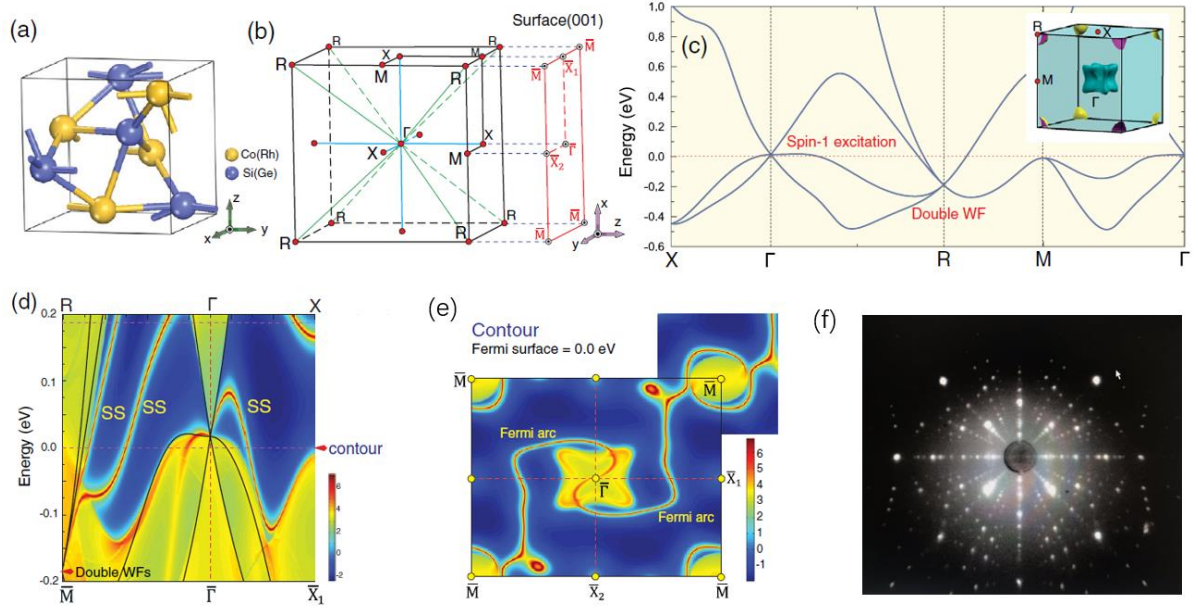
Figure 1. Crystal structure and electronic properties of Co(Rh)Si. (a) The crystal structure of Co(Rh)Si, the yellow solid ball stand for the Co(Rh) atom, while the blue solid ball stand for Si atom. (b) The Brillouin zone (BZ) for the Co(Rh)Si. The projected BZ of the (001) surface is marked in red lines. (c) The band structure of Co(Rh)Si along the high symmetry line. It exists double Weyl Fermions in R point in BZ. The inset shows the 3D Fermi surface of Co(Rh)Si at calculated Fermi level. (d) The corresponding electronic spectra for the (001) surface. Black solid curve stand for the bulk band. (e) The Fermi surface on the (001) surface of CoSi family.[1] (f) The Laue spot figure of RhSi.
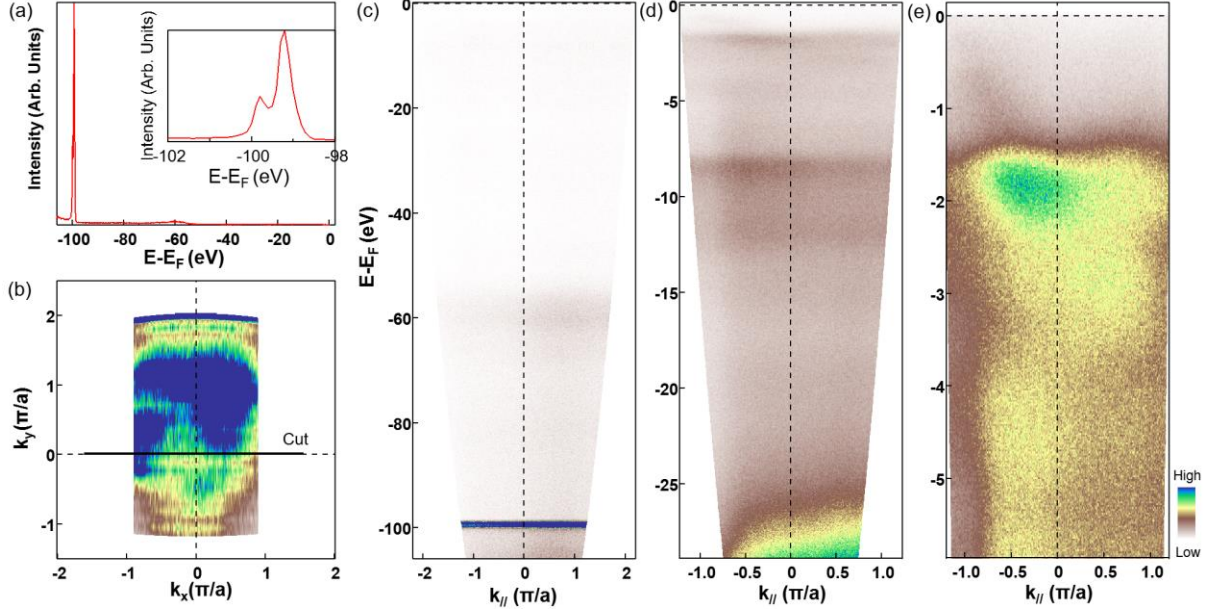

Figure 2. Electronic structure of RhSi. (a) The large energy range photoemission spectra measured with 150 eV photon energy. Zoom in the EDC as shown in the inset of (a). (b) The Fermi surface of RhSi. (c) The band structure of RhSi measured with 150 eV photon energy along momentum cut marked in (a). (d) and (e) The band structure of RhSi measured with 50 eV photon energy along the momentum cut marked in (a). (d) shows the larger range than (e).

REFERENCES

[1] Peizhe Tang, Shoucheng Zhang et al., Phys. Rev. Lett. 119(206402) 2017
[2] Guoqing Chang, M Zahid Hasan et al. Phys. Rev. Lett. 119(206402) 2017
[3] Tiantian Zhang, Zhong Fang et al., Phys. Rev. Lett. 120(016401) 2018

Electronic correlation effect in electron-hole systems with orbital degeneracy

T. Mizokawa[a], R. Matsumoto[a], T. Mitsuoka[a], T. Shimaiwa[a], N. L. Saini[b], R. Jha[c], R. Higashinaka[c], T. D Matsuda[c], Y. Aoki[c], and M. Arita[d]

[a] *Department of Applied Physics, Waseda University, Shinjuku-ku, Tokyo 169-8555, Japan*

[b] *Department of Physics, University of Roma "La Sapienza", Piazzale Aldo Moro 2, 00185 Roma, Italy*

[c] *Department of Physics, Tokyo Metropolitan University, Hachioji 192-0397, Japan*

[d] *HiSOR, Hiroshima University, Higashihiroshima, Hiroshima 739-0046, Japan*

In Weyl semimetals, a Dirac point is split into two Wely points in three-dimesional momemtum space due to time reversal symmetry or space inversion symmetry breaking [1-5]. In particular, the Weyl ponits and the surface Fermi arcs are identified in As-terminated TaAs by means of angle-resolved photoemission spectroscopy (ARPES) [6-10]. Among the various Weyl semimetals, $MoTe_2$ without space inversion symmetry is known as a type-II Weyl semimetal where the Weyl cones are turned over in the momentum space [11-14]. It is expected that Coulomb interaction between electron and hole plays important roles in such semimetals or narrow gap semiconductors. In the present work, we have studied the electronic structure of $MoTe_2$ by means of ARPES in order to clarify the effect of electron-hole correlation.

Figure 1 (a) shows the Fermi surface map of $MoTe_2$ taken at photon energy of 23.8 eV. A series of Femi pockets are observed along the k_x axis. As shown in Figure 1(b), the left and right Fermi pockets are reduced in size with increasing binding energy. Therefore, these Fermi pockets have electron character. On the other hand, the Fermi pocket around the zone center has hole character. The existence of electron and hole pockets is consistent with the band-structure calculation. However, the two electron pockets are observed at $k_x = \pm$ 0.3 - 0.4 $Å^{-1}$ whereas they are predicted at $k_x = \pm$ 0.4 - 0.5 $Å^{-1}$ in the calculation. In addition, the observed hole pocket is much smaller than the theoretical prediction. This situation is very similar to that reported for WTe_2[15] in which the excitonic correlation between electron and hole is responsible for upward and downward energy shifts of the electron and hole bands, respectively. Since the Weyl points are located above the Fermi level in WTe_2 and $MoTe_2$, optical control of the excitonic correlation can be employed to tune the Weyl point at the Fermi level.
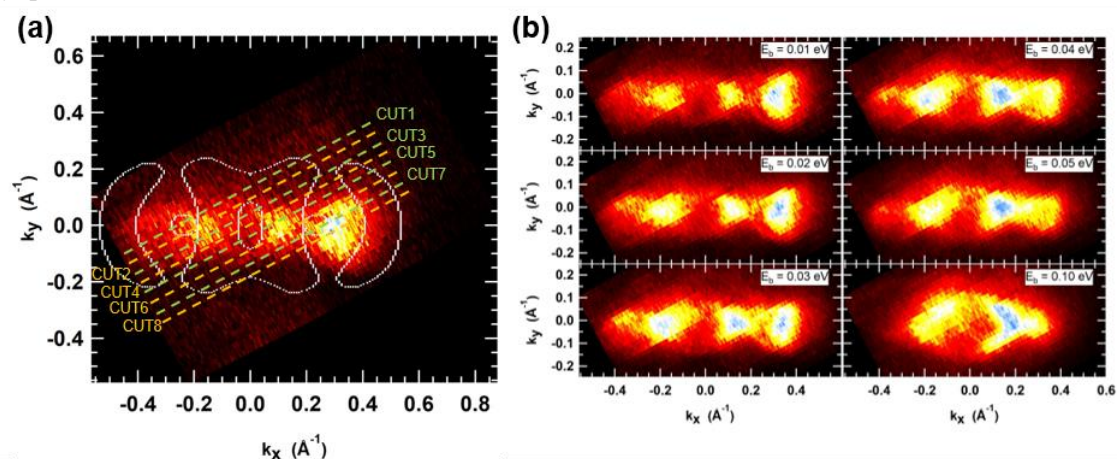

FIGURE 1. (a) The observed Fermi surfaces of $MoTe_2$ taken at 23.8 eV. (b) Constant energy maps at selected energies.
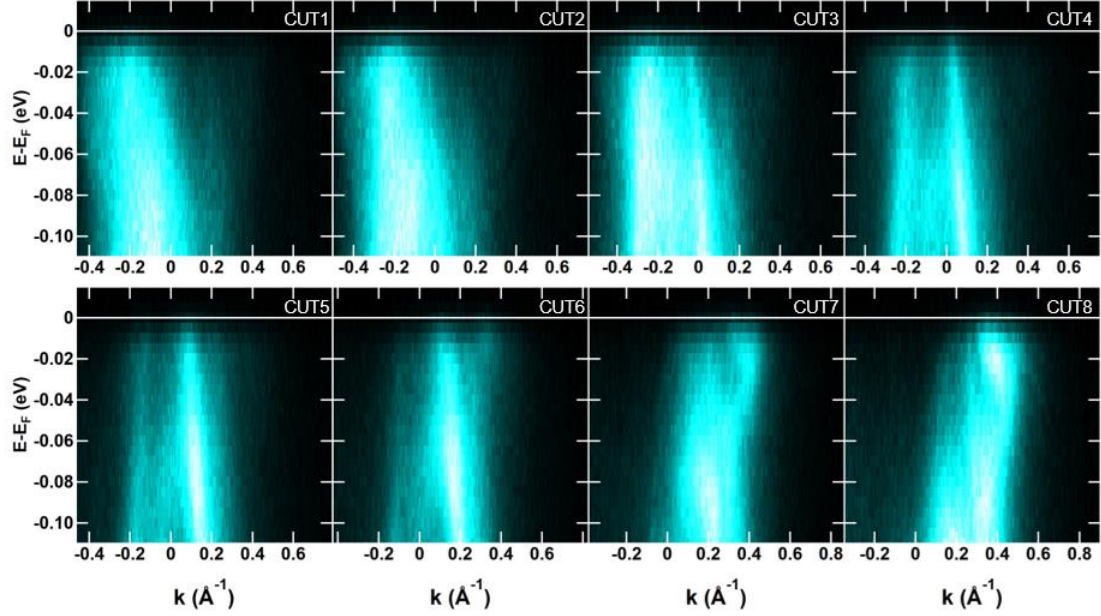
FIGURE 2. ARPES results near the Fermi level. ARPES intensity maps measured at photon energy of 23.8 eV along CUT1 to CUT8 direction indicated in Fig.1.

Figure 2 shows the band dispersions near the Fermi level for CUT1 to CUT8 as indicated in Fig. 1. The electron pocket on the right side is clearly observed in CUT6-CUT8. The bottom of the electron band reaches -0.04 eV below the Fermi level. A surface band stems from the electron band bottom and reaches the hole band around -0.06 eV. Ref. 14 has reported domain dependence of the surface band which is not clear in the present $MoTe_2$ crystal. The relationship between the electron-hole correlation and the surface band should be clarified in future by means of space-resolved ARPES and time-resolved ARPES.

REFERENCES

1. H. Weyl, *Z. Phys.* **56**, 330 (1929).
2. H. B. Nielsen and M. Ninomiya, *Phys. Lett.* **130B**, 389 (1983).
3. S. Murakami, *New J. Phys.* **9**, 356 (2007).
4. Xiangang Wan, Ari M. Turner, Ashvin Vishwanath, and Sergey Y. Savrasov, *Phys. Rev. B* **83**, 205101 (2011).
5. A. A. Burkov, M. D. Hook, and L. Balents, *Phys. Rev. B* **84**, 235126 (2011).
6. S.-M. Huang, S.-Y. Xu, I. Belopolski, C.-C. Lee, G. Chang, B. Wang, N. Alidoust, G. Bian, M. Neupane, C. Zhang, S. Jia, A. Bansil, H. Lin, and M. Z. Hasan, *Nat. Commun.***6**, 7373 (2015).
7. B. Q. Lv, H. M. Weng, B. B. Fu, X. P. Wang, H. Miao, J. Ma, P. Richard, X. C. Huang, L. X. Zhao, G. F. Chen, Z. Fang, X. Dai, T. Qian, H. Ding, *Phys. Rev. X* **5**, 031013 (2015).
8. S.-Y. Xu, I. Belopolski, N. Alidoust, M. Neupane, G. Bian, C. Zhang, R. Sankar, G. Chang, Z. Yuan, C.-C. Lee, S.-M. Huang, H. Zheng, J. Ma, D. S. Sanchez, B. Wang, A. Bansil, F. Chou, P. P. Shibayev, H. Lin, S. Jia, M. Z. Hasan, *Science* **349**, 614 (2015).
9. B. Q. Lv, H. M. Weng, B. B. Fu, X. P. Wang, H. Miao, J. Ma, P. Richard, X. C. Huang, L. X. Zhao, G. F. Chen, Z. Fang, X. Dai, T. Qian, and H. Ding, *Nat. Phys.* **11**, 724 (2015).
10. S.-Y. Xu, I. Belopolski, D. S. Sanchez, M. Neupane, G. Chang, K. Yaji, Z. Yuan, C. Zhang, K. Kuroda, G. Bian, C. Guo, H. Lu, T. R. Chang, N. Alidoust, H. Zheng, C. C. Lee, S. M. Huang, C. H. Hsu, H. T. Jeng, A. Bansil, T. Neupert, F. Komori, T. Kondo, S. Shin, H. Lin, S. Jia, M. Z. Hasan, *Phys. Rev. Lett.* **116**, 096801, (2016).
11. Yan Sun, Shu-Chun Wu, Mazhar N. Ali, Claudia Felser, and Binghai Yan, "Prediction of Weyl semimetal in orthorhombic MoTe2", Phys. Rev. B 92, 161107(R) (2015).
12. L. Huang, T. M. McCormick, M. Ochi, Z. Zhao, Michi-To Suzuki, R. Arita, Y. Wu, D. Mou, H. Cao, J. Yan, N. Trivedi, and A. Kaminski, *Nat. Mater.* **15**, 1155 (2016).
13. Ke Deng, GuoliangWan, Peng Deng, Kenan Zhang, Shijie Ding, EryinWang, Mingzhe Yan, Huaqing Huang, Hongyun Zhang, Zhilin Xu, Jonathan Denlinger, Alexei Fedorov, Haitao Yang, Wenhui Duan, Hong Yao, YangWu, Shoushan Fan, Haijun Zhang, Xi Chen, and Shuyun Zhou, *Nat. Phys.* **12**, 1105 (2016).
14. M. Sakano, M. S. Bahramy, H. Tsuji, I. Araya, K. Ikeura, H. Sakai, S. Ishiwata, K. Yaji, K. Kuroda, A. Harasawa, S. Shin, and K. Ishizaka1, *Phys. Rev. B* 95, 121101(R) (2017).
15. R. Matsumoto, T. Sugimoto, T. Mizokawa, N. L. Saini, M. Arita, R. Jha, R. Higashinaka, T. D. Matsuda, and Y. Aoki, *Phys. Rev. B* 98, 205138 (2018).

Electronic structure of electron-doped
J=1/2 Mott insulators

Yong Hu[a], Zhiyuan Wei[a] and Junfeng He[a]

[a]*University of Science and Technology of China, Hefei, Anhui 230026, China.*

Keywords: Iridates, Mott insulators, Electronic structure

Perovskite strontium iridates, the so-called spin-orbit coupled Mott insulators, have attracted much recent attention by the interplay of spin orbit coupling (SOC) and Coulomb interaction. The splitting of t_{2g} energy level by spin orbit coupling effectively reduces the width of each sub-band (J=3/2 and J=1/2), that a moderate onsite Coulomb Repulsion U is sufficient to split the J=1/2 band into upper and lower Hubbard bands.

Theoretically, many exotic phenomena, including superconductivity, have been expected when this spin-orbit coupled Mott insulator gets doped [1]. Experimentally, one important finding in electron-doped iridates is the spectroscopic evidence for negative electronic compressibility [2]. Negative properties of materials, although rarely existed, have attracted substantial general interests by their roles in changing the ways people think about materials. As a prominent example, negative electronic compressibility (κ_e) does appear in some quantum materials when it is countered by the positive compressibility of other subsystems of the materials. However, it was only found in very few dilute 2D systems in which the electron exchange energy dominates over kinetic energy. Recently, we found most likely the first experimental evidence for 3D negative κ_e in $(Sr_{1-x}La_x)_3Ir_2O_7$, which is driven by a dominance of the correlation energy of electrons at a relatively high density [2]. Our finding might open the door to an uncharted territory of negative κ_e which potentially features a variety of bulk correlated metals. It is natural to ask whether the negative electronic compressibility also exists in the single layer electron-doped iridates, $(Sr_{1-x}La_x)_2IrO_4$. To this end, we proposed systematic ARPES study on the electronic structure of electron-doped J=1/2 Mott insulators $(Sr_{1-x}La_x)_2IrO_4$.
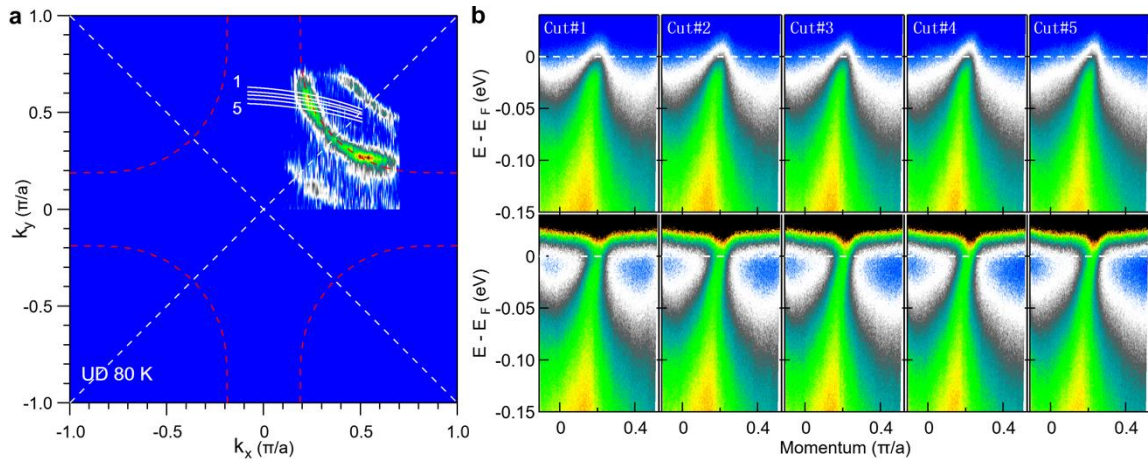

FIGURE 1. Fermi surface and band structure of the UD80 K Bi2212 sample. (a) Fermi surface of the UD80 K Bi2212. (b) Band structure along five momentum cuts around anti-nodal direction (cut 1 to 5 as labelled in a). Upper panel shows the raw data, the spectra in the lower panel have been divided by the corresponding Fermi-Dirac distribution functions. The data were taken at ~95 K.

ARPES measurements were carried out at HiSOR BL-9A on the La-doped Sr_2IrO_4 samples. However, we didn't get clear band dispersion on Sr_2IrO_4 samples with the Xe lamp (no synchrotron available), possibly due to the matrix element effects in ARPES measurements. But these initial tests provided us some very useful information for the follow-up beam time in other places. For this beam time, we carried out the back-

up plan and measured Bi-2212 samples (UD80K). The Fermi surface mapping and band dispersion are shown in Fig. 1. More systematic data analysis will be performed in the near future.

REFERENCES

1. F. Wang et al., Phys. Rev. Lett. 106, 136402 (2011).
2. J.-F. He et al., Nat. Mat. 14, 577-582 (2015).

Photoemission study of mechanical polished FeSi [111] surface

M. Arita[1], K. Shimada[1], T. Kanomata[2]

[1]*Hiroshima Synchrotron Radiation Center,Hiroshima University, Kagamiyama, Higashi-Hiroshima 739-0046, Japan*

[2]*Research Institute for Engineering and Technology, Tohoku Gakuin University*

FeSi is a nonmagnetic semiconductor at low temperatures. With increasing temperature, the magnetic susceptibility rises and the temperature dependence of the electric resistivity shows a crossover from the semiconducting state to the metallic state at ~300 K [1,2]. Thus FeSi can be viewed as the Kondo insulator [3]. In order to investigate the electronic structure and electron-electron correlation effect in FeSi, the ARPES measurements on FeSi [111] surface were carried out at BL-9A. In previous our study, the ordered surface was obtained by cleavage, but it is difficult to obtain the surfaces on which ARPES spectra could be observed [4]. In this paper, FeSi [111] clean surface could be obtained by mechanical polishing and annealing. The sharp LEED image can be seen from the surface (Fig. 1). We examine a difference of the observed spectra due to a difference of the surface treatment procedure.

Figures 2 shows the ARPES image for $h\nu = 8.4$ eV at 10 K. The clear hole-like band, a maximum of which exists about E = - 25 meV, is observed around $k_x = 0$. As the spectral intensity is enhanced near E_F steeply, which suggests the strong renormalized band exists near E_F due to the electron-electron interaction.

To clarify the temperature dependence of the renormalized band structure, we measured the temperature dependence of the normal emission spectra with $h\nu = 8.4$ eV. Figures 3 shows the spectra between 10 and 350K, which corresponds to the energy distribution curve (EDC) at $k_x = 0$. The strong peak structure is found at 10K. The peak width broadens and the energy is shifted toward E_F with increasing temperature. Though the spectral intensities at E_F are suppressed below 100 K strongly, the full gap structure is not observed. It is considered that the measured sample is the p-type semiconductor or that the metallic surface state exists. The spectral intensity at E_F increases above 100 K and the peak and gap structures almost disappear at 350 K. These spectral structures and temperature dependence are consistent with the

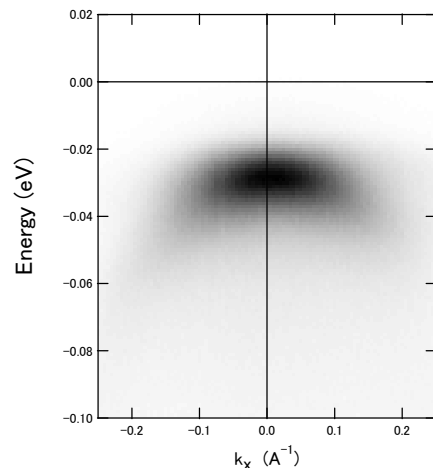Fig.1 LEED image of FeSi [111] for E = 110 eV.

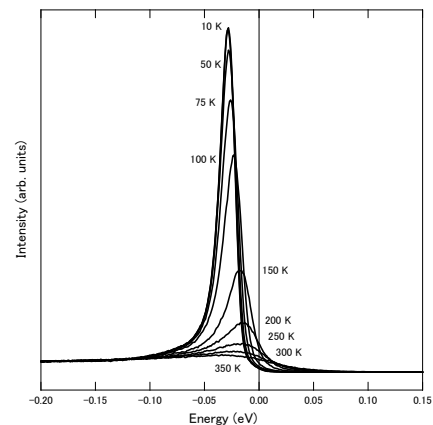Fig.2 ARPES image of FeSi [111] with $h\nu = 8.4$ eV.

Fig.3 Temperature dependence of EDCs at $k_x = 0$ taken with $h\nu = 8.4$ eV.

temperature dependences of the electrical resistivity and the magnetic susceptibility [5,6,7] and correspond to the result of the previous study [4].

Compared with the spectral features measured for the cleaved surface, the band dispersion is observed more clearly and the EDC peak intensity relative to the intensity around E = -0.15 eV is higher for the polished surface. Thismeans the atomic order for the polished surface in a wide area is better than that of cleaved surface. Therefore, it is expected that the ARPES spectra having little deviation can be obtained for FeSi [111], because the clean surface with good reproducibility can be prepared by the mechanical polishing.

[1] V. Jaccarino *et al*., Phys Rev. 160, 476 (1998).
[2] M.B.Hunt *et al*., Phys Rev. B 50,14933 (1994).
[3] G. Aeppli,*et al*., Comments Condens. Matter Phys. 16,155 (1992).
[4] M. Arita *et al*., Phys Rev. B 77,205117 (2008).
[5] K. Koyama *et al.*, J. Phys. Soc. Jpn. 68, 1693 (1999).
[6] K. Koyama *et al*., J. Phys. Soc. Jpn. 69, 219 (2000).
[7] E. Arushanov *et al*., Phys. Rev. B 55, 8056(1997).

Electronic structure of van der Waals ferromagnet Fe₃GeTe₂

X. Xu[1], Y. J. Chen[1], L. X. Yang[1], Y. L. Chen[1]

[1] *Physical department, Tsinghua University, Beijing 100084, China*

Keywords: van der Waals ferromagnet, Electronic structure, ARPES

Van der Waals compounds represent a large variety of layered materials with extremely weak interlayer coupling. On one hand, they provide fertile platform to explore and realize various intriguing emergent phenomena, such as charge/spin density wave, superconductivity, magnetism, and topological quantum phases. On the other hand, they can deliver exotic two-dimensional materials and hetero-structures with extraordinary properties, such as quantum Hall effect and Dirac fermions in graphene, valley transport in atomically thin transition metal dichalcogenides, quantum spin Hall effect in monolayer topological quantum materials, and high temperature superconductivity in FeSe-SrTiO3 interface. These extraordinary properties both in thin films and bulk form of the Van der Waals compounds not only provides significant scientific implications in condensed matter physics, but also promise broad application potentials in the electronics and spintronics devices.

Recently, low-dimensional ferromagnets have attracted great research attention. Many different types of van der Waals ferromagnetic materials, such as $Cr_2Si_2Te_6$/$Cr_2Ge_2Te_6$, CrI_3/$CrBr_3$, and Fe_3GeTe_2 (FGT) [1-7], have been thinned to their physical limit to realize 2D ferromagnets. Among them, Fe_3GeTe_2 has been intensively studied due to the realization of tuneable room temperature ferromagnetism in its monolayer form. The survival of 2D ferromagnetism against the thermal fluctuation in FGT is protected by the intrinsic magnetocrystalline anisotropy [6, 7]. Thickness dependent measurements have revealed 2D to 3D crossover of the ferromagnetism [6]. Besides the 2D ferromagnet in atomically thin FGT, bulk FGT also exhibits fertile and intriguing properties, such as electron correlation [6], Kondo lattice physics [8], strongly enhanced electron mass, and extremely large anomalous Hall effect induced by topological nodal lines [9], coherent-incoherent crossover. However, despite the intensive research effort, the detailed electronic structure of bulk FGT, especially its evolution, is still essentially lacking.
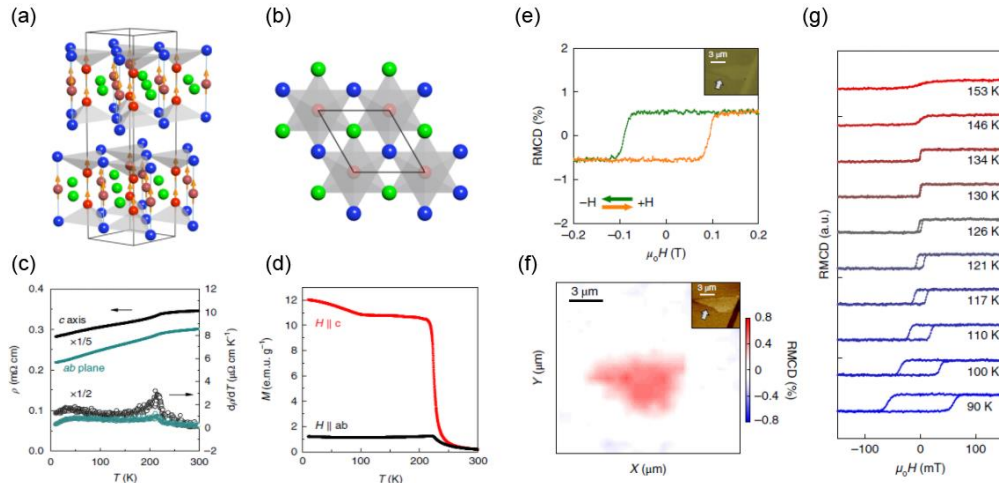

Figure 1 (a) Perspective view and (b) top view of crystal structure of Fe₃GeTe₂. (c) Resistivity and its derivative with respect to the temperature as functions of temperature. (d) Magnetic moments as functions of the temperature along c and ab directions. (e) RMCD measurement of the ferromagnetism in monolayer Fe₃GeTe₂. (f) RMCD map at magnetic field of 0.2 T at 78 K. (g) RMCD sweeps at different temperatures in the monolayer Fe₃GeTe₂. Panels (c) and (d) are from Ref. [9]. Panels (e-g) are from Ref. [6].

FGT crystallizes into a layered hexagonal structure with space group of P63/mmc (No. 194). It consists of stacking FeTe-FeGe-FeTe sandwich layers that are bonded by weak van der Waals interaction as shown in Figs. 1(a) and 1(b). There are two different positions for the Fe atoms. Fe1 and Te form pyramid, while Fe2 and two Te atoms form Te-Fe-Te vertical lines. There are two FeTe-FeGe-FeTe

sandwich layers rotated 90 degrees about c axis in the unit cell of FGT. In the ferromagnetic state, the magnetic moment of all the Fe atoms aligns along the c axis, indicated by the orange arrows in Fig. 1(a). Figure 1(c) shows the 3D Brillouin zone and its (001) surface projection. The crystal can be easily cleaved along (001) direction, inducing clean and flat surface with large scale. Transport measurements suggest a ferromagnetic transition near 220 K with large anisotropy (Figs.1(c) and (d)). Ab-initio calculations of the electronic structure of FGT in the ferromagnetic and paramagnetic states (Fig. 1(h)) show the complicated band splitting due to the exchange interaction [9]. By thinned to its monolayer limit, FGT still shows strong ferromagnetism at low temperatures with a thickness dependent ferromagnetic transition, as shown in Figs. 1(e)-(g) [9].
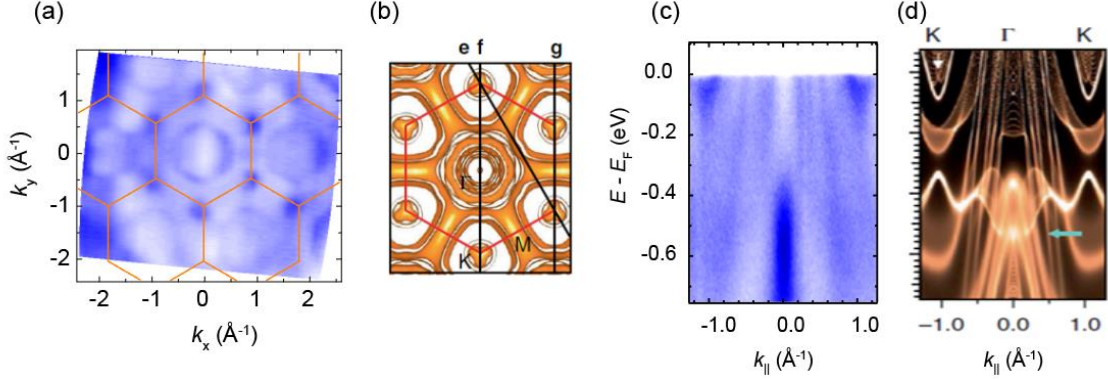

Figure 2 ARPES measurements on Fe_3GeTe_2. (a) Fermi surface mapping. (b) DFT calculation of fermi surface from Ref. [9]. (c) Band dispersion along ΓK. (d) DFT calculation from Ref. [9].

In this report, we study the electronic structure of FGT using high-resolution ARPES at beamline 9A in Hisor. The measured fermi surface consists of a hole pocket around the center of the Brillouin zone and blurred spectral weight from the electron dispersion near the K points, which shows overall consistence with previous reports (Figs. 2(a) and 2(b)) [9]. The cut in Fig. 2(c) shows the electron dispersions along KGK. The bands show strong polarization dependence due to their 3d orbital nature. Therefore, not all the bands in the calculation (Fig. 2(d)) are observed in our measurement using photons with linearly horizontal polarization. We have measured the temperature evolution of the electronic structure of FGT (not shown here), further studies and analysis of our data will provide important insights to the intriguing physical properties of FGT.

REFERENCES

[1]C. Gong et al., Nature. 546, 265–269 (2017).
[2] B. Huang et al., Nature. 546, 270–273 (2017).
[3]Y. Liu, C. Petrovic, Phys. Rev. B 96, 054406 (2017).
[4] G. Lin et al., Phy. Rev. B. 95, 245212 (2017).
[5] B. Liu et al., Sci. Rep. 6, 33873 (2016).
[6] Z. Y. Fei et al., Nat. Mat. 17, 778 (2018).
[7] Y. J. Deng et al., arXiv:1803.02038 (2018).
[8] Y. Zhang et al., Sci. Adv. 4:eaao6791 (2018).
[9] K. Kim et al., Nat. Mat. 17, 794 (2018).